AN ABSTRACT OF THE THESIS OF

J. Cameron McNatt for the degree of Master of Ocean Engineering in Civil Engineering presented on August 1, 2012
Title: Wave Field Patterns Generated by Wave Energy Converters

Abstract approved:

H. Tuba Özkan-Haller

The eventual deployment of wave energy converters (WECs) on a commercial scale will necessitate the grouping of devices into arrays or "wave farms," in order to minimize overhead costs of mooring, maintenance, installation, and electrical cabling for shoreward power delivery. Closely spaced WECs will interact hydrodynamically through diffracted and radiated waves. Recent research has focused on the WEC wave field and used its structures to design constructive WEC arrays as well as to describe the means of WEC energy absorption. In this study, the WEC wave field is investigated for a single WEC and a five WEC array with linear wave theory and experimental results. Both regular waves and spectral seas are considered. Computational results are produced with the linear boundary-element-method (BEM) hydrodynamic software WAMIT for a simple WEC geometry. Experimental data comes from WEC array tests that took place at Oregon State University over the winter of 2010-11 [1]. The experimental measurements help validate the computational modeling, and the computational models serve as an aid to interpreting the experimental data.

Results reveal two universal WEC wave field features - partially standing waves and a wave shadow, both of which are the result of the coherent interaction of the planar incident wave with the circular generated wave, composed of the diffracted and radiated waves. The partial standing waves in the offshore are seen qualitatively in experimental data but could not be exactly reproduced computationally, because the computational model is only a simple representation of the physical model. In the lee of the WEC, the measured longshore structure of the wave shadow is in good agreement with theoretical expectations as well as computational results. It is believed that the agreement is

because the formation of the wave shadow is dominated by energy extraction, which was approximately the same for both the computational and physical models.

A study of the linear WEC wave field in regular waves and spectral seas reveals patterns such as the wave shadow that have also been found in experimental data. The positions and magnitudes of the offshore partially standing waves are very sensitive to wavelength, and WEC geometry, motions and location, and in spectral seas, they are smoothed when considering significant wave height. All of which suggest that it may be difficult to use them advantageously in the design of WEC arrays. The wave shadow is a dominant feature of the WEC wave field for both regular waves and spectral seas. It appears to be fairly generic and to be based on power absorption. In the design of WEC arrays, rather than attempting constructive interference by using standing wave crests, perhaps the best one can do is to avoid destructive interference of the wave shadow.

Wave Field Patterns Generated by Wave Energy Converters

by

J. Cameron McNatt

A THESIS

submitted to

Oregon State University

in partial fulfillment of

the requirements for the

degree of

Master of Ocean Engineering

Presented August 1, 2012

Commencement June 2013

Master of Ocean Engineering thesis of J. Cameron McNatt presented on August 1, 2012

APPROVED:

Major Professor, representing Civil Engineering

Head of the School of Civil and Construction Engineering

Dean of the Graduate School

I understand that my thesis will become part of the permanent collection of Oregon State University libraries. My signature below authorizes release of my thesis to any reader upon request.

J. Cameron McNatt, Author

ACKNOWLEDGMENTS

This research was partially funded by the U.S. Department of Energy (DE-EE0002658), Sandia National Labs, and Columbia Power Technologies under Research Subagreement NO. 2010-1698, additional support came from Oregon Wave Energy Trust through Award Number OIC-0911-109. A portion of the thesis is based upon work enabled by the National Northwest Marine Renewable Energy Center and the U.S. Department of Energy under Award Number DE-FG36-08GO18179.

Throughout the course of this project I had a great amount of assistance and support. The experimental data analysis and organization was performed by Aaron Porter. This, I know, was no small task. All I had to do was put the numbers in a plot. Aaron also conducted all of the SWAN runs. Using one computational model is hard enough, I am glad I did not have to learn two. Aaron, I could not have done it without you.

Mick Haller, Pukha Lenee-Bluhm, and Aaron suffered through numerous overtime meetings, discussing our results and planning our next moves. It was always rewarding to share the ideas and work in which I had been engrossed in the weeks previous and extremely helpful to get outside feedback. The discussions we had were impassioned and thought-provoking. The meetings served as regular check points in our progress towards a final product. Thank you all for your considerate attention, observations, and guidance.

I would like to thank Tuba Özkan-Haller, my advisor. Not only during this project, but throughout my graduate studies at Oregon State, she has been so supportive, encouraging, and interested in my endeavors. She gave me the freedom and provided the projects and tools that enabled me to follow courses of investigation about which I was passionate. Her advice and input especially on my writing was always thoughtful and insightful. Tuba, you have been a superb advisor. Thank you so much, and I wish you all the best.

And to my beautiful wife, Tess, thank you for taking on this adventure with me. It is no small deal to move across the country to a new place with new people, leave your friends and family behind, quit your well paying jobs, and live the life of students. Your love, support, and simply your company made it a pleasure. You encouraged me to follow my dreams, and were there at my side as I did. Home is wherever I'm with you. Bootie, I love you so much!

TABLE OF CONTENTS

LIST OF FIGURES

Wave Field Patterns Generated by Wave Energy Converters

1 Introduction

Anyone who has been in a boat in a crowded river or lake has felt the effects of hydrodynamic interactions between floating bodies. Waves from one boat propagate through the water, become incident upon and create motion in other vessels. Typically, the waves are the Kelvin wake generated by the boat's steady forward motion. Wave energy converters (WECs) generally do not move at a steady speed. Instead, they oscillate about a mean position and so the hydrodynamic interactions between multiple closely spaced WECs are via two other types of waves, diffracted waves and radiated waves. When boat wakes intersect the resulting wave is the combination of each wake, which in some cases is larger and others smaller than each wake independently. Similarly, the coherent interaction of the incident, diffracted and radiated waves creates spatial variations in the wave height around a single WEC or arrays of WECs. An example of a WEC wave field is shown in Fig. 1.

A fundamental facet of WECs is that they remove energy from the waves, and so by conservation of energy, they necessarily must decrease the net wave height, which is related to wave energy. In fact, they not only remove energy but also redistribute it. In the wave field shoreward of a group of WECs, wave energy removal may affect coastal processes such as erosion and accretion, human commercial and recreational activities, environmental and biological processes, and even the efficacy of other arrays of wave energy converters. In the near WEC wave field, this has significant implications to the design of WEC arrays.

The eventual deployment of WECs on a commercial scale will necessitate the grouping of devices into arrays or "wave farms," in order to minimize overhead costs of installation, mooring, maintenance, and electrical cabling for shoreward power delivery. Closely spaced devices are not isolated from one another, but interact hydrodynamically. Despite WEC energy removal, hydrodynamic WEC array interactions have been shown in theory under certain circumstances to be constructive; that is, by interacting the power performance of the array is greater than the sum of isolated individual performances. However, the assumptions made in these computations may not be realistic. In

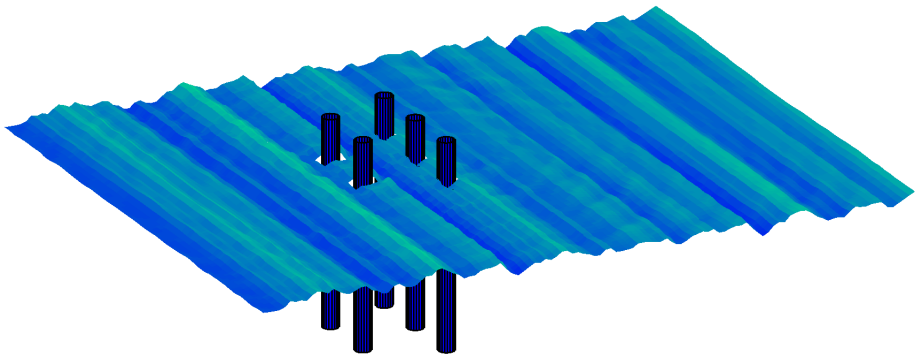

Figure 1: The picture shows the wave elevation of an array of five cylindrical WECs as computed by WAMIT. The image is stretched in the z-direction in order to magnify the size of the waves.

any case, the design of WEC arrays or array optimization is complex, but will have a significant impact on the power performance and economics of a wave farm.

In the past, array optimization has focused on performance as the only parameter to guide the spatial configuration of WEC arrays. Hydrodynamic interactions were implicit in the formulations of performance through the radiation and excitation forces, but the interaction of various waves was not explicitly examined. Only recently have researchers looked specifically at the WEC wave field, and used it to guide spatial WEC array design. For example, Child and Venugopal [2] exploited standing waves in their Parabolic Intersection method to design constructive arrays. Herein, the so-called "wave shadow" in the lee of a WEC is described.

Physically, WECs absorb wave energy when wave momentum is transferred to the mechanical motions of the device, which is converted down the line to other forms of energy. However, the process is not simple - some wave energy is reflected off the device; at times the device transfers energy back to the wave field through a momentum exchange; and within the wave field, wave energy diffuses spatially. Fortunately, linear water wave theory serves to simplify the wave-body interaction processes and computations.

Under the assumptions of potential flow, small wave height, and small body motions, linear wave theory breaks down the wave field into the superposition

of three components - the incident wave, the diffracted wave, and the radiated waves. The incident wave is the wave that exists in the absence of submerged bodies. The diffracted wave is the wave that is generated when the incident wave interacts with fixed (not moving) submerged or partially submerged bodies. One could think of the diffracted wave as similar to a reflected wave, but it includes a wave field that propagates at all directions. Radiated waves exist for each mode of motion of the device. For a given mode, the radiated wave is generated by the device motion in the absence of incident waves.

In linear wave theory, energy is removed from and redistributed within the wave field by the precise relationship in amplitude and phase of the incident wave to the combined diffracted and radiated waves. Farley [3] calls the combined diffracted and radiated waves the generated wave. Offshore, the redistribution occurs as partially standing waves. In the lee of a WEC, the energy redistribution and removal combine to create a wave shadow. These wave field patterns exist for a regular wave at a given incident wave frequency and direction. In reality, WEC arrays will operate in spectral seas, in which wave energy is spread over wave frequency and direction. Spectral seas can be approximated as multiple incident wave components at different frequency-direction pairs, and which, under linear wave theory are independent of one another. Wave fields can be computed separately for each wave component and then the results combined to produce a spectral wave field. Consideration of the spectral wave field is critical to the optimization of WEC arrays for real conditions.

In this thesis, WEC wave fields are studied explicitly with linear wave theory and through experimental data analysis in order to show fundamental patterns that could be helpful in the design of WEC arrays. Results are shown as plots of wave elevation and wave energy flux for regular waves and as plots of significant wave height and wave spectra for irregular waves. Computational results are produced by the linear boundary-element-method (BEM) hydrodynamic software WAMIT for a simple WEC geometry. Experimental data comes from WEC array tests of a device designed by Columbia Power Technologies, Inc. The experiments took place in the O.H. Hinsdale Tsunami wave basin at Oregon State University over the winter of 2010-11 [1]. The experimental results help to validate the computational model results, and the computational models serves as an invaluable aid to interpreting the experimental data.

Phase-resolving linear wave theory is one of many computational methods available with which to model the WEC wave field. And so in addition, a comparison is made of the phase-resolved wave field to that of a phase-averaged computational model, SWAN. Phase-averaged models are not able to model some of the physical wave-structure interaction processes explicitly, but can be augmented with physics-based parametric approximations. In general, they are computationally faster and can cover a broad domain with a realistic bathymetry. The goal of the comparison was the explore the adequacy of the phase-averaged model in reproducing the linear WEC wave field.

The importance of hydrodynamic interactions in the design of wave farms should not be underestimated. They will have a significant impact on the overall performance and hence the economics of the wave energy. There are numerous methods for computing WEC array interactions. Some require significant computation time and do not elucidate the means of the interactions, that is the WEC generated wave field. Recent research has studied the wave field explicitly and found it to be useful for understanding WEC energy absorption and array interactions, and for designing WEC arrays. Results discussed in this paper expand upon previous WEC wave field research and show some WEC wave field patterns experimentally. It is believed that the patterns are fundamental and apply generally to WECs of any type. WEC engineers could to apply the understanding of WEC wave field patterns as rules-of-thumb in their preliminary array designs.

2 Background

A great variety of computational methods exist for modeling wave energy converter arrays, and an excellent review and comparison is given by Folley et al. [4]. Herein, the focus is linear wave theory, which because of its relative simplicity has historically been the dominant theoretical framework for studying WEC arrays. In this section, a brief review of array computations, optimization, and wave field studies based on linear wave theory is given.

2.1 Computation of WEC Array Performance

The linear wave theory methods used in the computation of WEC array performance have developed from analytical to numerical with advances in computing power. Although numerical methods are fairly common now, some of the original analytical methods are still useful for promoting conceptual understanding, and they perform well within the range of their assumptions.

The commonly used measure of WEC array performance is the factor q.

$$q = \frac{Power\ of\ Array}{N \times (Power\ of\ a\ Device)}$$

where N is the number of devices in the array. A q greater than 1 signifies constructive interference and is desirable. A q less than 1 indicates destructive device interaction, and a q equal to 1 means that there is no net gain from the array. Although it is not the only means of measuring WEC array hydrodynamic interaction, it is the most commonly used, has a simple and universal scale, and shall be referenced throughout this document.

The very first studies [5, 6, 7] on WEC array performance used two important assumptions: 1) the point absorber assumption and 2) optimal motions. The point absorber assumption states that the dimensions of an individual WEC are much smaller than the incident wavelength, and so the diffracted wave can be neglected. The interaction of the radiated wave with the incident wave is the only means of hydrodynamic interactions between the devices. One may wonder why, if the body is small enough to neglect the diffracted wave, should the radiated wave be significant. This is generally attributed to the assumption of optimal motions [8]. It was found by Evans [6] that if the radiation and excitation forces are known for every mode of motion of every body (all degrees of freedom), there exists an amplitude and phase of

motion for each degree of freedom that maximizes the total power absorption of the incident wave by the array.[1] Depending on incident wave frequency and the properties of the radiation interaction, the amplitudes of these motions could be very large, and in some cases unrealistically large. Because the body motions are large, the amplitude of the radiated wave is proportionally large (assumed to be much larger than the diffracted wave).

Later work improved upon these assumptions. Thomas and Evans [7] showed that for a row of five semi-submerged spheres the amplitude of optimal motions could be eight times higher than the incident wave height, which is physically unlikely. In addition to computing the performance of the array oscillating with optimal amplitude, they found the performance for motions where the amplitude was limited to two and three times the incident wave amplitude. Simon [9], developed the plane wave method to approximate the diffracted wave as well as scattering by the radiated waves in WEC arrays. The method states that if the devices are spaced far enough apart, a diffracted or radiated wave from device 1 incident on device 2 could be modeled as a plane sinusoidal wave at device 2 of an amplitude defined by the scattering properties of and distance from device 1. Kagemoto and Yue [10] devised a fully analytical method for solving hydrodynamic interactions within arrays of floating bodies that included forces due to propagating and evanescent wave modes. If the forces and wave response for each individual body is known, then the hydrodynamic problem can be formulated into a matrix and solved efficiently. Their method is exact within the context of linear wave theory.

Except for relative simple canonical cases, numerical methods are required for finding the diffracted and radiated wave fields and forces on submerged geometries. One of the more common methods is the boundary-element method (BEM), which is the method employed by WAMIT to solve linear hydrodynamic problems in the frequency domain [11]. In its most fundamental sense, the BEM is known as the integral method because a solution to the flow (Laplace's equation), is found by integrating source or dipole distributions over the surfaces in the boundary value problem. In the traditional low-order version of the BEM, wetted surfaces are discritized into quadrilateral panels containing a source or dipole. The source or dipole strength is determined so that the boundary conditions on all the panels are met [12]. The implementation of the BEM in WAMIT is described in the WAMIT User's Manual [11].

[1] Section 3.3 explains the optimal motions mathematically.

Several authors have used WAMIT [13, 14, 15, 16, 17] or another BEM code [18, 19, 20] to solve for the hydrodynamic forces in WEC arrays.

Early methods in computing WEC array hydrodynamics made significant assumptions about the motion and size of the WECs. Later methods improved upon these assumptions so that the WEC array problem can now be solved completely for any number of bodies with arbitrary geometries under the assumptions of linear wave theory.

2.2 WEC Array Optimization

The primary goal of array design is to maximize the output power of the array for its intended wave conditions within the limits of cost, safety, and practicality. Such an effort is called array optimization. In general, array optimization includes the design of the spatial layout of the devices as well as individualized control and power take-off (PTO) settings. Several studies have shown that individualizing the PTO settings can have significant benefits to the array performance [18, 14, 15]. Optimization of the array would necessitate the simultaneous optimizations of both the layout and the PTO properties, which is a complex problem. In the present study on the hydrodynamic interactions, WEC array optimization is only with respect to the spatial configuration of the WECs in the wave field.

Many early studies of WEC array hydrodynamic interactions only considered a single row or a regular grid of evenly spaced devices and examined the performance as a function of the separation distance between devices [5, 6, 7, 21, 9]. They showed very high q values at certain ratios of device spacing to wavelength and q values much less than 1 at others. For a given wave frequency and direction, the spacing between the devices could be tuned to optimize the array performance. However, at that same array spacing, significant losses would occur at other wave frequencies and directions. Because real seas are spectral and vary temporally, it is clearly not possible to achieve consistent constructive hydrodynamic interference.

Recognizing this characteristic, McIver [8] stated:

> ...part of a practical strategy for the design of wave-power stations with large numbers of devices might be to seek to reduce destructive interference effects, perhaps by using unequal spacing, rather than attempt large increase in power absorption through constructive interference.

He computed the performance for a row of devices with unequal spacing and found that q was consistently much closer to 1 for all frequencies and directions examined. Mavrakos and Kalofonos [22] computed the performance of two irregular WEC array arrangements and compared them to a regular row of devices. For the irregular array configurations, they also found q to be more consistently near 1 over all frequencies. Neither of these studies attempted to optimize the array configuration for a given set of wave conditions.

More recent research has examined arrays in relatively simple configurations: a pair of devices [18, 19], a triangle [17], an "X" shape [23], and a square [14], in both regular and irregular waves. Borgarino et al. [20] examined triangular and regular grids of 9, 16, and 25 WECs in spectral seas and found that the triangular grid performed better than the regular grid. In several studies, the effect of device spacing on the array performance was examined, but in none was an optimization performed to find the arrangement of maximum power production.

Fitzgerald and Thomas [24] performed a constrained nonlinear optimization of the configuration of an array of five spherical WECs at a single frequency under the point absorber and optimal motions assumptions. Their optimal arrangement had a q value of 2.77, which is extremely high for such a small number of devices. In the same paper, they presented a consistency condition, which states that under the point absorber assumption at a given frequency, the average of q over all wave directions is 1. This means that for any region of constructive interference at one direction, there must be an equal amount of destructive interference at other directions. The plots of the q factor versus direction for the optimal arrangement show a large spike of 2.77 at the direction for which the array was designed, and values near or less than 1 at all other directions. Fitzgerald and Thomas's optimization was the first of its kind but it was performed within the possibly unrealistic context of optimal motions and point absorber theory.

Folley and Whittaker [16] found optimal configurations of two, three, and four point absorbers with optimal motions for spectral seas. To find the optimal configuration, they mapped values of the average q factor (traditional q factor scaled by the incident wave energy) to values of the parameter space. In spectral seas, the average q factor of the optimal array was always close to 1. The use of spectral seas was a step forward in array design, but the optimization was still performed with point absorber and optimal motions

assumptions.

Child and Venugopal [2] used the exact analytical method of Kagemoto and Yue to solve for an array of five cylindrical WECs. To find optimal configurations, they used a genetic algorithm and a novel heuristic method, which they termed the Parabolic Intersection (PI) method. They found parabolic-like contours around a single device where the incident wave was in-phase and out-of-phase with the combined radiated and diffracted wave. The parabolic intersection method takes advantage of the parabolas formed by either the incident and diffracted wave or the incident and radiated wave to guide the placement of devices in an array. Devices placed on in-phase parabolic curves lead to higher array performance, because these intersections indicate the location of crests of partial standing waves. Although their genetic algorithm method did not explicitly guide the WEC positions towards in-phase crests, the optimal configurations found by the genetic algorithm had devices located on such crests. The optimization was performed for a single frequency and direction, but they examined the performance of the optimal arrays as a function of frequency and direction. Child and Venugopal's research was the first time that the wave field had been explicitly utilized in the design and analysis of a WEC array.

2.3 WEC Wave Field

Under linear wave theory, harmonic wave components can be superimposed to create a total wave field. If progressive wave components are of different frequencies, they travel at different speeds and pass through one another. However, if the waves are of the same frequency (coherent), their interaction is different and can lead to wave magnification, cancellation, and partially or fully standing waves depending on the relationship between the amplitude, phase and direction of the waves.

This can be most easily understood with a two-dimensional example. Consider two waves of the same frequency and traveling in the same direction with amplitudes a_1 and a_2, respectively. When the waves are in phase, the result is a harmonic wave traveling in the same direction with an amplitude $a_1 + a_2$. When the waves are out of phase, they result in a wave of amplitude less than $a_1 + a_2$ reaching a minimum of 0 when the waves are 180° out of phase. Now, consider the wave components traveling in opposite directions.

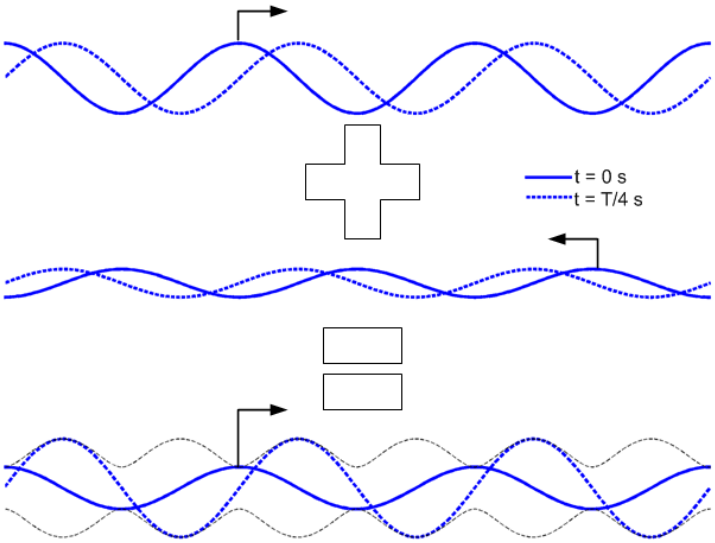

Figure 2: The figure shows the superposition of two 2D waves travelling in opposite directions. The resultant wave is a partially standing wave shown at the bottom. The solid line shows the waves at time, $t = 0\,s$, and the dashed line shows the waves at a future time, $t = T/4\,s$, where T is the wave period. The black dashed line shows the envelope of the standing wave. Note how the resultant wave increases in amplitude from $t = 0\,s$ (at a node) to $t = T/4\,s$ (at an anti-node).

When the amplitudes of the two waves are the same, the result is a fully standing (non-progressing) wave. When the amplitudes are not equal, the result is a partially standing wave progressing in the direction of the wave with the higher amplitude (see Fig. 2). The amplitude of a two-dimensional standing wave forms a simple harmonic pattern of nodes and anti-nodes. The node is the location of minimum wave height; for a fully standing wave the node has zero wave height. The anti-node is the location of maximum wave height. The positions of the nodes and anti-nodes are determined by the phasing relationship between the wave components. One can now imagine placing WECs in the two-dimensional standing wave field. It seems that a WEC placed at an anti-node would perform better than a WEC at a node.

A similar behavior occurs in three-dimensional wave fields except the patterns are more complex because there are many wave directions and because the waves do not have to be planar, but can also be circular. Modern studies have investigated the wave field to improve the understanding of WEC array hydrodynamics and guide the design of WEC configurations. Child and Venugopal [2] applied wave field structure to an array design method and to the analysis of their results. Newman and Mei [25] plotted the wave amplitude across a row of nine floating bodies computed with WAMIT and showed wave amplitudes four times greater than the incident amplitude due to so called "trapped" waves. Although it was not a plot of the wave field explicitly, Folley and Whittaker [16] plotted the magnitude and direction of the total radiated wave for certain array arrangements and used the plots to discuss array performance. Kalen [13] produced plots of the wave elevation for arrays of 2, 7, and 420 point absorbers and used wave elevation at each WEC as an indicator of performance. Borgarino et. al [20] plotted the wave elevation of a single WEC and three WECs in their array configurations to show that at the optimal separation distance, certain WECs were in the peak of standing waves.

It was shown early in WEC research that a WEC could absorb power from an incident wave front much wider than its physical dimensions. For instance, a heaving axisymmetric WEC of any size can theoretically absorb energy from a width of the incident wave front equal to $\lambda/2\pi$, where λ is the wavelength [26]. This may seem physically unintuitive but is similar to the way in which an electromagnetic antenna can absorb power from an area wider than its physical width. Within the context of linear wave theory, power absorption is explained mathematically by the destructive interference of the generated wave

(combined diffracted and radiated waves) with the incident wave [27]. Because the generated wave travels outward from the WEC in a circular pattern, it interacts with the incident wave outside the physical dimensions of the WEC, which explains the capture width phenomenon and has implications on the size and shape of the wave shadow.

Recent papers have explored the process of energy extraction in the wave field in more detail. Wypych et al. [28] used analytical functions for radiated waves produced by heaving and surging point sources to compute the energy flux through a cylindrical control surface. From a wave field formulation, they were able to derive classical absorption equations for point absorbers. Farley [3] defined the term "generated wave," which he said is the sum of all waves both diffracted and radiated created by any number of power absorbing bodies. He plotted the wave field energy flux over a transect perpendicular to the direction of the incident wave propagation. He was also able to derive the classical limit of point absorber capture width. Most interestingly he showed that only the portion of generated wave that propagated in the direction of the incident wave is responsible for power capture. The wake or wave shadow of any single WEC or WEC array always has the same general form at a large enough distance from the devices, and that form is based on the power capture.

3 Methods

In this study, WEC motions and wave field properties are computed with linear water wave theory. Linear wave theory rests on two significant assumptions, first that the fluid can be described with potential flow and second that the free surface and body motions are small. The potential flow condition states that if the fluid can considered inviscid and irrotational, the fluid velocity vector can be reduced to the gradient of the scalar velocity potential. For the free surface to be small, the wave height must be much less than the wavelength and the water depth. For body motions to be considered small, the motion must be small with respect to the length scale of the body. The linear wave theory principle of superposition justifies the decomposition of the total velocity potential into velocity potentials due to the incident wave, the diffracted wave, and radiated waves [29].

The following subsections describe the boundary value problem of linear water wave theory, the formulation of the equations of body motion, and the computation of power absorption by the body and through energy flux in the wave field. Additionally, a simple theoretical WEC wave field is devised that serves to illustrate mathematically some of its key features. In addition to describing concepts, this section introduces the notation used throughout the document.

3.1 Boundary Value Problem

Consider an arbitrary number bodies floating in an inviscid irrotational fluid. A right-handed coordinate system is defined with positive z up, and the $x-y$ plane at $z = 0$ is the calm water surface. The fluid extends to infinity in all x and y directions, and there is a flat sea floor at $z = -h$. Because the fluid is inviscid and irrotational, it can be defined by a velocity potential, $\Phi(x, y, z)$, where the velocity of the fluid is the vector, $\mathbf{V} = \nabla\Phi$. Also assume the motions of the bodies and fluid to be small and harmonic with a frequency ω, so that $\Phi = \mathrm{Re}\{\phi e^{i\omega t}\}$,[2] where $i = \sqrt{-1}$ and ϕ is complex valued. The governing equation in the fluid domain (i.e. $-h \leq z \leq 0$ and external to all body boundaries) is Laplace's equation,

[2]Often in literature the time function is $e^{-i\omega t}$, which results in a slightly different set of equations. However, WAMIT uses $e^{i\omega t}$ and so that version shall be followed here.

$$\nabla^2\phi = 0$$

On the sea floor ($z = -h$), the no penetration condition states

$$\frac{\partial\phi}{\partial z} = 0$$

On the linearized free surface ($z = 0$), the dynamic and kinematic boundary conditions can be combined as

$$\omega^2\phi = g\frac{\partial\phi}{\partial z}$$

where g is the gravitational constant.

The velocity potential can be separated into components consisting of the incident wave potential, $A\phi_i$, the diffraction potential, $A\phi_d$, and radiation potentials due to motion in each degree of freedom, $\xi^j\phi_r^j$, where j is the index of the j^{th} motion. A is the complex amplitude of the incident wave. ξ^j is the complex amplitude of the j^{th} motion, and ϕ_r^j is the velocity potential due to unit amplitude, zero phase motion in mode j in otherwise calm water. ϕ_i is the velocity potential of a unit amplitude, zero phase incident wave and is equal to

$$\phi_i = i\frac{g}{\omega}\frac{\cosh k\,(h+z)}{\cosh kh}e^{-ik(\cos\beta\cdot x+\sin\beta\cdot y)} \tag{1}$$

where β is the direction of wave propagation and k is the wave number. k is related to the frequency by the dispersion relation

$$\omega^2 = gk\tanh kh$$

ϕ_d is the velocity potential of the diffracted wave that results from a unit amplitude, zero phase incident wave. Define the j^{th} mode of motion response to a unit amplitude, zero phase incident wave as ζ^j so that $\xi^j = A\zeta^j$. For floating bodies with a total of N degrees of freedom, the total velocity potential is

$$\phi = A\left(\phi_i + \phi_d + \sum_{j=1}^{N}\zeta^j\phi_r^j\right) \tag{2}$$

The incident and the diffracted potential satisfy the boundary value problem for all bodies held fixed. Call S the wetted surface of all bodies and $\frac{\partial}{\partial n}$

indicates the partial derivative in the direction of the body surface normal. By the no-penetration condition, on S the diffraction potential must satisfy

$$\frac{\partial \phi_d}{\partial n} = -\frac{\partial \phi_i}{\partial n}$$

Each radiation potential, ϕ_r^j, is found for the unit amplitude, zero phase motion j, which moves at a velocity $i\omega$ in an otherwise undisturbed fluid. On the wetted surface, S, motion j has a generalized normal $\mathbf{n}^j$, where $\mathbf{n}^j$ is a unit normal in the direction of the motion for translational modes and is the cross-product of the unit normal and vector about the point of rotation for rotational modes. On S, the radiation potential of the j^{th} motion satisfies the boundary condition

$$\frac{\partial \phi_r^j}{\partial n} = i\omega \mathbf{n}^j$$

Far from the bodies, the wave field should appear as the undisturbed or incident wave field, which means that the diffraction and radiation potentials must decay as the distance from the bodies increases. By energy conservation, the magnitude of the potential should decrease with inverse of the square-root of the distance. This is called the radiation boundary condition, and it is stated as

$$\phi_d,\ \phi_r^j \propto (kr)^{-1/2}\, e^{-ikr}\ as\ r \to \infty \tag{3}$$

where r is the radial distance from the body.

The velocity potential provides a complete description of the wave field. The complex fluid velocity amplitude is

$$\mathbf{v} = \nabla \phi \tag{4}$$

From the Bernoulli equation, the complex dynamic fluid pressure is

$$p = -i\omega\rho\phi \tag{5}$$

where ρ is the fluid density. And the complex wave elevation is

$$\eta = -\frac{i\omega}{g}\,\phi|_{z=0} \tag{6}$$

$$= \frac{1}{\rho g}\,p|_{z=0} \tag{7}$$

Additionally, the velocity potential can be used to compute the hydrodynamic forces and moments on the floating bodies. Just as the solution to the boundary value problem was divided into a diffraction problem and a radiation problem so too are the hydrodynamic forces. When the bodies are held fixed, the force or moment on each mode of motion, j, is the excitation force, F_{ex}^j, which is the integral over the wetted surface of the incident plus diffracted pressure in the direction of the generalized normal $\mathbf{n}^j$.

$$F_{ex}^j = \mathrm{Re}\left\{f_{ex}^j e^{i\omega t}\right\}$$

$$f_{ex}^j = -i\omega\rho A \int\int_S (\phi_i + \phi_d)\,\mathbf{n}^j dS$$

The radiation force on mode j, F_r^j, is slightly more complicated because it is the summation of the integrals of the pressure forces generated by motion in all modes including j.

$$F_r^j = \mathrm{Re}\left\{f_r^j e^{i\omega t}\right\}$$

$$f_r^j = \sum_{k=1}^{N} -i\omega\rho A\zeta^k \int\int_S \phi_r^k \mathbf{n}^j dS$$

For unit amplitude motion, the velocity of the motion j is $i\omega\mathbf{n}^j$, which means that from the radiation body boundary condition, $i\omega\mathbf{n}^j = \frac{\partial\phi_r^j}{\partial n}$. The radiation force can be rewritten as the force on mode j due to motion in k^{th} direction

$$f_r^{jk} = A\zeta^k \left[-\rho \int\int_S \frac{\partial\phi_r^j}{\partial n}\phi_r^k dS\right]$$

The quantity in the brackets is the complex radiation resistance matrix and is typically written in terms of the real added mass, $\mathcal{A}^{jk}$, and damping, $\mathcal{B}^{jk}$, coefficients.

$$-\rho \int \int_S \frac{\partial \phi_r^j}{\partial n} \phi_r^k ds = \omega^2 \mathcal{A}^{jk} - i\omega \mathcal{B}^{jk}$$

So the total force in mode j is the sum of the forces due to motions in mode k.

$$f_r^j = -A \sum_{k=1}^{N} \left(-\omega^2 \mathcal{A}^{jk} + i\omega \mathcal{B}^{jk} \right) \zeta^k$$

Since, $\dot{\zeta} = i\omega\zeta$ and $\ddot{\zeta} = -\omega^2\zeta$,

$$f_r^j = -A \sum_{k=1}^{N} \left(\mathcal{A}^{jk} \ddot{\zeta^k} + \mathcal{B}^{jk} \dot{\zeta^k} \right)$$

$\mathcal{A}^{jk}$ applies a force proportional to body acceleration and $\mathcal{B}^{jk}$ applies a force proportional to velocity, which explains the respective terminology, added mass and damping.

Diffraction and radiation velocity potentials are found from the linear water wave boundary value problem for an arbitrary number of floating bodies. From the potentials, wave field properties are found including wave elevation, pressure, and velocity. Wave pressure is used to compute the excitation force and added mass and damping coefficient matrices.

3.2 Equations of Motion

In the previous section, hydrodynamic forces and moments are described for an arbitrary number of floating rigid bodies with N degrees of freedom. Generally, one wants to know the amplitude and phase of the motions of the bodies in response to waves. And to find the total elevation of the wave field, one needs to know the complex body motions (see Eqns. 2 and 6). To compute the body motions, one also needs mass and mechanical properties of the bodies. The motions are solved with a linear equation for complex amplitudes in the frequency domain.

Again consider an arbitrary number of floating rigid bodies with N degrees of freedom. In matrix form, the equation of motion is

$$\mathbf{M}\ddot{\mathbf{X}} = \mathbf{F}_{hyd} + \mathbf{F}_{hs} + \mathbf{F}_{mech}$$

where $\mathbf{M}$ is an $N \times N$ matrix of masses or moments of inertia depending

on whether the mode of motion is translational or rotational, $\ddot{\mathbf{X}}$ is an $N \times 1$ vector of accelerations, and each $\mathbf{F}$ is an $N \times 1$ vector of forces, where the subscript *hyd* indicates hydrodynamic, *hs* indicates hydrostatic, and *mech* indicates mechanical forces.

As described in the previous section, the hydrodynamic force is the sum of excitation force and the radiation forces which can be written in terms of real added mass and damping coefficients.

$$\mathbf{F}_{hyd} = \mathbf{F}_{ex} - \boldsymbol{\mathcal{A}}\ddot{\mathbf{X}} - \boldsymbol{\mathcal{B}}\dot{\mathbf{X}}$$

where $\mathbf{F}_{ex}$ is an $N \times 1$ vector of exciting forces, $\boldsymbol{\mathcal{A}}$ is the $N \times N$ added mass matrix and $\boldsymbol{\mathcal{B}}$ is the $N \times N$ damping matrix. The hydrostatic force can be described by the product of an $N \times N$ stiffness matrix and the body displacements

$$\mathbf{F}_{hs} = -\mathbf{C}\mathbf{X}$$

The linear body forces are a damping force proportional to body velocity and a stiffness force proportional to body displacement,

$$\mathbf{F}_{mech} = -\mathbf{D}\dot{\mathbf{X}} - \mathbf{K}\mathbf{X}$$

where $\mathbf{D}$ is an $N \times N$ body damping matrix and $\mathbf{K}$ is an $N \times N$ body stiffness matrix. Moving all terms in $\mathbf{X}$ to the left-hand side, the equation of motion is written as

$$\left(\boldsymbol{\mathcal{A}} + \mathbf{M}\right)\ddot{\mathbf{X}} + \left(\boldsymbol{\mathcal{B}} + \mathbf{D}\right)\dot{\mathbf{X}} + \left(\mathbf{C} + \mathbf{K}\right)\mathbf{X} = \mathbf{F}_{ex}$$

Assuming the excitation force and motions to be harmonic with a frequency ω, $\mathbf{F}_{ex} = \mathrm{Re}\left\{\mathbf{f}_{ex}e^{i\omega t}\right\}$ and $\mathbf{X} = \mathrm{Re}\left\{\boldsymbol{\xi}e^{i\omega t}\right\}$, the equation of motion can be written as

$$\left[\mathbf{C} + \mathbf{K} - \omega^2\left(\boldsymbol{\mathcal{A}} + \mathbf{M}\right) + i\omega\left(\boldsymbol{\mathcal{B}} + \mathbf{D}\right)\right]\boldsymbol{\xi} = \mathbf{f}_{ex} \tag{8}$$

and so the complex amplitude vector of the motion in each degree of freedom is

$$\boldsymbol{\xi} = \left[\mathbf{C} + \mathbf{K} - \omega^2\left(\boldsymbol{\mathcal{A}} + \mathbf{M}\right) + i\omega\left(\boldsymbol{\mathcal{B}} + \mathbf{D}\right)\right]^{-1}\mathbf{f}_{ex} \tag{9}$$

3.3 Device Power

The total time-averaged power delivered by the waves to the array of WECs is the time average of the sum of the products of the hydrodynamic forces and the body velocities.

$$P = \frac{\omega}{2\pi} \int_0^{\frac{2\pi}{\omega}} \mathbf{F}_{hyd}^T \dot{\mathbf{X}} dt$$

where T indicates the transpose. In complex form this can be written as

$$P = \frac{1}{2}\mathrm{Re}\left\{i\omega \mathbf{f}_{ex}^* \boldsymbol{\xi}\right\} - \frac{1}{2}\omega^2 \boldsymbol{\xi}^* \boldsymbol{\mathcal{B}} \boldsymbol{\xi} \tag{10}$$

where * indicates the complex conjugate transpose. The first term in the power equation is the power absorbed by the bodies from the wave excitation force and the second term is the power radiated back into the wave field by waves generated by the bodies. When the excitation force (Eqn. 8) equation is substituted into Eqn. 10, the result is

$$P = \frac{1}{2}\omega^2 \boldsymbol{\xi}^* \mathbf{D} \boldsymbol{\xi} \tag{11}$$

For this reason, the mechanical body damping matrix, $\mathbf{D}$, is typically called the power-take-off (PTO) damping. The PTO damping determines how much power is absorbed by the floating bodies from the wave field.

Rather than computing the power for motions specified by equation 9, one can specify the motions and determine how it affects the power absorbed. Evans [6] showed that equation 10 can be rewritten as

$$P = \frac{1}{8}\mathbf{f}_{ex}^* \boldsymbol{\mathcal{B}}^{-1} \mathbf{f}_{ex} - \frac{1}{2}\left(i\omega\boldsymbol{\xi} - \frac{1}{2}\boldsymbol{\mathcal{B}}^{-1}\mathbf{f}_{ex}\right)^* \boldsymbol{\mathcal{B}} \left(i\omega\boldsymbol{\xi} - \frac{1}{2}\boldsymbol{\mathcal{B}}^{-1}\mathbf{f}_{ex}\right)$$

In this form, the body motions are part of an independent term. The power clearly reaches a maximum of (the first term)

$$P = \frac{1}{8}\mathbf{f}_x^* \boldsymbol{\mathcal{B}}^{-1} \mathbf{f}_x$$

when body motions are defined by

$$\boldsymbol{\xi} = -\frac{i}{2\omega}\boldsymbol{\mathcal{B}}^{-1}\mathbf{f}_x \tag{12}$$

because it results in the second term being zero. Motions found by the above

equation are the optimal motions that have been used frequently in WEC array studies. They can be computed for any array of WECs where the excitation force and radiation damping matrix are known.

3.4 Wave Energy Flux

Just as the power absorbed by the floating bodies can be computed from the body motions, it can also be computed from the wave field. Instantaneous power in a fluid is the product of pressure and a volumetric flow rate, where the volumetric flow rate can be formulated as the flux of the fluid through a control surface. If the pressure and velocity are harmonic with a frequency ω, the instantaneous power in the fluid or the wave energy flux is

$$\mathcal{F}_{inst} = \int_{CS} \mathrm{Re}\left\{pe^{i\omega t}\right\} \cdot \mathrm{Re}\left\{\mathbf{v}e^{i\omega t} \cdot \mathbf{n}\right\} ds$$

where p and $\mathbf{v}$ are the complex pressure and velocity amplitudes as before, and $\mathbf{n}$ is the unit normal of the control surface, CS. In the wave field, p, $\mathbf{v}$, and CS are functions of three dimensional space $\{x, y, z\}$ for $z \leq 0$. The time-averaged wave energy flux is

$$\mathcal{F} = \frac{\omega}{2\pi} \int_0^{\frac{2\pi}{\omega}} \int_{CS} \mathrm{Re}\left\{pe^{i\omega t}\right\} \cdot \mathrm{Re}\left\{\mathbf{v}e^{i\omega t} \cdot \mathbf{n}\right\} dsdt$$

which can be rewritten as

$$\mathcal{F} = \frac{1}{4} \int_{CS} \left(p\mathbf{v}^* \cdot \mathbf{n} + p^*\mathbf{v} \cdot \mathbf{n}\right) ds \tag{13}$$

where * indicates the complex conjugate. Eqn. 13 computes the flux through some arbitrary three-dimensional wetted control surface of a harmonically oscillating fluid with only the complex pressure and velocity amplitudes.

The wave energy flux of regular waves is computed by integrating the product of the pressure and velocity values along a vertical control surface that extends from the sea floor ($z = -h$) to the linearized free-surface ($z = 0$) [30]. Here, make the assumption that the vertical profiles of the pressure and velocity are of known forms $g_p(z)$ and $\boldsymbol{g}_{\mathbf{v}}(z)$ respectively, which can be separated functions of horizontal space, (x, y). The separation into functions of the vertical and horizontal variables can be performed for regular waves in the absence of submerged bodies. It also seems reasonable in the region outside of where the fluid is constrained in the z direction by a submerged body, in

other words, in the region with a free surface. The pressure can be written as the product of the surface pressure, $p_s(x,y)$ at $z=0$ and the vertical pressure function, $g_p(z)$. Likewise, the velocity can be written as a function of the velocity at the surface, $\mathbf{v}_s(x,y)$ and a vertical function, which in this case is a vector, $\boldsymbol{g}_{\mathbf{v}}(z)$.

$$p(x,y,z) = p_s(x,y)\, g_p(z)$$

$$\mathbf{v}(x,y,z) = \mathbf{v}_s(x,y)\, \boldsymbol{g}_{\mathbf{v}}(z)$$

Now, define the control surface, CS, to be everywhere perpendicular to planes of constant z, and to extend from the bottom, $z=-h$, to the linearized free surface, $z=0$. Its projection onto the plane $z=0$ would be an open or closed curve, which shall be called the control loop, CL. Just as the pressure and velocity functions were defined as the product of their values at the surface and a function of z, so too can the control surface, where at $z=0$ it is defined by the control loop CL and its depth function is $g_{CS}(z)=1$. CS is the constant CL at all water depths. Because CS does not change in the z direction, the normal in the z direction is zero over the entire surface, $n_z=0$, and the normals in x and y are constants with respect to depth. The dot product of the control surface normal and the velocity in Eqn. 13 is then

$$\mathbf{v}\cdot\mathbf{n} = u_s(x,y)\, g_u(z)\, n_x(x,y) + v_s(x,y)\, g_v(z)\, n_y(x,y)$$

where u_s is the velocity in the x direction at the surface $z=0$, v_s is the surface velocity in the y direction, g_u is the depth dependence of the x velocity and g_v is the depth dependance of the y velocity. Based off the equations for regular waves (see Eqn. 1, 4, and 5), the depth functions for pressure and velocity are all the same ($g_p(z) = g_u(z) = g_v(z) = g(z)$) and are all equal to

$$g(z) = \frac{\cosh k(h+z)}{\cosh kh} \tag{14}$$

Eqn. 13 can then be separated into the product of a depth integral and a integral around the control loop.

$$\mathcal{F} = \frac{1}{4}\int_{CL} \left(p_s \mathbf{v}_s^* \cdot \mathbf{n}_s + p_s^* \mathbf{v}_s \cdot \mathbf{n}_s\right) dl \int_{-h}^{0} g(z)^2\, dz$$

The depth integral is

$$\begin{aligned}\int_{-h}^{0} g\left(z\right)^2 dz &= \frac{1}{\cosh^2 kh}\int_{-h}^{0}\cosh^2 k\left(h+z\right)dz \\ &= \frac{c}{g}c_g\end{aligned}$$

where c is the phase speed of the wave, $c = \omega/k$, and c_g is the group velocity and is equal to

$$c_g = \frac{1}{2}\left(1+\frac{2kh}{\sinh 2kh}\right)\cdot c$$

Assuming the pressure and velocity have a depth dependence as defined by Eqn. 14, and that the control surface is uniform in z and defined by a control loop, CL, the average wave energy flux computed with complex pressure and velocity amplitudes at the linearized free surface is

$$\mathcal{F} = \frac{cc_g}{4g}\int_{CL}\left(p_s\mathbf{v}_s^*\cdot\mathbf{n}_s + p_s^*\mathbf{v}_s\cdot\mathbf{n}_s\right)dl \tag{15}$$

If the control loop is closed, encircles a group of floating bodies, and the normals point inwards, and the surface pressure and velocity values are found with Eqn. 2, 4, and 5, then the wave energy flux given by Eqn. 15 will equal the power absorbed by the bodies given by Eqn. 10.

For a regular harmonic wave propagating through an open-ended unit-width control surface, the dimensional energy flux is

$$\mathcal{F}_{reg} = \frac{1}{2}\rho g\left|A\right|^2 c_g \tag{16}$$

which can be found by combining Eqns. 1, 4, 5, and 15 for a wave of complex amplitude, A.

3.5 Theoretical WEC Wave Field

In order to illustrate the features of the WEC wave field and provide a mathematical background, a simple theoretical WEC wave field is devised. It consists of an incident regular wave and a circular wave that represents the combined diffracted and radiated waves. Although it may be simplified, it is a reasonable approximation of the linear WEC wave field.

In general, the total wave elevation is

$$\eta_t = \eta_i + \eta_d + \sum \xi^j \eta_r^j$$

First, consider just the diffracted and radiated waves, which propagate outwards from the WEC. Define the cylindrical coordinates $\{r, \theta, z\}$, where

$$x = r\cos\theta$$

$$y = r\sin\theta$$

$$z = z$$

In cylindrical coordinates, the boundary value problem of a circular wave can be solved with a separation of variables. Waves propagating radially outward have magnitudes in the radial direction defined by the Hankel function of kr [28]. Within a few wavelengths of the source, the Hankel function can be approximated as $(kr)^{-1/2} e^{ikr}$. The approximation represents circular waves whose magnitude decays at a rate that preserves the wave energy flux through ever increasing circumferences (i.e. it satisfies the radiation condition). Additionally, a complex directional dependence function, $f(\theta)$, is defined. A general circular wave can then be approximated as

$$\eta = \frac{f(\theta)}{(kr)^{1/2}} e^{-ikr} \tag{17}$$

The $f(\theta)$ function has been used frequently to describe the angular variation of the radiated as well as the diffracted wave field in WEC literature (e.g. [5, 7, 8]). It is often called the far-field angular dependence as it is typically only applied at large radial distances, but may be valid near the device. $f(\theta)$ is a function of the geometry of the device and the mode of motion that produces the radiated wave field. In this document it shall be called the generated wave function, because it describes the angular variation of a wave generated by the device. The wave may be due to device motions (radiation), diffraction, or the combination of radiation and diffraction.

Consider the diffracted and all radiated waves to be of the form of Eqn. 17, so that the wave field is then

$$\eta_t = \eta_i + \frac{f_d(\theta)}{(kr)^{1/2}} e^{-ikr} + \sum \xi^j \frac{f_r^j(\theta)}{(kr)^{1/2}} e^{-ikr}$$

All the circular waves can be combined into a single circular wave, modified by a single generated wave function,

$$\eta_t = \eta_i + \frac{f(\theta)}{(kr)^{1/2}} e^{-ikr}$$

where

$$f(\theta) = f_d(\theta) + \sum \xi^j f_r^j(\theta)$$

The WEC wave field for a single device can be considered as the superposition of a planar incident wave and circular wave. The wave field of a WEC array could also be approximated as such in the far-field if all waves radiated from the group come from approximately the same origin. Farley [3] claims that $f(\theta)$ is a universal function for any group of WECs, and can be used to determine the WEC wave field and the power capture.

As an example, take the incident wave field as the unit amplitude, zero phase case, propagating at an angle $\beta = 0$. The complex generated wave function, $f(\theta)$ is the sum of the complex responses of the diffracted wave and the various radiated waves due to the unit amplitude, zero phase, incident wave propagating in the direction $\beta = 0$. The total wave is then

$$\eta_t = e^{-ikr\cos\theta} + \frac{f(\theta)}{(kr)^{1/2}} e^{-ikr} \tag{18}$$

Of primary interest in this paper is the spatial variation of the magnitude of the total wave field. The magnitude of Eqn. 18 is

$$|\eta_t| = \sqrt{1 + \frac{|f(\theta)|^2}{kr} + \frac{2|f(\theta)|}{(kr)^{1/2}} \cos\left(kr(\cos\theta - 1) + \epsilon_f(\theta)\right)} \tag{19}$$

where $|f(\theta)|$ and $\epsilon_f(\theta)$ are the magnitude and phase of $f(\theta)$, respectively. What wave field patterns can be deduced from Eqn. 19? How does magnitude of the wave elevation vary spatially? First, as the distance from the origin increases ($kr \to \infty$), the magnitude of the wave field goes to 1 (the magnitude of the incident wave) as it should. Second, in the region near the WEC, there are peaks in the wave field when the argument of the cosine term is equal to

an integer multiple of 2π. That is, there are standing wave peaks when

$$kr\left(\cos\theta - 1\right) + \epsilon_f\left(\theta\right) = \pm 2\pi n \tag{20}$$

If ϵ_f is defined from $0 \leq \epsilon_f < 2\pi$, and $r > 0$ ($r = 0$ causes a singularity in Eqn. 17 and so is undefined in the domain), the left hand side of Eqn. 20 is always less than 2π, and so the positive symbol on the right-hand side is eliminated and $n = 0, 1, 2, 3, \ldots$. Using Cartesian coordinates, Eqn. 20 becomes

$$y = \pm\sqrt{\frac{2}{k}\left(2\pi n + \epsilon_f\left(\theta\right)\right)x + \frac{1}{k^2}\left(2\pi n + \epsilon_f\left(\theta\right)\right)^2} \tag{21}$$

Of course, the standing wave pattern also contains troughs which are found as

$$y = \pm\sqrt{\frac{2}{k}\left(2\pi\left(n - \tfrac{1}{2}\right) + \epsilon_f\left(\theta\right)\right)x + \frac{1}{k^2}\left(2\pi\left(n - \tfrac{1}{2}\right) + \epsilon_f\left(\theta\right)\right)^2} \tag{22}$$

Note that the first trough ($n = 0$) is only valid when $\epsilon_f\left(\theta\right) \geq \pi$.

Farley showed that the power absorbed (or radiated) by a WEC can be computed from the value of the generated wave function at $\theta = 0$ [3], that is, in the direction that the incident wave propagates. Following his derivation, the power absorbed by the wave (and thus the WEC) described by Eqn. 18 is

$$P_{farley} = -\frac{2\sqrt{\pi}\left|f\left(0\right)\right|}{k}\left(\sin\epsilon_f\left(0\right) + \cos\epsilon_f\left(0\right)\right) - \frac{1}{k}\int_0^{2\pi}\left|f\left(\theta\right)\right|^2 d\theta \tag{23}$$

where $\epsilon_f\left(0\right)$ is the phase of the circular wave in the direction of incident wave propagation. The power absorbed reaches a maximum when $\epsilon_f\left(0\right) = \frac{5\pi}{4}$, which is the optimal phase of the wave. An interesting aspect of the value of the phase that Farley points out is that, for the two-dimensional case (i.e. when the generated wave in long-crested), the optimal phase is π, so that the generated wave cancels perfectly with the incident wave. However, for the combination of a circular wave with an incident planar wave, the phasing is offset from π by $\pi/4$ or $1/8$ of the wavelength.

As a simplification, consider the generated wave function to be a constant with respect to direction, $f\left(\theta\right) = f$, which would be the case for the radiated wave of an axisymmetric device operating in heave. Equations 21 and 22 (ϵ_f is a constant) then describe a family of parabolas symmetric about the x-axis and increasing towards positive x. These are the same set of parabolic

standing waves, that Child and Venugopal describe and exploit in the Parabolic Intersection method [2]. For the heaving WEC wave ($f(\theta) = f$) operating with the optimal wave phase, $\epsilon_f(0) = \frac{5\pi}{4}$, the absorbed power is

$$P_{farley} = \frac{2\sqrt{2\pi}}{k}|f| - \frac{2\pi}{k}|f|^2 \tag{24}$$

Equation 24 is quadratic in $|f|$ and has a maximum at $|f| = \frac{\sqrt{2\pi}}{2\pi}$, at which the power captured is $P_{farley} = \frac{\lambda}{2\pi}$. $\frac{\lambda}{2\pi}$ is the well know optimum capture width for a WEC operating in heave [26]. Another interesting facet of the optimal amplitude and phase of the generated wave is that they are constants with respect to wave frequency. The optimal motions of the device are functions of frequency, but that is because of the frequency dependence of the hydrodynamic forces. Essentially, the device motions have to change as a function of frequency so as to produce the same generated wave at all frequencies.

Figure 3 shows wave fields for the heaving WEC operating at optimal amplitude for different radiated wave phases (ϵ_f). The wave fields are plots of $|\eta_t|$ at a wavelength, $\lambda = 2$, as given by Eqn. 19. Also, superimposed on the plot are red and blue parabolas located on the crests and troughs respectively of the standing waves. The phase and power absorption are given above each figure. A negative power absorption means that power is radiated rather than absorbed. For only three of the phases shown does the WEC wave absorb power ($\epsilon_f = \pi$, $\epsilon_f = 5\pi/4$, and $\epsilon_f = 3\pi/2$). The phase $\epsilon_f = 5\pi/4$ is the optimal phase at which the power absorption is $P = 0.32 = \lambda/2\pi$. As the value of the phase increases, the parabolas widen, and shadow forms inside the aft-most parabolic crest. The aft-most parabolic trough and the region inside it constitutes what shall be referred to as the wave shadow. It is interesting to observe how the wave shadow changes with phase. Note that at $\epsilon_f = \pi$ and $\epsilon_f = 3\pi/2$, the wave absorbs the same amount of power, but the wave shadows look different. At $\epsilon_f = 3\pi/2$, the wave shadow is clearly a parabola and in between its arms the wave elevation increases back to almost the incident elevation. At $\epsilon_f = \pi$, the final parabola has been swept back until it collapsed into line and the wave shadow loses its "V" shape.

In its most simple form, the WEC wave field is formed by the interaction between a planar incident wave and a circular generated wave. The question remains though: how good of an approximation is the circular wave to the radiated and diffracted waves of a real device? The following sections attempt

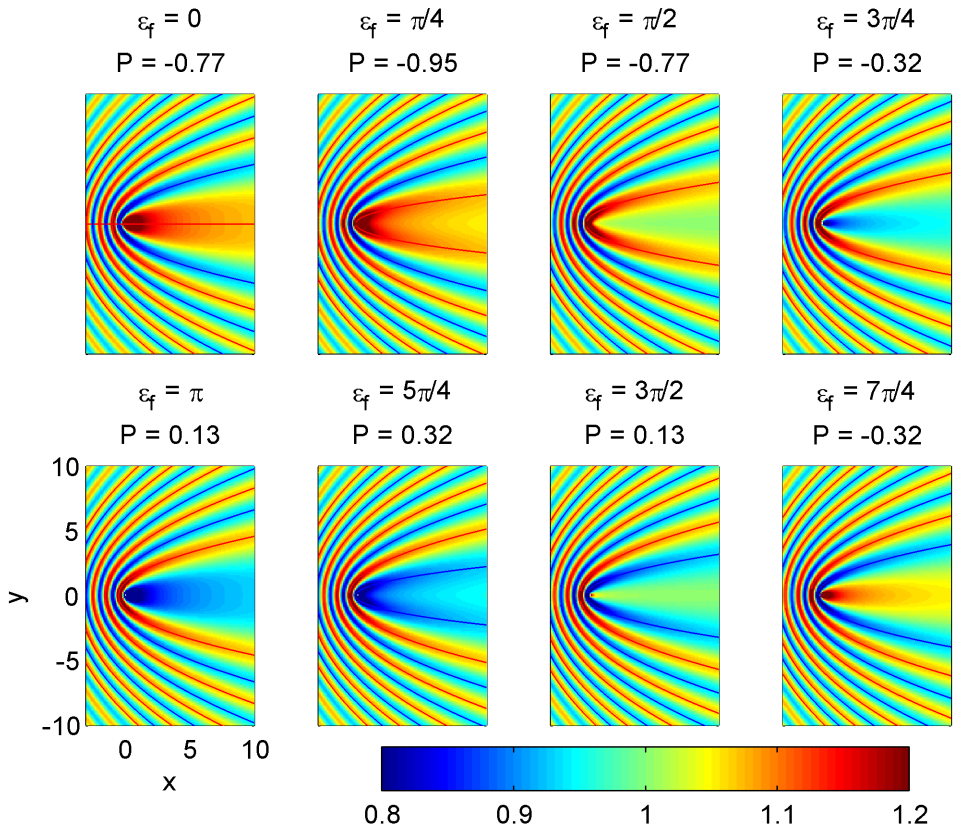

Figure 3: The figures show the magnitude of the wave elevation $|\eta_t|$ at a wavelength of $\lambda = 2$ at different phases of the generated wave. The phase and power absoption are given above each figure. A negative power absoption means that power is radiated rather than absorbed.

to answer that question by computing the radiated and diffracted wave fields for simple geometries and by comparison with experimental data.

3.6 WEC and Wave Field Computation

The linear wave BEM software WAMIT is used to solve the boundary value problem described in Sec. 3.1 for a given geometry. Hydrodynamic forces from WAMIT are combined with mechanical forces to solve for body motions as described in Sec. 3.2. WAMIT also returns separate radiation and diffraction[3] pressures, and velocity vectors at user specified field points. The diffracted wave field computed by WAMIT is the wave field due to a unit amplitude, zero phase incident wave (ϕ_d from Sec. 3.1). Radiated wave fields are computed in each degree of freedom, j, for unit amplitude, zero-phase motions (ϕ_r^j from Sec. 3.1). Body motions are combined with the field quantities to produce wave fields as described in Sec. 3.1.

In addition to being functions of the wetted geometry, diffracted and radiated wave fields are functions of the radial frequency, ω. Diffracted wave fields are also functions of the incident wave direction, β, which is measured in degrees, counter-clockwise from the positive x-axis. However, because the radiated wave fields computed by WAMIT are for unit-amplitude, zero-phase body motions, they are independent of incident wave direction. Radiated wave fields become functions of direction when they are multiplied by directionally dependent body motions. Body motions can also be computed for unit-amplitude, zero-phase incident waves, and then the sum of the incident, diffracted, and radiated waves in each degree of freedom can be scaled by the complex incident wave amplitude, A (see Eqn. 2).

For regular waves, the wave field is typically represented by the wave elevation, η, as a function of space. Because wave elevation is complex valued, it can be plotted in a color map as either the real part, which represents the wave at an instant in time, or as the magnitude, which shows the size of the wave. Magnitude plots are typically used for visualizing standing wave patterns and the wave shadow. Two wave fields are of significant interest: the incident plus diffracted, $\eta_i + \eta_d$, and the total wave field, $\eta_t = \eta_i + \eta_d + \sum \eta_r^j$. The incident plus diffracted is the wave field of the fixed device, which does not absorb power, and the total wave field is that of power absorbing device. Unless otherwise specified, the wave fields are for unit-amplitude, zero-phase

[3]What WAMIT refers to as the diffracted wave field is herein referred to as the incident plus diffracted wave field. Therefore to compute the diffracted wave field defined by this document, one needs to subtract the incident (Eqn. 1) wave field from the WAMIT diffracted wave field.

incident waves.

In addition to computing the wave field for regular waves, spectral wave fields are considered by evaluating multiple wave components at different frequencies and directions and applying an amplitude to the incident wave as defined by a wave spectrum. Consider the spectral representation of the incident wave field to be $S_i(\omega, \beta)$. At a given frequency and direction, (ω, β), the magnitude of incident wave amplitude is

$$|A(\omega, \beta)| = \sqrt{2S_i(\omega, \beta)\,\Delta\omega\Delta\beta} \tag{25}$$

where $\Delta\omega$ and $\Delta\beta$ are the bin widths at the given frequency and direction respectively. For the phase of the incident wave amplitude, random values can be chosen from a uniform distribution between 0 and 2π. The phase is only relevant when considering the real part of the wave. And so for a given incident wave spectrum, $S_i(\omega, \beta)$, the total wave field is created with Eqn. 2 where the magnitude of the of the wave amplitude is defined by Eqn. 25.

The incident wave amplitudes scale the resulting wave fields over the computed range of frequencies and directions. Within the wave field at each location, there is a spectral representation of the wave field over the range of frequencies and directions computed. The spectral representation of the total wave field is

$$S_t(\omega, \beta) = \frac{1}{2}\frac{|\eta_t(\omega, \beta)|^2}{\Delta\omega\Delta\beta}$$

At any given point, a spectrum can be computed and plotted. In order to visualize the entire spectral wave field simultaneously, the bulk parameter of the zeroth-moment significant wave height is plotted over the grid of field points. In order to accurately understand the wave field, it is important to study both the significant wave height as well as wave spectra.

4 Results

In this section, WEC wave fields are shown for three independent but interrelated studies. In the first, generic wave field patterns and techniques for analyzing the wave field are described using a heaving cylindrical WEC. Similar patterns are found in the second study, which is a comparison of WEC array experiment results to a computational model. The computational wave field proved quite useful for interpreting the experimental data and the data validates the existence of the modeled wave shadow. In the final set of results, the linear computational WEC wave field is compared to wave fields produced by a phase-averaged computational wave model, SWAN, which helps to frame the range of applicability of the phase-averaged model.

4.1 Generic WEC Wave Field

As an initial investigation, a generic WEC operating in a single degree of freedom is used in order to keep the results as general as possible. The WEC model is selected to be cylinder of diameter, d, and draft, l, allowed to operate only in heave. Results are shown for three regular wave cases and two spectral seas cases. Each regular wave case is for a different device diameter to wavelength ratio. The spectral seas cases are for unidirectional irregular waves and irregular waves spread over direction. Wave fields are presented as color plots of elevation or significant wave height, transects of wave elevation or energy flux, and wave spectra for irregular waves. Energy flux through the wave field is computed and the results are displayed graphically.

All motions, forces, and wave field properties are made nondimensional by ρ, g, and d. The nondimensional quantities are indicated by an apostrophe, $'$. The mechanical spring force shall be taken as zero, $K = 0$, and the nondimensional equation of motions for a cylindrical WEC operating only in heave is

$$\xi' = \frac{f'_{ex}}{\frac{\pi}{4} - \omega'^2\left(\frac{\pi}{4}l' + \mathcal{A}'\right) + i\omega'\left(\mathcal{B}' + D'\right)} \tag{26}$$

where $\xi' = d^{-1}\xi$, $f'_{ex} = \rho^{-1}g^{-1}d^{-3}f_{ex}$, $l' = d^{-1}l$, $\mathcal{A}' = \rho^{-1}d^{-3}\mathcal{A}$, $\mathcal{B}' = \rho^{-1}g^{-1/2}d^{-5/2}\mathcal{B}$, $D' = \rho^{-1}g^{-1/2}d^{-5/2}D$, $\omega' = g^{-1/2}d^{1/2}\omega$. Also define the nondimensional coordinates, $x' = d^{-1}x$, $y' = d^{-1}y$, and $z' = d^{-1}z$.

The critical geometric parameter is the nondimensional draft $l' = l/d$.

Cylinders with large nondimensional drafts are typically referred to as spars and have very low resonant frequencies, which makes them stable in the typical range of ocean wave frequencies and they are often used for offshore structures such as oil platforms. WECs should respond actively to ocean waves, and as such a heaving cylindrical WEC should have a low nondimensional draft. In this case the nondimensional draft is taken as $l' = 1/2$.

In addition to the parameters of the equation of motion, the following nondimensional wave field parameters are defined, $\lambda' = d^{-1}\lambda$, $k' = dk$, $h' = d^{-1}h$, $A' = d^{-1}A$, $\phi' = g^{1/2}d^{-3/2}\phi$, $p' = \rho^{-1}g^{-1}d^{-1}p$, $\mathbf{v}' = g^{-1/2}d^{-1/2}\mathbf{v}$, $\eta' = d^{-1}\eta$. The nondimensional wavelength is related to the nondimensional wave number by $\lambda' = 2\pi/k'$, the nondimensional wave number is related to the nondimensional frequency by the nondimensional dispersion relation

$$\omega'^2 = k' \tanh k'h'$$

and the nondimensional group velocity is, $c'_g = g^{1/2}d^{-3/2}c_g$. For this study, a nondimensional water depth of $h' = 4$ is used because this would, for instance, represent a $10m$ diameter full scale WEC in $40m$ of water, which seems typical.

The power absorbed by the WEC and the energy flux through the wave field are nondimensionalized as $P' = \rho^{-1}g^{-3/2}d^{-7/2}P$, and $\mathcal{F}' = \rho^{-1}g^{-3/2}d^{-7/2}\mathcal{F}$ respectively. Unless otherwise specified for the remainder of Sec. 4.1, all quantities shall be the nondimensional quantities and the word "nondimensional" shall be left out. Power absorption by the WEC shall occur through a linear power take-off (PTO) damping,

$$P' = \frac{1}{2}\omega'^2 D' \left|\xi'_x\right|^2$$

For a given set of incident wave conditions, there is a D' value that maximizes the amount of power absorbed by the WEC. At and near the resonant frequency, the optimal D' can lead to motions that are very large. Just as the amplitude of optimal motions can be considered unrealistically large, so too can the motions for the optimal D' value. A heaving cylinder does not move at these predicted large amplitudes because of nonlinear effects and hydrodynamic viscous forces. In order to make the motions of the heaving WEC more realistic, a suboptimal D' value is chosen. For this study, the value of $D' = 0.15$ is used.

A plot of $|\xi'/A'|$, or the response amplitude operator (RAO), for the heaving

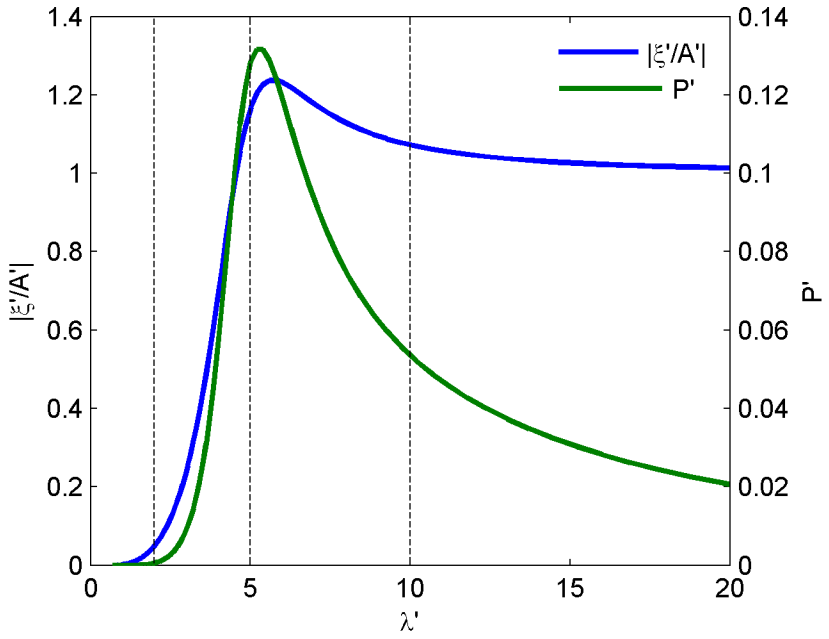

Figure 4: The RAO, $|\xi'/A'|$, is shown in blue and corresponds to the left-hand axis, and the WEC power absorption, P', is shown in green and its axis is on the right.

WEC as a function of wavelength is shown as the blue line in Fig. 4. The RAO indicates the relative motion response of the WEC at different frequencies. For long waves, $|\xi'/A'| \approx 1$, which means the WEC mostly follows the motion of the waves. At a wavelength slight greater than $\lambda' = 5$, there is a resonant peak, and for short waves, the WEC motion goes to zero. The green line in Fig. 4 shows the power absorption of the WEC as a function of wavelength. The peak of the power absorption occurs near the resonant frequency, and power absorption decays for both longer and shorter waves. The RAO and power curves are typical of heaving WECs with linear PTO.

4.1.1 Regular Waves

Figure 5 shows the real part of four wave fields, the incident, $\mathrm{Re}\{\eta_i'\}$, the diffracted, $\mathrm{Re}\{\eta_d'\}$, the radiated, $\mathrm{Re}\{\eta_r'\}$, and the total, $\mathrm{Re}\{\eta_t'\}$ in different rows, at three different wave lengths, $\lambda' = 2$, $\lambda' = 5$, and $\lambda' = 10$ in different columns. These wavelengths are indicated by the vertical dashed lines in Fig. 4. The axes in all of the plots in Fig. 5 are the same; the x-axis is x'/λ' and the y-axis is y'/λ', where the limits in both the x-axis and y-axis go from

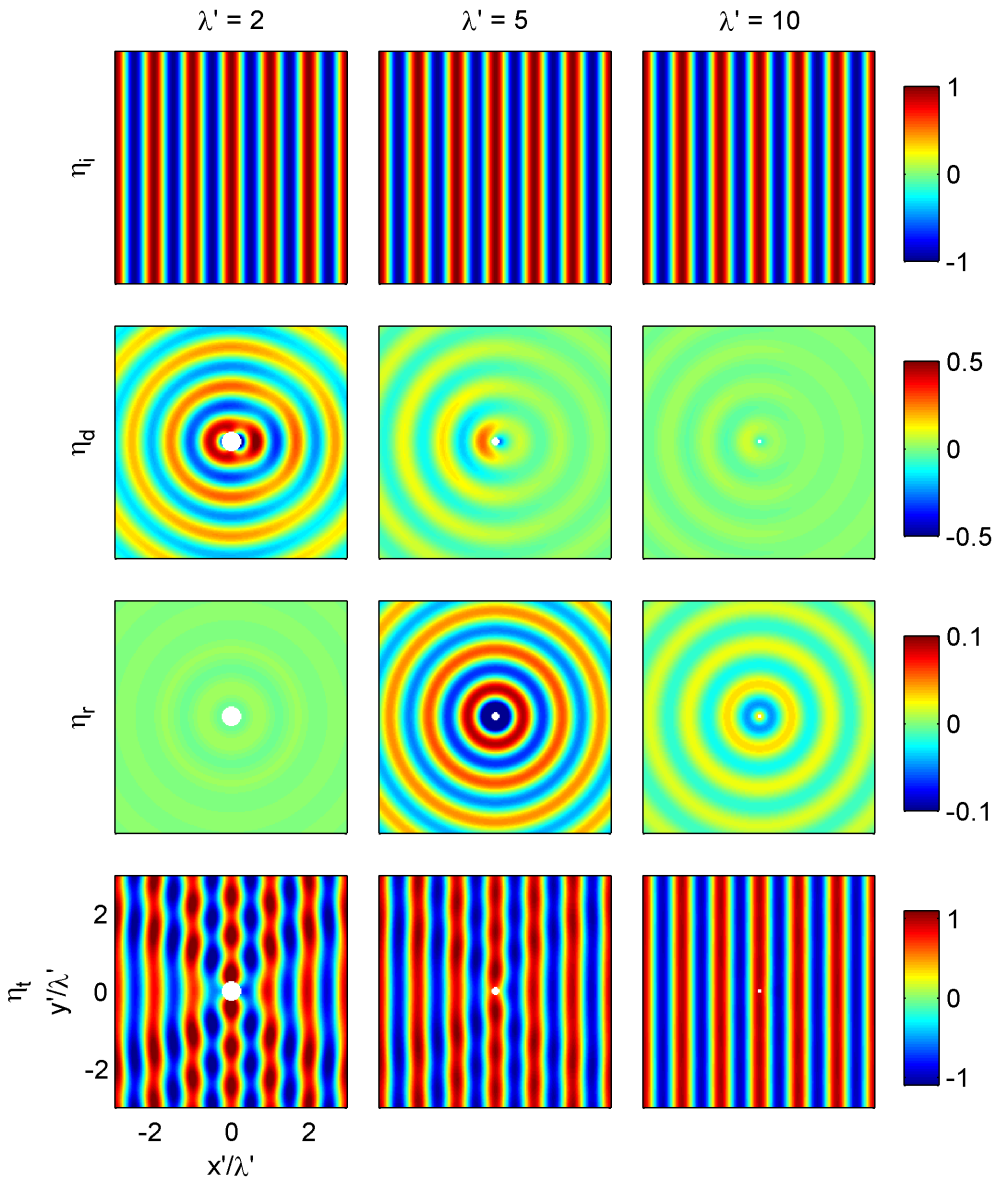

Figure 5: The figure shows real values of the incident, $\mathrm{Re}\{\eta_i\}$, the diffracted, $\mathrm{Re}\{\eta_d\}$, the radiated, $\mathrm{Re}\{\eta_r\}$, and the total, $\mathrm{Re}\{\eta_t\}$, wave fields at $\lambda' = 2$, $\lambda' = 5$, and $\lambda' = 10$. The real values are the instantaneous wave elevation at time $t = 0\ s$.

-3 to 3, and are shown in the bottom left hand figure. The axes scaling was designed so that six wavelengths fit in the wave field regardless of λ'. A result of this scaling is that the cylinder appears to shrink with increasing λ' (figures from left to right). An equally valid perspective is that the field of view is "zoomed-out" with increasing λ'.

The real part of η shows the wave elevation at time $t = 0$. In all figures, one can clearly see periodic wave patterns. The incident wave field (top row) is clearly a planar regular wave. It appears the same for all wavelengths because the incident wave is independent of the body geometry. The diffracted (second row) and radiated (third row) wave fields have an obvious circular pattern, which is periodic in the radial direction. The angular variation of the diffracted wave field is interesting. It appears as if the wave is not circular (note the asymmetry from left to right), but the wave field can still be represented by the complex generated wave function, $f(\theta)$, where the magnitude and phase changes from the front to the back of the device (left to right in the figure), because of the directionality of the incident wave. Because the device is axisymmetric and operating in heave, the radiated wave field is isotropic, which mathematically means that is has a constant generated wave function, $f(\theta) = f$, as discussed in Sec. 3.5.

Comparison of each type of wave field at different wavelengths helps to illustrate fundamental WEC concepts. The color scaling is the same across columns but varies between rows and is indicated by the color bars on the right. The diffracted wave field has the largest amplitude for the shortest wavelength, and is very weak for the longest wavelength. The point-absorber assumption states that if the wavelength is much greater than the device dimensions, the diffracted wave can be neglected, which may be reasonable in this example at the longest wavelength.

The radiated wave elevation is a function of the device geometry and the amplitude of the device motion at a given frequency. Insight into the radiated waves can be gained from Fig. 4. At $\lambda' = 2$, the relative motion and power absorption of the WEC are very small, at $\lambda' = 5$, the motion and power absorption are near the maximum, and at $\lambda' = 10$ the motion and power absorption are moderate. The radiated wave fields shown in Fig. 5 follow the same trend. It is almost nonexistent at $\lambda' = 2$ where the power absorption is very close to zero. It is maximized at $\lambda' = 5$, and slightly smaller at $\lambda' = 10$. In linear wave theory, while the phase of the wave is critical, in order to absorb

energy from the wave field, a finite amplitude radiated wave is required.

The bottom row of figures show the total wave elevation, which is the real part of the sum of the complex incident, diffracted, and radiated wave elevations. One can see waves that are nearly regular but are modulated in magnitude with respect to space, which indicates the presence of standing waves. The modulation of the waves is more discernible at the shorter wavelengths. However, it is difficult to learn a great deal from these figures. A plot of the magnitude of the wave elevation, makes the standing wave effect much more clear.

Figure 6 shows the magnitude of the combined incident and diffracted wave fields, $|\eta_i' + \eta_d'|$, and the total wave field, $|\eta_t'|$. The combined incident and diffracted wave field is significant because it is the wave field of a fixed device, for which, the wave field is modified, but no energy is removed. In Fig. 6 all plots have the same color scaling. The magnitude is centered around 1, which is the magnitude of a unit-amplitude incident wave. All plots show with varying degrees of intensity, standing waves in the form of parabolas where the crests are shown in hot colors and the troughs in cool colors. These are the parabolic formations described in Sec. 3.5 and used by Child and Venugopal [2] in the Parabolic Intersection method. The height of the standing waves decreases with increasing wavelength. The shortest wavelength produces the most intense standing waves, and in the plot of the longest wavelength, the standing waves are almost nonexistent.

It is interesting to compare the wave field of the fixed cylinder (top row of Fig. 6) to that of the energy extracting WEC (bottom row). For $\lambda' = 2$, both wave fields appear identical, which is not surprising because at this wavelength, the WEC hardly moves at all (see Fig. 4). At $\lambda' = 5$, the WEC moves a great deal and absorbs a large amount of energy. This energy absorption is clearly visible by comparing the incident and diffracted wave field to the total wave field. In the plot of the incident and diffracted wave field, most of the effect on the wave field occurs in front of the device in the form of reflection and there is little shadowing. In the plot of the total wave field, there is a distinct parabolic wave shadow in the lee of the device. For the longest wave, $\lambda' = 10$, there does not appear to be much of a shadow in either of the wave fields, but the effect of energy extraction seems to be that the standing waves in front of the WEC are smaller than those of the fixed WEC. That is, it reduces the amount of wave reflection.

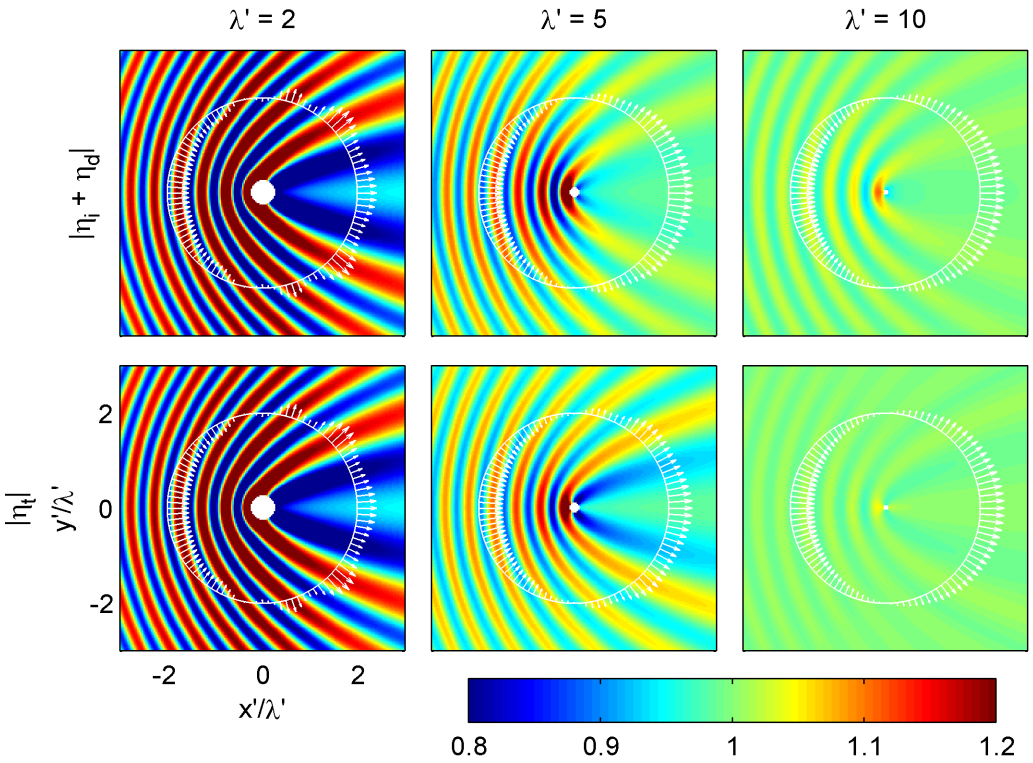

Figure 6: The figures show magnitudes of the wave elevation for a fixed cylinder, $|\eta_i + \eta_d|$, and for the heaving WEC, $|\eta_t|$, at three wavelengths, $\lambda' = 2$, $\lambda' = 5$, and $\lambda' = 10$. Parabolic standing wave patterns and a parablic wave shadow are visable. The waves shadow is most apparent in the plot of $|\eta_t|$ at $\lambda = 5$, which is where the WEC absorbs the most energy. The white circles represent control surfaces, each has a radius equal to two wavelengths, and the white vectors are graphical representations of the wave energy flux through the control surface where the direction of the arrow is the direction of the control surface normal and the arrow length is the magnitude of the energy flux at that point.

Also shown in Fig. 6 are white circles and vectors, which are graphical representations of the wave energy flux through a cylindrical control surface surrounding the WEC. The energy flux through the wave field is computed with Eqn. 15. As mentioned at the end of Sec. 3.4, the energy flux through a control surface surrounding a WEC should be equal to the power absorbed by the WEC. The computed values of WEC power (Eqn. 11) and energy flux through the wave field (Eqn. 15) are within 0.5 % of one another. The agreement serves to verify the method of computing energy flux as well as the accuracy of the wave field. The vectors in the figures point in the directions of the control surface normals and the magnitudes of the vectors, including the signs, are the magnitudes of the flux at those points on the control surface. A vector pointing inward indicates a net energy flux into the control surface and a vector pointing outward indicates a net flux out. One can see variation in the magnitude of flux along the control surface corresponding to the magnitude of the standing wave through which the control surface passes. This is most apparent behind the WEC in the $\lambda' = 2$ plots. The differences between the magnitude of the vectors of the fixed case as compared to the power absorbing case appears quite small, but this is because the power absorption is small. At $\lambda' = 5$, the power absorption is $P' = 0.13$, which means that only 13 % of the wave power incident to the WEC is absorbed.

The $\lambda' = 2$ case is also significant because even though there is no energy extracted, the presence of the device significantly modifies the wave field including the creation of a parabolic wave shadow. There are also large standing wave ridges. Energy lost in the wave shadow is recuperated at other locations in the wave field, so that the net wave energy flux is nearly zero. The WEC modifies the wave field by reflecting and diffracting waves without extracting energy. This effect on the wave field shall be termed wave scattering, and is more prevalent at short wavelengths.

Another useful way to visualize the wave field is through transects of the wave elevation or energy flux. A longshore transect of the wave elevation is simply a plot of η' as a function of y' at a constant x', or a slice of the wave field at a constant x'. A cross-shore wave elevation transect is a slice of the wave field at a constant y'. A longshore energy flux transect is the flux of energy through a planar control surface at a constant x'. The energy flux is related to the wave elevation, but because the flux computation includes directionality they are not linearly proportional to one another. One method

of approximating energy flux through the wave field is to assume that the waves are planar and are propagating in the direction of the incident waves, so that the energy flux can be computed by applying the complex wave elevation at field points, η', to Eqn. 16 through a delta width in the longshore, $\Delta y'$. This is relevant because in phase-averaged wave models, such as SWAN, the waves are planar by definition and the planar wave approximation is the only means of computing energy flux. In nondimensional form, the planar wave energy flux approximation is

$$\mathcal{F}'_{pl-ap} = \frac{1}{2} |\eta'|^2 c'_g \Delta y' \tag{27}$$

Figure 7 compares the shoreward energy flux computed by Eqn. 15 to the planar wave flux approximation, Eqn. 27, across five longshore transects at $x'/\lambda' = -1, 0, 1, 2, 3$ for $\lambda' = 5$. $x'/\lambda' = -1$ is an offshore transect, $x'/\lambda' = 0$ is a transect that cuts through the WEC, and the other three transects are in the lee of the WEC. In the lee of the WEC, the planar wave flux approximation and the true flux are in reasonable agreement. However near the WEC and in front of it, the difference between the two is quite large. In all regions, the energy flux is not as large as that predicted by the planar wave approximation because the planar wave approximation assumes that all the energy is traveling toward the WEC, while in reality the radiated and diffracted energy is directed radially outwards from the WEC. The difference between the two is most significant offshore because the difference between the direction of the incident and of the radiated and diffracted waves is the greatest. Even though there may be large variation in the wave height in the longshore, the variation in the net wave energy flux relatively small. In the lee, the incident, radiated, and diffracted waves are traveling in mostly the same direction, and so the wave height is a reasonable indicator of the wave energy flux.

The pattern of the wave energy flux in the lee of the WEC is of a particular shape that appears to expand as the distance behind the WEC increases. Compare the longshore transects at $x'/\lambda' = 1$, 2, 3 in Fig. 7. The transects of $x'/\lambda' = 2$ and $x'/\lambda' = 3$ appear to be a stretched version of the transect at $x'/\lambda' = 1$. This is the same transect shape and stretching pattern is described by Farley [3] for any generic system of WECs.

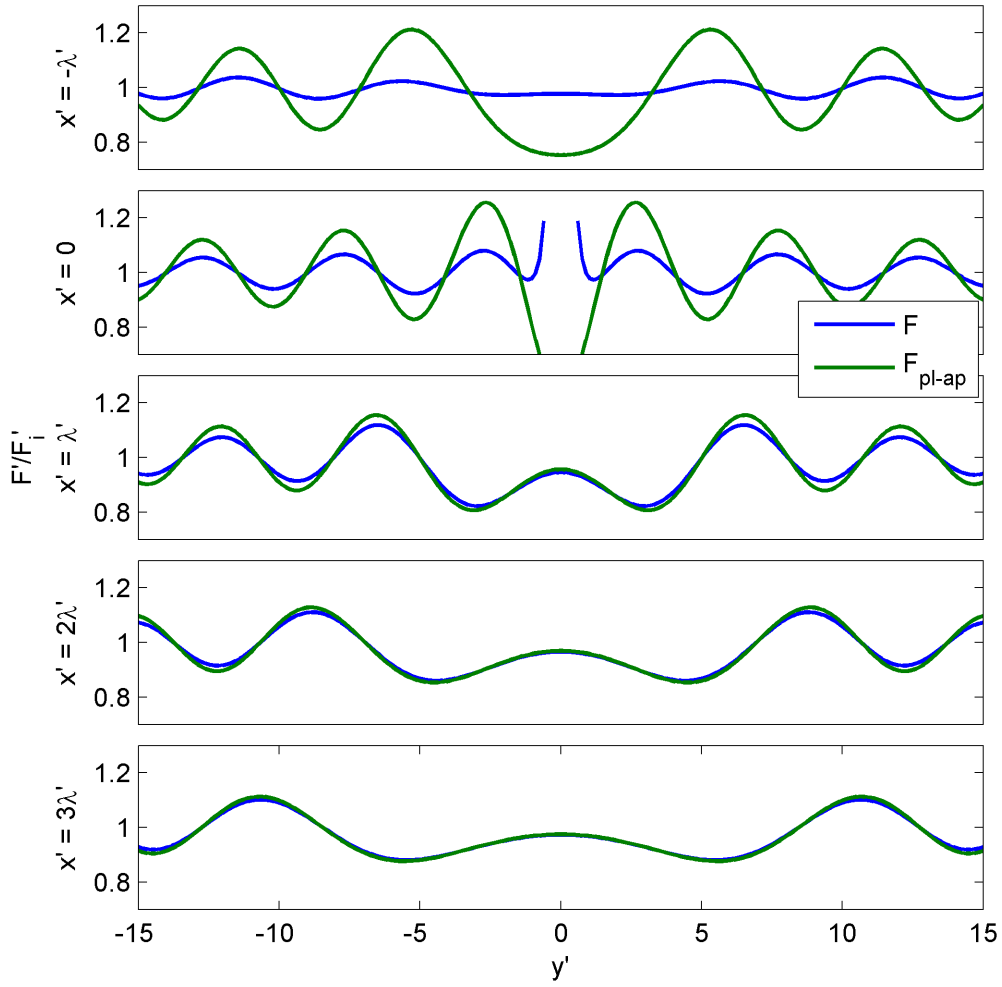

Figure 7: The figure shows longshore transects of wave energy flux computed using Eqn. 15 compared to transects of the planar wave approximation of wave energy flux computed using Eqn. 27. The wavelength is $\lambda' = 5$, and transects are shown at one wavelength in front of the device, through the device, and at one, two, and three wavelengths behind the device. The y-axis is the wave field flux normalized by the incident flux.

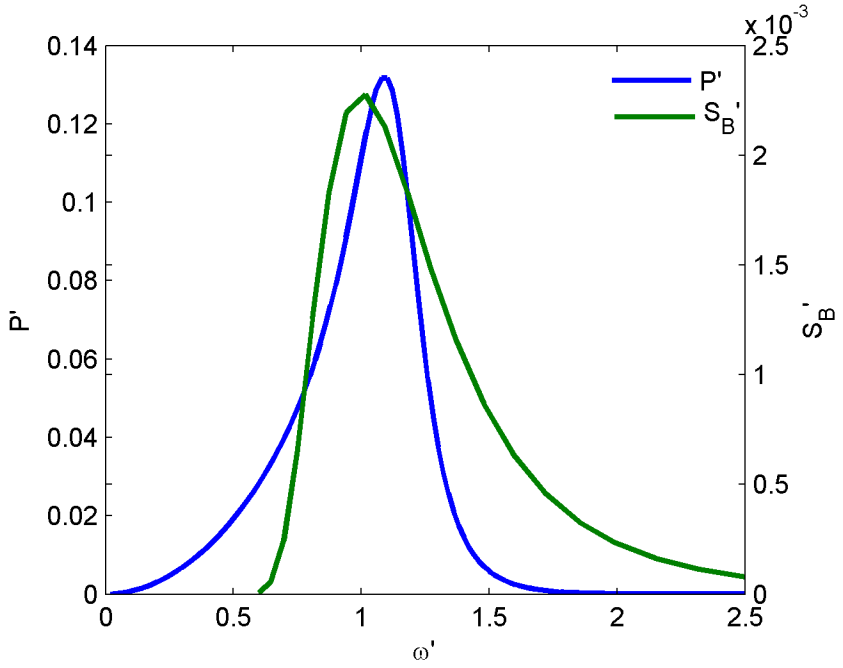

Figure 8: The figure shows the non-dimensional incident wave spectrum (S'_B) and WEC power absorption curve P'.

4.1.2 Spectral Seas

To examine the irregular wave field, a spectrum is applied to incident wave components as described in Sec. 2.1. Consider the nondimensional Bretschneider spectrum

$$S'_B(\omega) = \frac{1.25}{4}\frac{\omega'^4_m}{\omega'^5}H'^2_s e^{-1.25(\omega'_m/\omega')^4}$$

where ω'_m is the nondimensional modal frequency, H'_s is the nondimensional significant wave height, and the parameters are made nondimensional as $S'_B = g^{-1/2}d^{-5/2}S_B$, $\omega'_m = g^{-1/2}d^{1/2}\omega$, and $H'_s = d^{-1}H_s$. First, consider the long-crested case, in which all wave components are traveling in the direction $\beta = 0°$. The modal frequency is chosen to be near the resonant frequency of the device, $\omega'_m = 1$, and the significant wave height is chosen as $H'_s = 0.5$. The spectrum and power absorption curve as a function of frequency are shown in Fig. 8.

Figure 9 shows the significant wave height of the wave field for the fixed WEC case ($\eta'_i + \eta'_d$) and for the power absorbing WEC (η'_t). The significant wave height is normalized by the incident wave significant wave height, H'_s/H'_{s-in}, so that in regions of green, the significant wave height of the wave

field is the same as that of the incident. Although, there are still thin parabolic ridges in the offshore, the clearly defined parabolic standing wave patterns of regular wave fields are mostly smoothed out in significant wave height. There is also a clear parabolic wave shadow for both the fixed cylinder and total wave fields. Even a device not absorbing power creates a wave shadow due to wave scattering. The wave shadow of the power absorbing WEC is more intense and extends further in the lee than that of the fixed WEC. Also interesting is that the fixed WEC creates an intense peak in the wave height immediately in front of and around itself. However, this peak appears to be significantly diminished for the power absorbing WEC. By absorbing power, the WEC not only increases the wave show in its lee, but also reduces reflection in the offshore.

Examining the significant wave height wave field only tells part of the story. At each field point, there is a complete wave spectrum. In the total wave field of Fig. 9, white dots indicate points at which wave spectra are examined, three between the WEC and the wave source, or offshore, and three behind the WEC, or in the lee. Each set is numbered 1 through 3 with increasing y'. The spectra along with the original incident wave spectrum are shown in Fig. 10. First, examine the lee spectra. Spectrum "Lee 2" is taken from within the wave shadow. It shows a uniform reduction in wave energy across almost all frequencies, meaning that for most frequencies, there is a wave shadow here. In contrast, spectrum "Lee 3" shows almost no reduction in energy, because at this point, there is no wave shadow for most frequencies. "Lee 1" is quite interesting, because it shows a reduction in energy at some frequencies but a gain in energy at others. This phenomenon will become more clear in the examination of the offshore spectra.

The energy density of all offshore spectra oscillates between being less than and being greater than the incident energy as a function of frequency. This is most apparent in "Offshore 3," which is in line with the WEC and the wave propagation. The oscillations in spectral energy are the result of spatial variations of the peaks and troughs of standing waves at different frequencies. At a given point in space, some wave frequencies will have a standing wave trough and others will have a peak. Figure 11 helps to visually explain this phenomenon. It shows cross-shore transect of the wave elevation at five frequencies for the position $y' = 0$, which cuts through the WEC, offshore spectrum 3 and lee spectrum 3. In Fig. 11, the position of the WEC is indi-

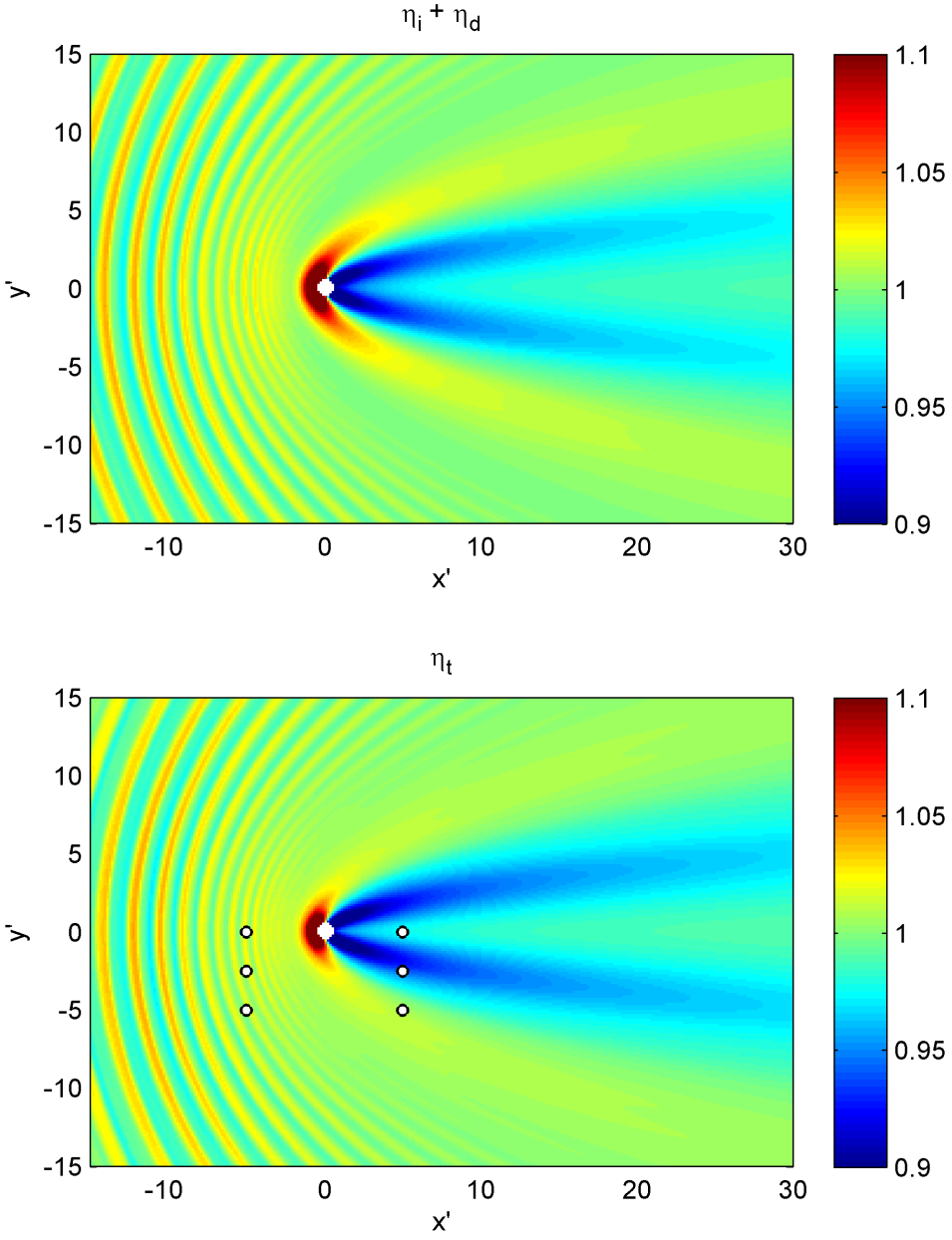

Figure 9: The figures show the normalized significant wave height (H'_s at field points divided by the incident H'_{s-in}) for the WEC held fixed ($|\eta_i + \eta_d|$) at the top and the power absorbing WEC ($|\eta_t|$) at the bottom in the non-directional spectral wave field. The incident wave spectrum is shown in Fig. 8. In the total wave field figure, the white dots indicate the locations at which wave field spectra are examined. The offshore spectra occur at $x' = -5$ and the lee spectra are at $x' = 5$. The spectra labeled 1 are located at $y' = -5$, 2 at $y' = -2.5$, and 3 at $y' = 0$.

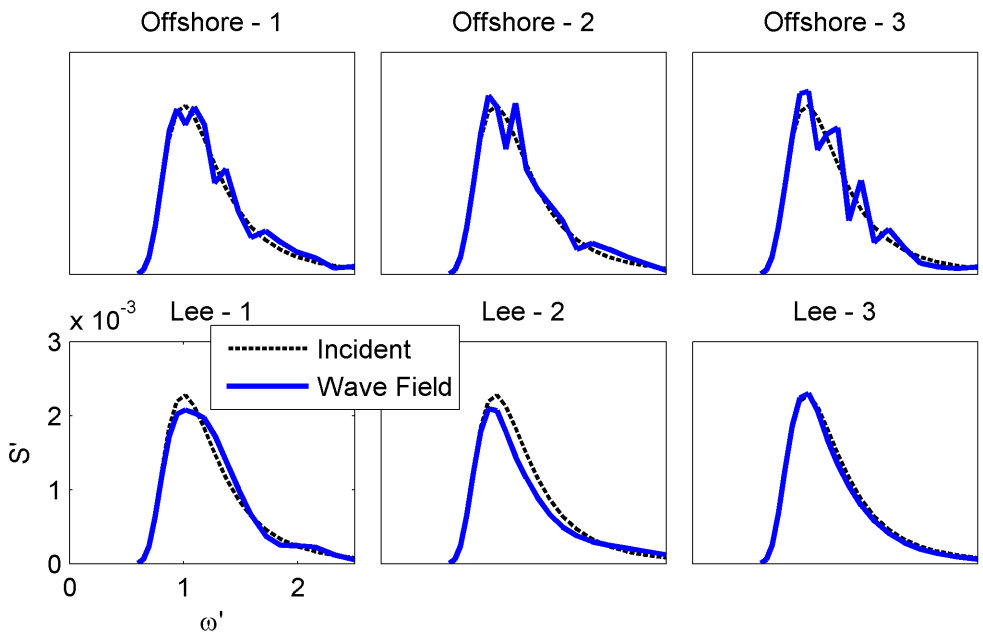

Figure 10: Figures show the field spectra for the power absorbing WEC along with the incident wave spectrum. The locations can be seen in Fig. 9. Note the spikes in the offshore spectra, while the lee spectra are smooth.

cated by a hole in the elevation, and the positions of the spectra are vertical solid lines. The horizontal dashed line shows the magnitude of the incident wave component at that given frequency. At $\omega' = 0.94$, "Offshore 3" is located at a peak of a standing wave, and the spectrum shows a corresponding peak in Fig. 10. At $\omega' = 1.09$, "Offshore 3" is located in the trough, and the spectrum shows a hole. At $\omega' = 1.18$, "Offshore 3" is near a node and the spectrum is almost the same as the incident. The pattern continues as such. The magnitudes and locations of the peaks and troughs are dependent on the generated wave function, $f(\theta)$, which depends on the WEC geometry, motions, and precise location.

Now consider a spectrum with directional spreading defined by the function

$$G(\beta) = \gamma \cos^{2s}\left(\tfrac{1}{2}\beta\right) \quad for \quad -180^\circ < \beta \leq 180^\circ$$

$$\gamma = \frac{\Gamma(s+1)}{2\sqrt{\pi}\Gamma\left(s+\frac{1}{2}\right)}$$

where the coefficient γ normalizes the area of $G(\beta)$ to 1 and Γ is the gamma function. s is a parameter that defines the width of spreading. A lower value of

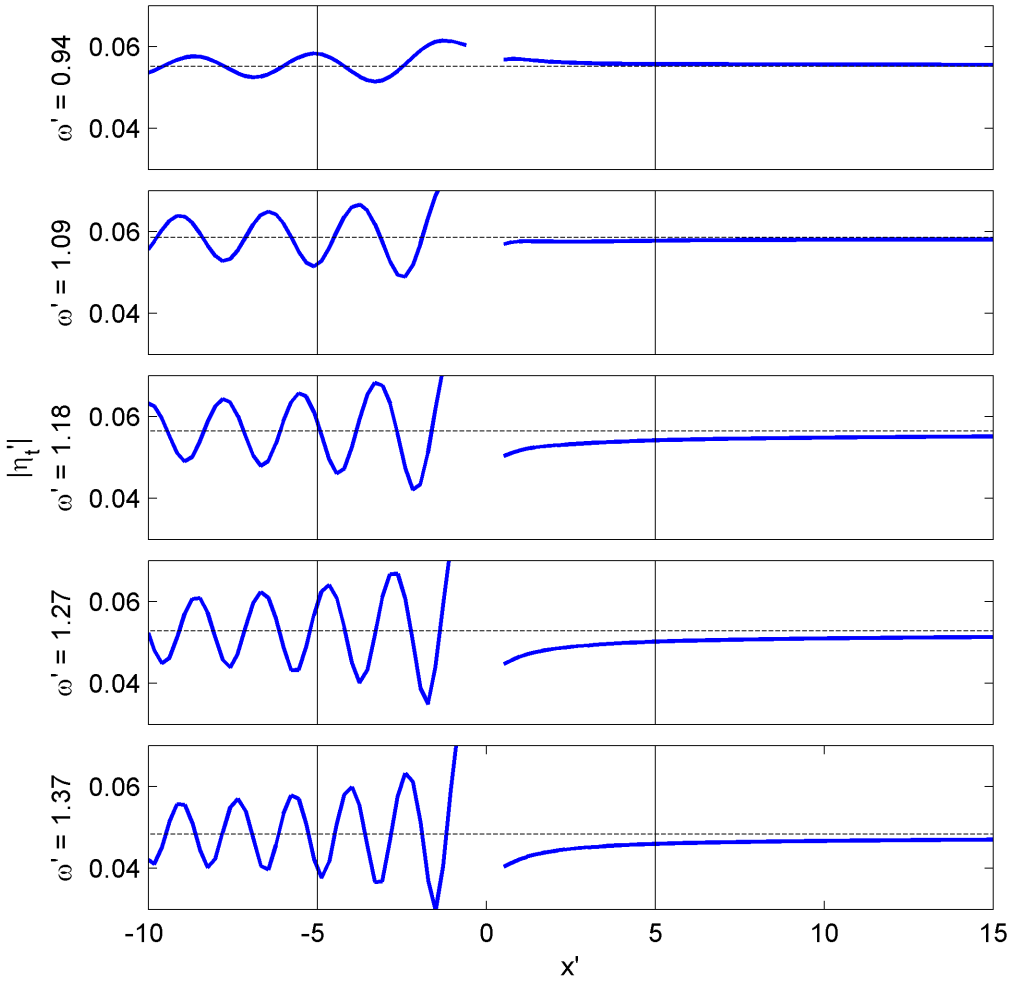

Figure 11: The figures show cross-shore transects at $x' = 0$ of the magnitude of the wave elevation of the total wave field for different frequencies. The hole in the elevation is the location of the WEC, and the vertical lines indicate the locations where spectra were examined. Note how the magnitude varies at each freqeuncy at the location of the offshore spectrum. This is causes the spikes in the offshore spectra.

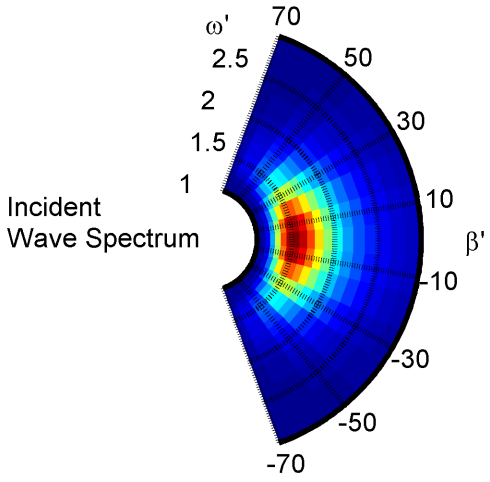

Figure 12: The figure shows the incident wave spectrum for the directional case.

s makes the directional spreading broader. As an example of spread spectrum wave field, take $s = 10$ as shown in Fig. 12. The resulting wave fields are shown in Fig. 13 as plots of the significant wave height for the fixed WEC and the power absorbing WEC. The wave fields in both figures are even more smooth than they were for the unidirectional case, and the parabolic wave shadow has become an egg shape. As with the unidirectional case, the shadow of the power absorbing WEC is greater than that of the fixed WEC and the reflection is reduced.

Figure 14 shows the directional spectra taken at field points. As with the unidirectional case, the offshore spectra are highly variable in energy density with peaks and troughs as a function of frequency and direction. The lee spectra are much more orderly in their shape. It is interesting to note that the direction of the peak of the wave energy shifts with position in the lee of the WEC. For instance, for "Lee 1" the peak is about 10°, while incident peak is at 0°. This is not too surprising; the WEC blocks wave energy from directions of 0° or less, but would do little to block energy traveling at positive directions. Perhaps if a WEC design is very directionally dependent, an array designer may want to orient WECs in the second row of an array so that they point outwards.

Wave fields around a generic heaving WEC are examined computationally. Patterns including parabolic standing waves, wave shadows, and frequency

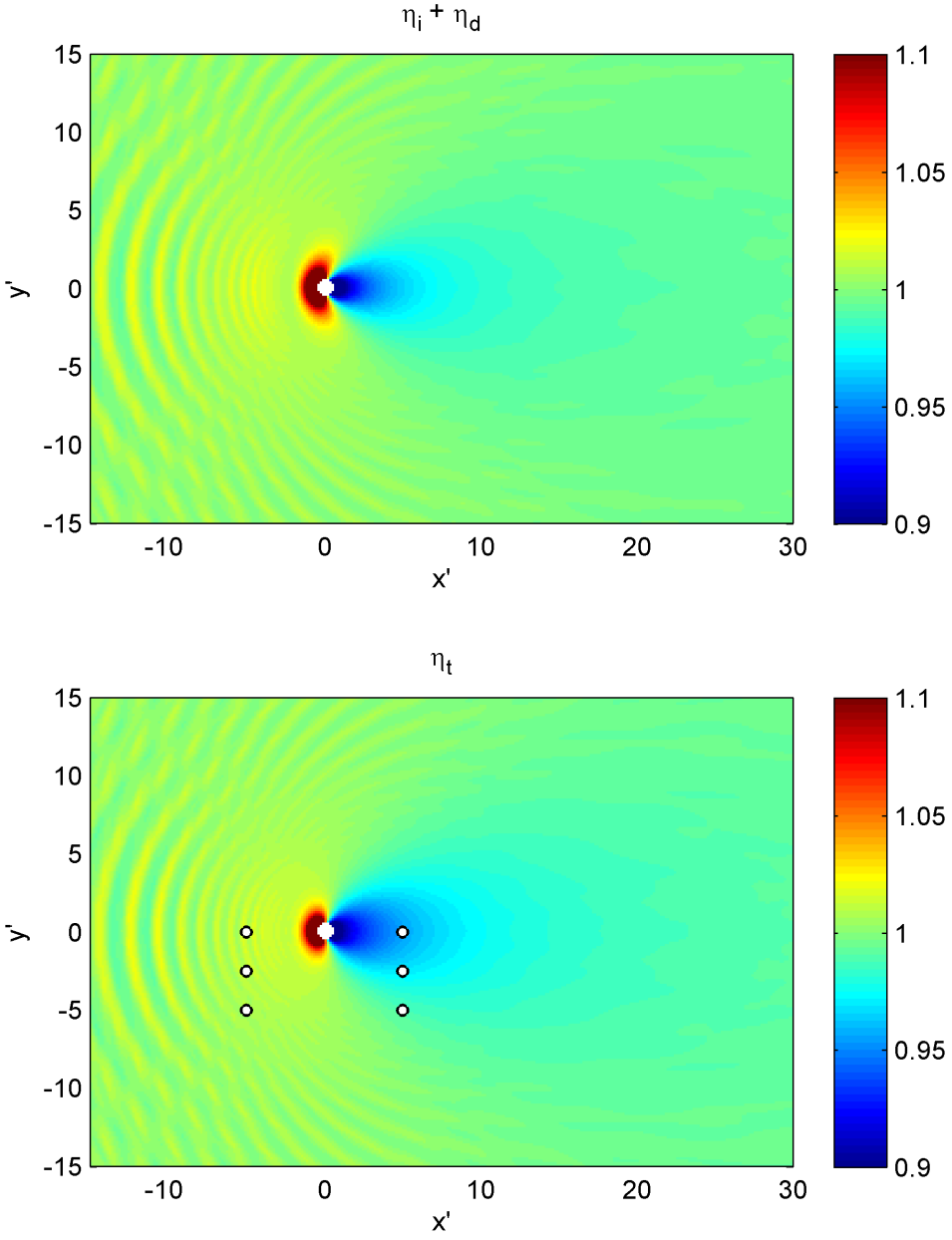

Figure 13: The figures show the normalized significant wave height (H_s' at field points divided by the incident H_s') for the WEC held fixed (incident plus diffracted) at the top and the power absorbing WEC (total wave field) at the bottom in the directional spectral wave field. The incident wave spectrum is shown in Fig. 12. In the total wave field figure, the white dots indicate the locations at which wave field spectra are examined. The offshore spectra occur at $x' = -5$ and the lee spectra are at $x' = 5$. The spectra labeled 1 have are at $y' = -5$, 2 are at $y' = -2.5$, and 3 are at $y' = 0$.

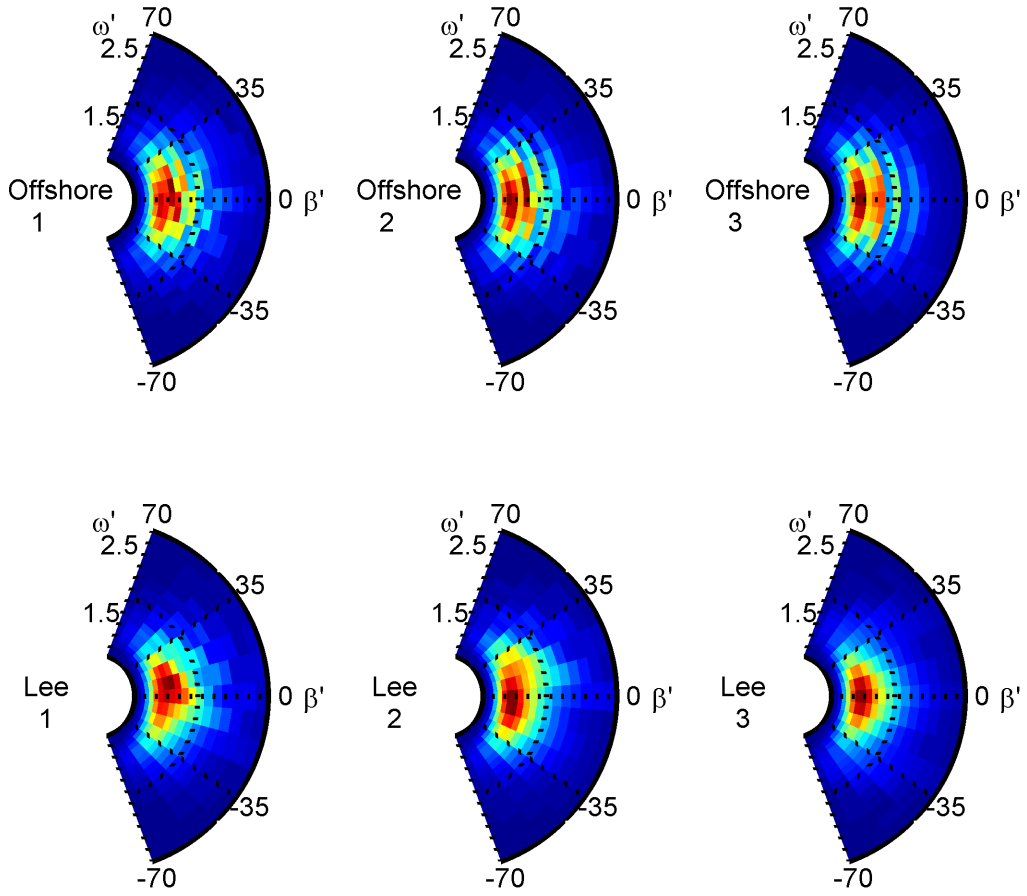

Figure 14: The figures show the wave field spectra for the directional incident wave case. The locations of the spectra can be seen in Fig. 13.

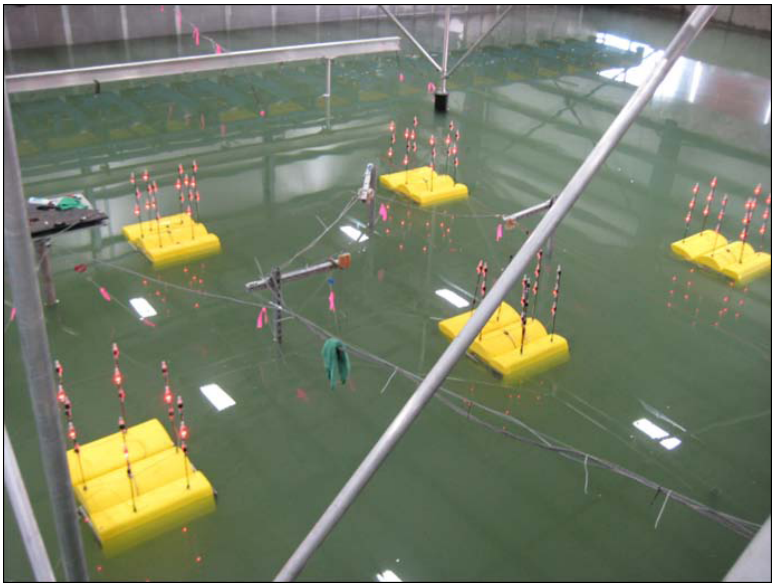

Figure 15: The photo shows the WEC array experiment for the 5 WEC case conducted in the O.H. Hinsdale Tsunami Wave Basin at Oregon State University [1].

dependent spikes in offshore spectra are described. Many of these patterns are also found in the WEC array experimental data described in the next section.

4.2 Experimental Wave Field Analysis

Over the winter of 2010-11, Oregon State University and Columbia Power Technologies, Inc. (CPT) conducted experiments on scale models of the CPT WEC design "Manta" in the O.H. Hinsdale Tsunami Wave Basin. Tests were performed on a single WEC as well as WEC arrays in a variety of wave conditions and extensive measurements were made of the wave field with a variety of instruments. A picture of the experiment is found in Fig. 15, and Fig 16 shows the experimental layout including the location of the WECs and wave gauges. The experimental wave conditions include regular waves at different frequencies and amplitudes, and irregular waves from seven sea states with and without directional spreading. A list of the regular wave conditions and the sea states of the irregular wave conditions is found in Table 1. The experiment is described by Haller et al. [1]. Experimental data presented here was provided by Porter, and details on the data analysis can be found in his Masters thesis [31]

In Sec. 4.1, modeling of the wave field around a generic WEC produced

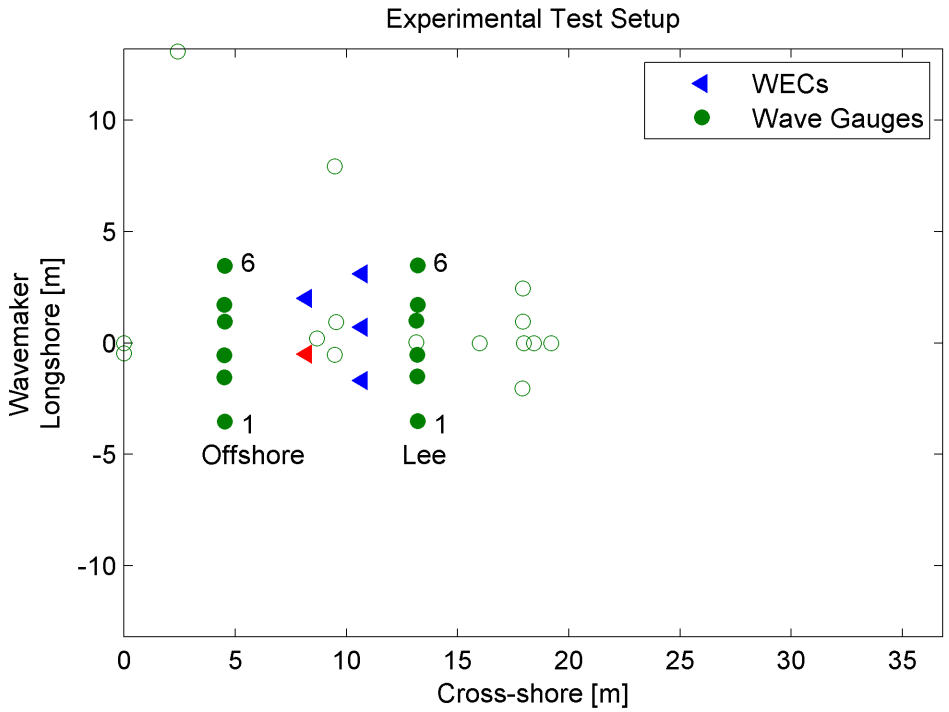

Figure 16: The figure shows tests experimental layout of the WEC array tests. The location of the WEC for the single WEC tests is shown as the red triangle. The filled-in circles indicate the offshore and lee wave gauges at which comparisons are made. Empty circles are gauges present in the experiment but not used in this analysis.

interesting information about wave field characteristics including parabolic standing wave formations, wave shadows, and modification of the offshore and lee wave spectra. The data from the WEC Array tests provides a valuable resource for validating the existence of these wave field patterns. Many of the wave field patterns are somewhat non-intuitive, and so computational modeling also aides in the interpretation and analysis of the experimental wave field data.

In order to model the WEC array experiments, a geometric model of the physical WEC under test is required. The actual physical model is described by Haller et al. [1] and is shown in Fig. 17. Because of proprietary issues and time limitations, a simple cylindrical WEC (also shown in Fig. 17) was adopted as the geometry for the computational model. Although the cylinder is a very rough approximation of the physical model, it was believed that a computational model with the cylinder could still provide useful information

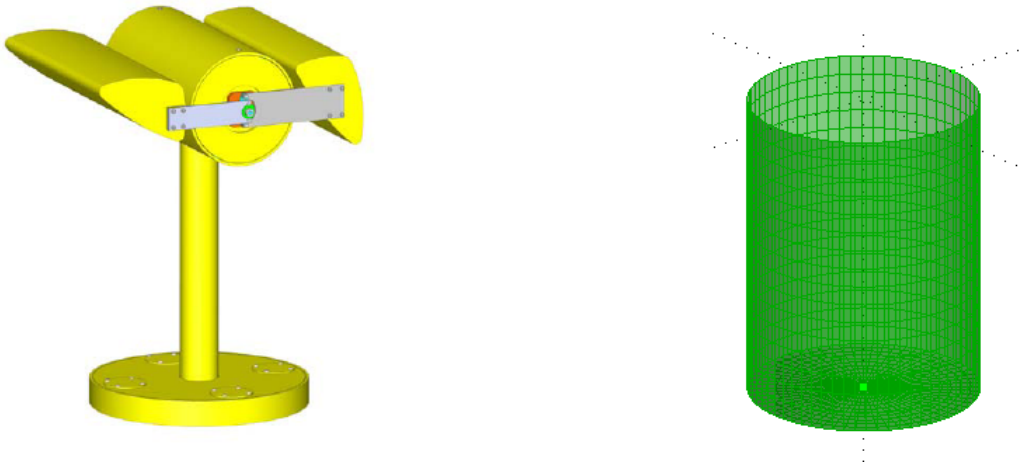

Figure 17: On the left is the Manta geometry that was used in the WEC array tests [1] and on the right is the cylinder that was used as the computational model.

about the WEC wave field. In order to make the cylindrical model similar to the physical model, three things were designed into it. First, the dimensions of the cylinder were chosen to match the approximate size of the physical model. The diameter and draft of the computational model WEC were selected as $d = 0.6\,m$ and $l = 0.8\,m$ respectively. Secondly, the single degree-of-freedom mode of motion was chosen to be surge because surge most closely resembles the power absorbing motion of the WEC under test. The power absorption curve of the surging cylindrical WEC is closer in shape to that of the physical model than are the power curves for other modes of motion. Finally, a PTO damping was chosen for the computational model WEC so that the power absorbed was of the same approximate magnitude with a peak at approximately the same frequency as the physical model. The dimensional damping value is $D = 2000kg/s$, and the power absorption curve and RAO of the computational model WEC are shown in Fig. 18. In this case, the power absorption is plotted as the relative capture width (RCW), which is the ratio of wave power absorbed by the device to the wave power incident to the device's width.

The modeled wave field domain is the same size as the Tsunami Wave Basin. The water depth is a uniform $h = 1.4\,m$. No effort was made to model the sloping beach, wave basin walls or the wave maker. Wave data from 21 wave gauges is available for comparison. Initially, interpolation of wave height between the wave gauges was explored. Figure 19 shows an interpolation of a wave field for a regular wave condition, $T = 1.5\,s$, compared to the compu-

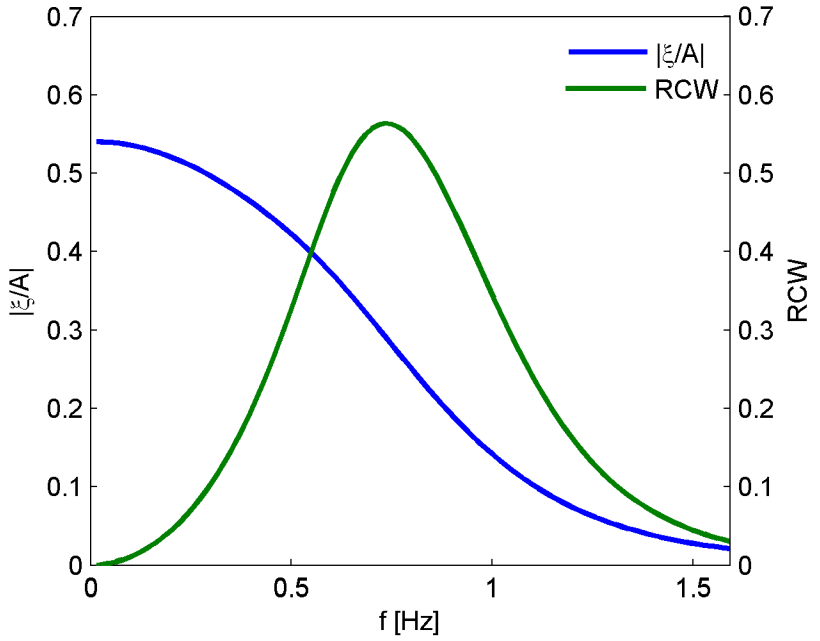

Figure 18: The plot is of the RAO ($|\xi/A|$) and relative caputure width (RCW) of cylindrical computational model of the WEC under test.

tational wave field produced by WAMIT. The WEC is indicated by a white circle, and the wave gauges are marked by 'x' and '*' symbols. The experimental data interpolation can be deceiving as it misses significant wave field features and produces wave field features that may not exist. The interpolation smooths a large region of the wave field where the model predicts standing waves. For instance, consider the two gauges at the top of the figure (greatest y value), the interpolation produces a uniform high wave height between the two gauges, but the computational wave field shows that these gauges just happen to be on the crests of standing waves, and between them the wave field varies. Although it is not certain whether the predictions of the computational wave field are in fact the behavior of the real wave field, it raises strong doubts as to the validity of the interpolated wave field.

Instead of making comparisons of the interpolated wave field, comparisons are made directly at two sets of wave gauges. One, called the offshore wave gauges, is the set of six gauges indicated by 'x' symbols in Fig. 19 that is between the WEC and the wave maker (lowest x value). The other set, called the lee wave gauges, is the line of six 'x' gauges behind the WEC in Fig. 19. The offshore and lee wave gauges are numbered 1 to 6 from left to right facing the wave maker. The numbering can be seen clearly in Fig. 16.

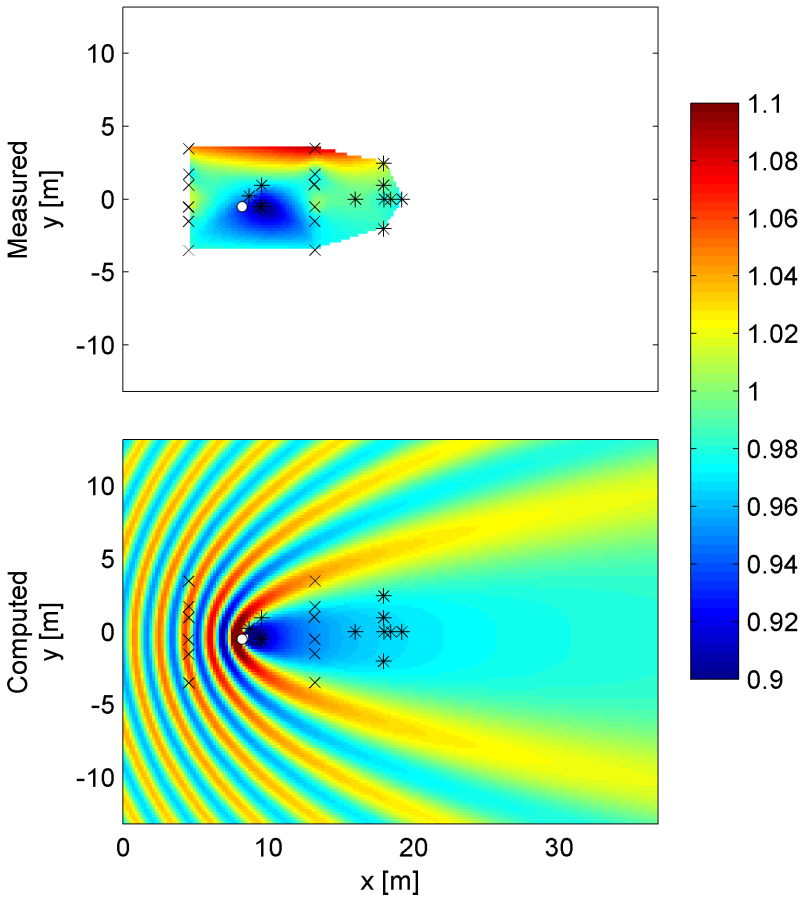

Figure 19: The top figure shows an interpolation between the values measured at the wave gauges for a regular wave with a period of $T = 1.5\ s$. The bottom figure shows the WAMIT wave field for the same wave. Note how the interpolation may distort features of the wave field.

4.2.1 Incident Wave Conditions

Determining the incident wave conditions was one of the challenges of the data analysis. The incident wave conditions are critical for determining the wave power delivered to the WECs and for calibrating the computational wave fields. Wave makers are not perfect and cannot be expected to produce precisely the wave conditions entered into their setup. One should use measurements to determine the actual waves produced.

It was believed that the offshore wave gauges would be sufficient to measure the incident wave conditions. However, the offshore gauges are within the wave field region affected by the WECs. For example, in Fig. 19 the computational result predict the offshore gauges to be on the crest of a standing wave. If one were to believe these results, then the wave height measured at the offshore gauges for this wave period would be 10% higher than the incident. However, the computational predictions should not be used adjust the incident wave heights. Determining the incident wave conditions is more challenging for spectral seas where multiple frequencies exist simultaneously. The spectra at the offshore gauges show peaks and troughs from frequency to frequency as was discussed in Sec. 4.1.2 and shown in Fig. 10. Also, as the number of WECs increases, the wave conditions measured by the offshore gauges diverge more severely from the condition supplied to the wave maker, which indicates a that the offshore wave data is dependent on the WECs.

In order to compare experimental data with computational data, one needs to know the incident wave conditions to scale the computational results. WAMIT computes results for a unit amplitude wave. The wave field can be scaled linearly by a dimensional incident wave height, and across frequencies by wave amplitudes determined by an incident wave spectrum (see Sec. 2.1). On way of determining incident wave conditions would have been to make wave gauge measurements for an empty tank, that is, in a wave tank without WECs. However, empty tank runs were only performed on a handful of conditions for another purpose.

It was decided that the incident wave conditions should be taken as the average of the offshore gauges and wave gauge 10 for the single WEC case. The single WEC case was selected because the influence of the WEC on the wave field would be less than the WEC influences of the 3 WEC and 5 WEC arrays. The offshore gauges were chosen because they are located in region from which the incident waves propagate, and wave gauge 10 was used because

it is far from the WECs and the WEC influence at gauge 10 should be small. By using the measurements from one particular case as the incident wave conditions for other trials, the assumption is that the wave maker produces repeatable results. The measured incident wave conditions for regular waves and spectral seas are summarized in Table 1. For the spectral seas cases, T_p is the period of the peak of the spectrum and H_{s-in} is the zeroth-moment significant wave height.

Regular Waves	
T (s)	H_{in} (cm)
0.9	5.70
1.1	5.70
1.5	5.54
1.7	5.64
1.9	5.47
2.1	5.43
2.3	5.52
2.5	5.59
2.7	5.37

Spectral Seas	
T_p (s)	H_{s-in} (cm)
1.25	3.83
1.43	6.96
1.67	4.43
1.54	9.87
1.67	7.79
2.22	8.25
2.22	14.8

Table 1: The tables shows values of the incident wave conditions for regular waves and spectral seas as measured by average of the offshore gauges and wave guage 10 for the single WEC trials. For the spectral seas cases, T_p is the period of the peak of the spectrum and H_{s-in} is the zeroth-moment significant wave height.

4.2.2 Regular Waves

This section compares the computational results from WAMIT to measured data from the WEC array tests for regular wave conditions. Figure 20 shows the results for the single WEC case. The left-hand column shows the offshore gauges and the right-hand shows the lee gauges. Each row shows a different wave period and the gauges are aligned as if one is facing the wave maker. The experimental data points are shown as diamond symbols. The data points are the average of two or three trials at the same condition. Repeatability between trials was excellent, and the size of the diamonds in the figure is generally greater than the one standard deviation from the average. More information on repeatability can be found in Porter [31].

For a single WEC in regular waves, there appears to be reasonable agreement between the experimental data and the computations. Two especially

exciting results are for the lee gauges at 0.9 second and 1.1 second waves. The experimental data seems to mimic the computational curve that starts with a hump on the left-hand side, decreases in the middle, has another hump to the right and then a hole. This shows the well known standing wave ridge pattern that was discussed in Secs. 3.5 and 4.1 as well as by Farley [3]. It appears that linear wave theory has some skill in modeling the wave field, and that the predicted standing waves do indeed exist for real waves. Without the linear computation model, interpreting the hills and valleys of the data transect would have been much more difficult.

For the offshore cases, the data and the model do not align as well, but as mentioned in Sec. 4.2.1, the standing wave field is very sensitive to the geometry, motions and position of the WEC, which are only crudely approximated. One would not expect to match the offshore wave field particularly well. However, it does appear that the magnitude of the variation of the data points is similar to the variation in the computational transect.

In the lee, for the periods, $T = 1.9 - 2.5\ s$, there appears to be an offset between the computational measurements and the experimental data points. At $T = 2.3$ and $2.5\ s$, the experimental points are higher than zero, which would indicate a gain in wave height rather than a wave shadow. The offset and the gain could be the result of inaccurate assessment of the incident wave conditions. For instance, if the incident wave height as determined by measurements at the offshore gauges and gauge 10 is smaller than the actual incident wave height then such an artificial gain would be produced. The low measured incident wave height would occur if the offshore gauges happened to be in the trough of an offshore standing wave. At the period, $T = 2.7$, the data does not match computational model well in the lee, which could be due to the simplicity of the computational geometry. For longer waves, the nondimensional distance between the wave gauges and WEC is smaller, and so the wave field may be more dependent on specific geometric qualities rather than the magnitude of the power absorption.

Figure 21 shows the regular wave results for the five WEC array. Generally, the results are not quite as good as those for a single WEC. Any differences between the computational and experimental models would be exaggerated five fold in the five WEC array, including the uncertainty in the positions of the WECs, and the geometric dissimilarities. For $T = 0.9\ s$, the lee experimental data may not align exactly with the computational transect, but the variation

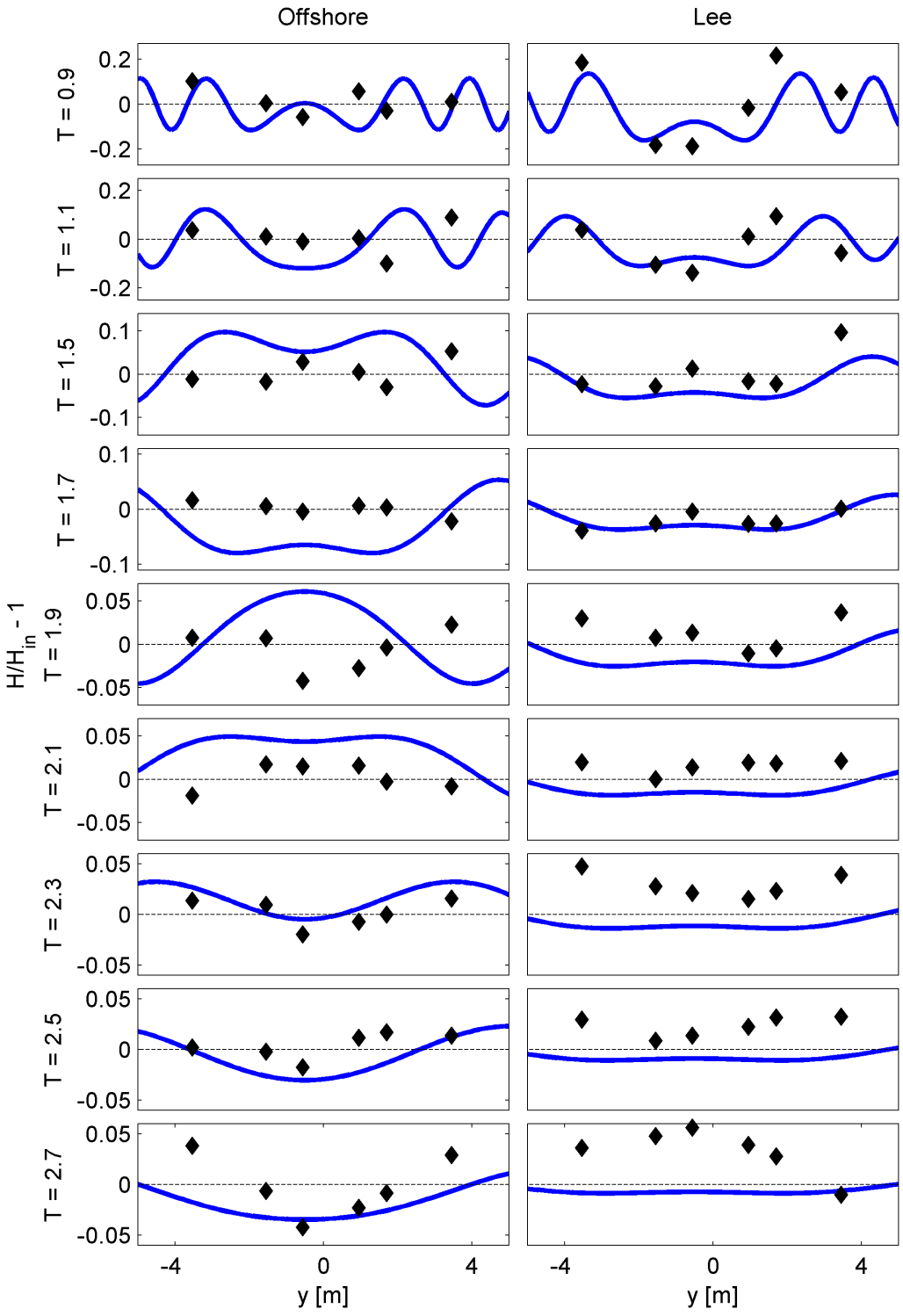

Figure 20: Figures show offshore and lee transect of the experimental results compared to the computational equivalent from WAMIT for a single WEC in regular waves.

of the data is on the same order of magnitude. The same is true for the $T = 0.9\,s$ and $T = 1.1\,s$ offshore transects. In the $T = 1.1\,s$ lee transect, one could argue that the data points follow the hill and valley pattern predicted by the model. The lee computational transect for $T = 1.5\,s$ matches the data fairly well. And the lee transects for periods, $T = 1.7 - 2.5\,s$, seem reasonable. The offshore and lee transects at $T = 2.7\,s$ are not great matches with the computational results, and differences are similar to the differences observed in the single WEC case, which again can be attributed to relatively close distance of the wave gauges to the WECs and the mismatch in geometry.

4.2.3 Spectral Seas - Significant Wave Height

This section compares the significant wave height from experimental data to that computed by WAMIT for unidirectional spectral seas. Both sets of significant wave heights are computed from the zeroth moment of the wave spectrum.

For both the one WEC and five WEC cases, the longshore structure of the experimental data matches well with the computational prediction. In the offshore, the significant wave height is was fairly uniform. The offshore variability due to standing waves that was found in the regular wave cases is smoothed in significant wave height, because it is a bulk parameter. The wave shadow is quite clear from both the data and the model, and the model appears to accurately capture its shape and relative magnitude. A couple poorer matches occur in the single WEC case. At $H_s = 8.2cm$, $T_p = 2.2s$, there is an offset in the lee between the data and model, which can be attributed to inaccuracy in the estimate of the incident wave conditions. And at $H_s = 14.8\,cm$, $T_p = 2.2\,s$, there is an offset in the offshore transect, which could be because of the influence of wave gauge 10. In both the cases, it is important to consider that the magnitude of these differences in only about $2 - 3\,\%$.

4.2.4 Spectral Seas - Wave Spectra

In this section, an irregular wave condition - $H_s = 7.58\,cm$, $T_p = 1.42\,s$ - is examined in more detail by comparing plots of the non-directional spectra at the wave gauge locations. Figure 24 shows the spectra for the single WEC case, and Fig. 25 for the five WEC case. The spectra are plotted for each gauge with the offshore spectra in the left-hand column and the lee spectra in the right. The input spectrum is the black dashed line, the computational

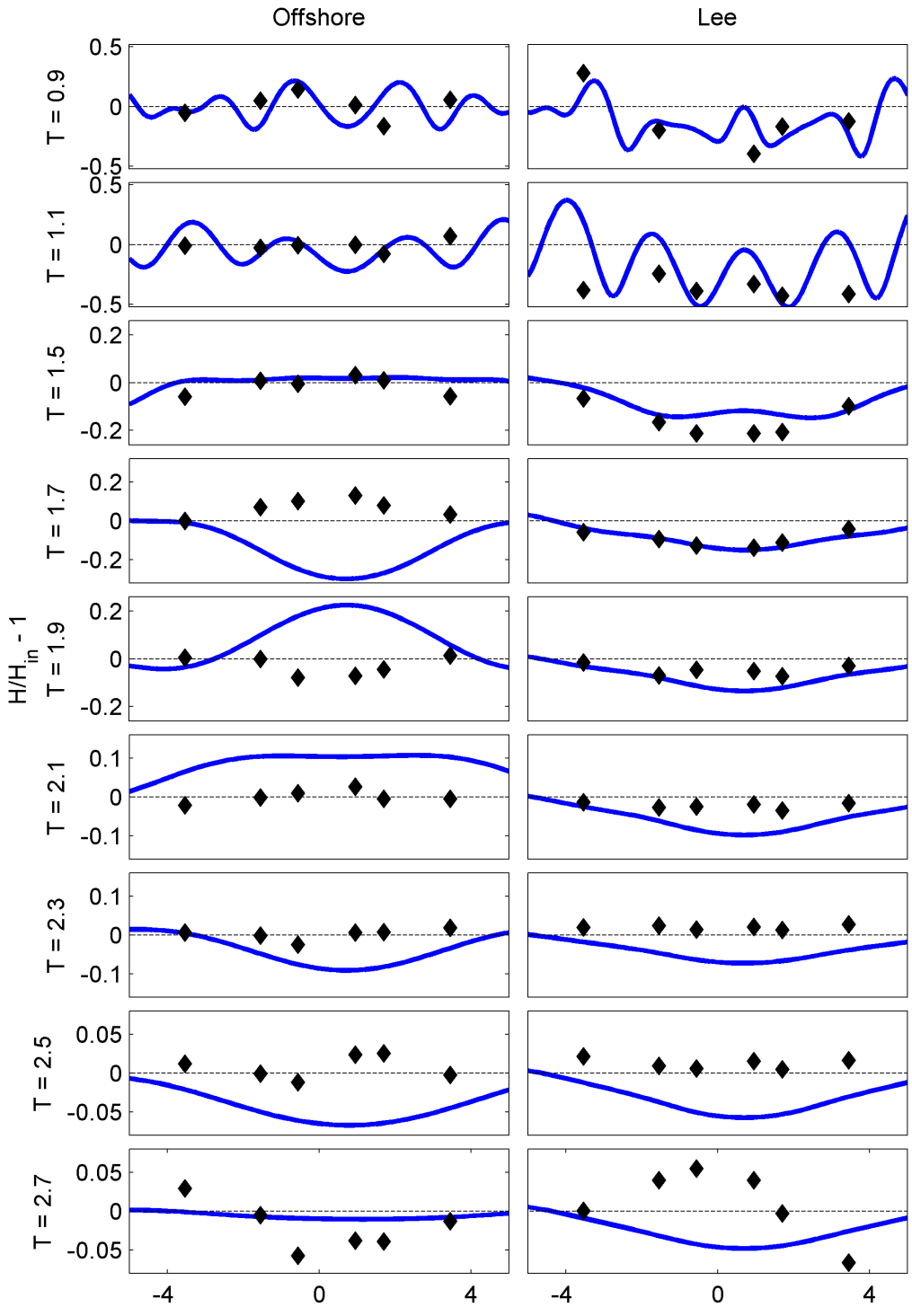

Figure 21: Figures show offshore and lee transect of the experimental results compared to the computational equivalent from WAMIT for the five WEC array in regular waves.

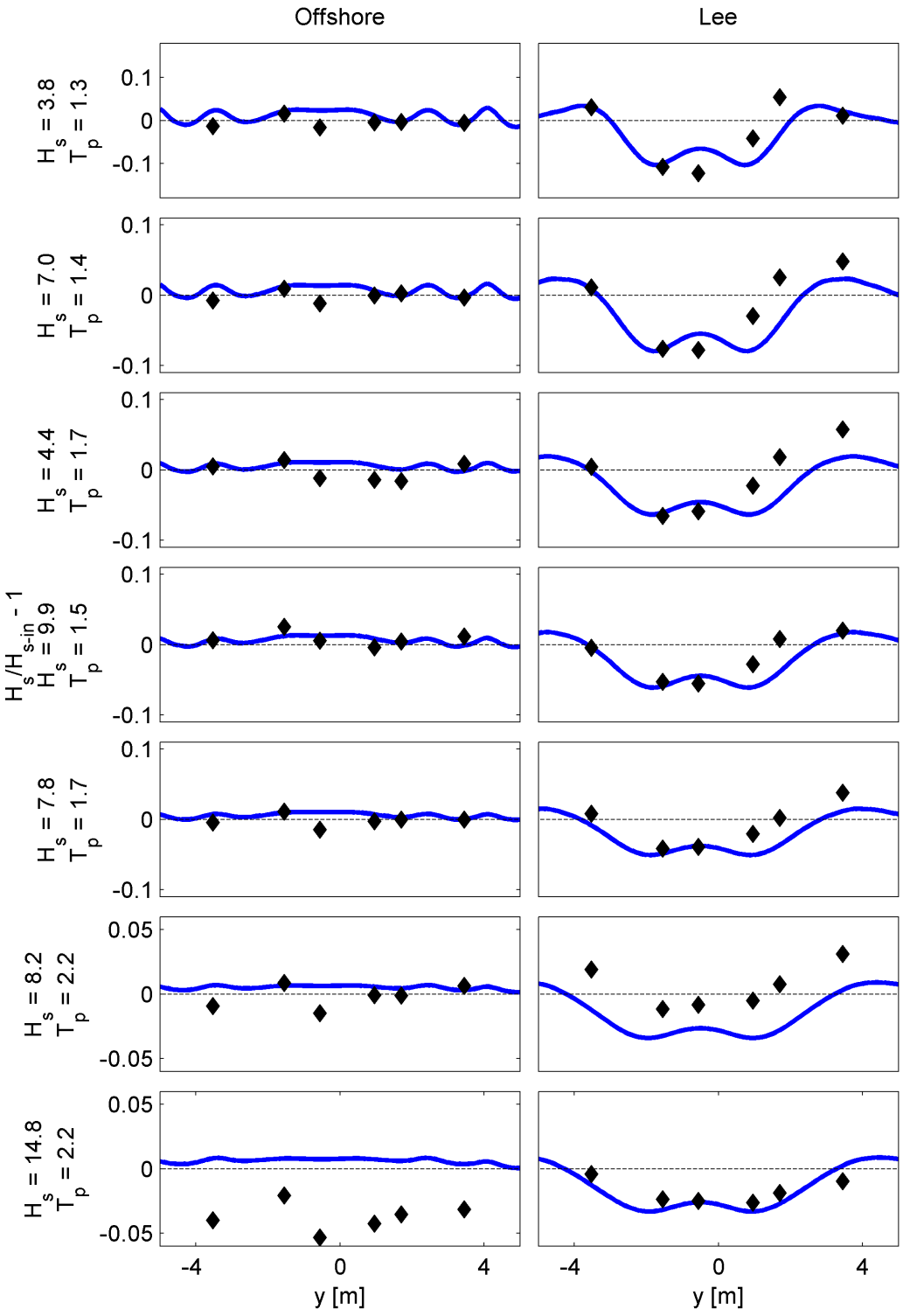

Figure 22: Figures show offshore and lee significant wave height transects of the experimental results compared to the computational equivalent from WAMIT for the single WEC in spectral seas.

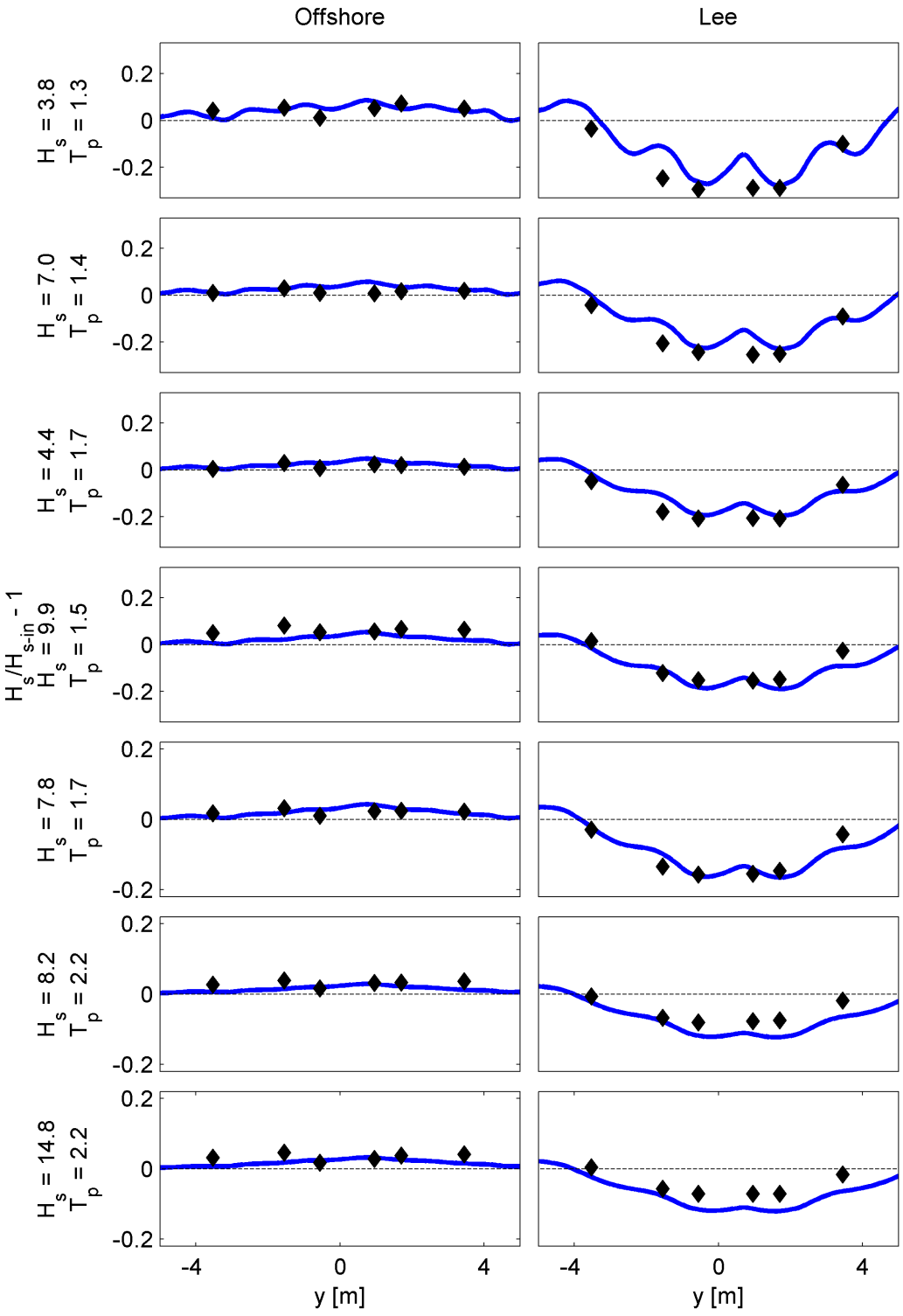

Figure 23: Figures show offshore and lee significant wave height transects of the experimental results compared to the computational equivalent from WAMIT for the five WEC array in spectral seas.

spectra are in blue and the measured spectra are in green. The green dashed lines show the 95 % confidence intervals of the measured spectra.

At first glance at the single WEC case, it is difficult to make any firm conclusions. The confidence bounds of the measured spectra are quite broad and encompass the computational spectra and the incident spectra. To understand the meaning of confidence interval, take a null hypothesis to be that the spectrum measured at a field point is the incident spectrum. If the confidence interval encloses the incident spectrum, then the null hypothesis cannot be rejected, and the field spectrum could potentially be the incident spectrum. This would mean the WECs have no effect on the wave field at those points. Now, take the null hypothesis to be that the measured spectrum is not the computational spectrum. Unless the computational result is clearly outside of the confidence intervals, the null hypothesis cannot be rejected, and the computational spectrum could be the measured spectrum. When the confidence intervals enclose the incident spectrum and the computational spectrum, then the measured spectrum could also be either the incident spectrum or the computational spectrum. To have clear results, one wants the confidence intervals to enclose the computational spectrum, but not the incident spectrum.

Despite the width of the confidence interval, the computational results do lend insight into the behavior of the experimental results. The computational results predict spikes and dips in the spectra due to frequency-dependent standing waves. The spikes and dips in the data are not extremely well resolved, which could be because the of the large number of degrees-of-freedom used in the FFT that created the spectra from the time series (for details see Porter [31]). Spectral modification does appear to exist. See in particular gauge 5 offshore and lee, and gauge 2 offshore.

Because the the effect of the WECs on the wave field increases with the number of WECs, the modification of the computational and experimental spectra for the 5 WEC array is more apparent than for the single WEC case. The computation results show dramatic spikes and dips, and the experimental results show clear modification of the spectra. An interesting result is lee gauge 6, in which both computation and experiment are in good qualitative agreement. In the lee spectra, there is a clear reduction in spectral magnitude for gauges 2 through 5, which is reflected in both the experimental data and computational results. More importantly the confidence intervals of the data do not include the incident wave spectrum, which gives us confidence that this

is a real reduction in spectral energy. This is the all important region of the wave shadow

4.3 SWAN Wave Field Analysis

In phase-resolving linear water wave theory, the phase of a wave component is computed as the argument of a complex variable. For the linear wave-body interaction problem, the phasing relationship between wave components (i.e. incident, diffracted, and radiated) is critical for determining body forces, wave fields, and absorbed power. The most common method of solving the linear wave-body problem is the boundary-element method (BEM). However, BEMs have some limitations. The BEM computation time is proportional to the square of the number of panels on wetted surfaces [12], which for arrays of WECs with complicated geometries can be quite large. Computing a large number of wave field points also requires a significant amount of time, especially for spectral wave conditions. Also, BEMs are only practical for modeling a constant depth bathymetry. In general, the BEM is not appropriate for modeling spectral seas over large domains with non-uniform bathymetry.

In contrast, phase-averaged models are designed to model spectral wave propagation over large domains with variable bathymetry, which makes them attractive for modeling the effects of WECs on the far wave field. Phase-averaged models propagate wave components with a balance of wave energy in a form known as wave action density, which is a quantity that is conserved in presence of currents. In the governing equation, only information on energy is preserved, where energy is proportional to the wave height squared; the phase of wave components is lost [32]. SWAN is a well known, and well validated phase-averaged wave model [33]. Several papers [34, 35, 36, 37] have used SWAN or another phase-averaged model to model the effects of WEC arrays on the wave field. Folley and Whittaker [38] discussed the adequacy of phase-averaged models for modeling WEC arrays. They concluded that phase-averaged models may be reasonable for modeling WEC array interactions because in reality, it is not possible to achieve precise phase relationships between devices in an array and the wave field.

The purpose of this section is to further explore the adequacy of phase-averaged models for modeling the WEC wave field by comparing the phase-resolved wave fields produced by WAMIT to those of the phase-averaged

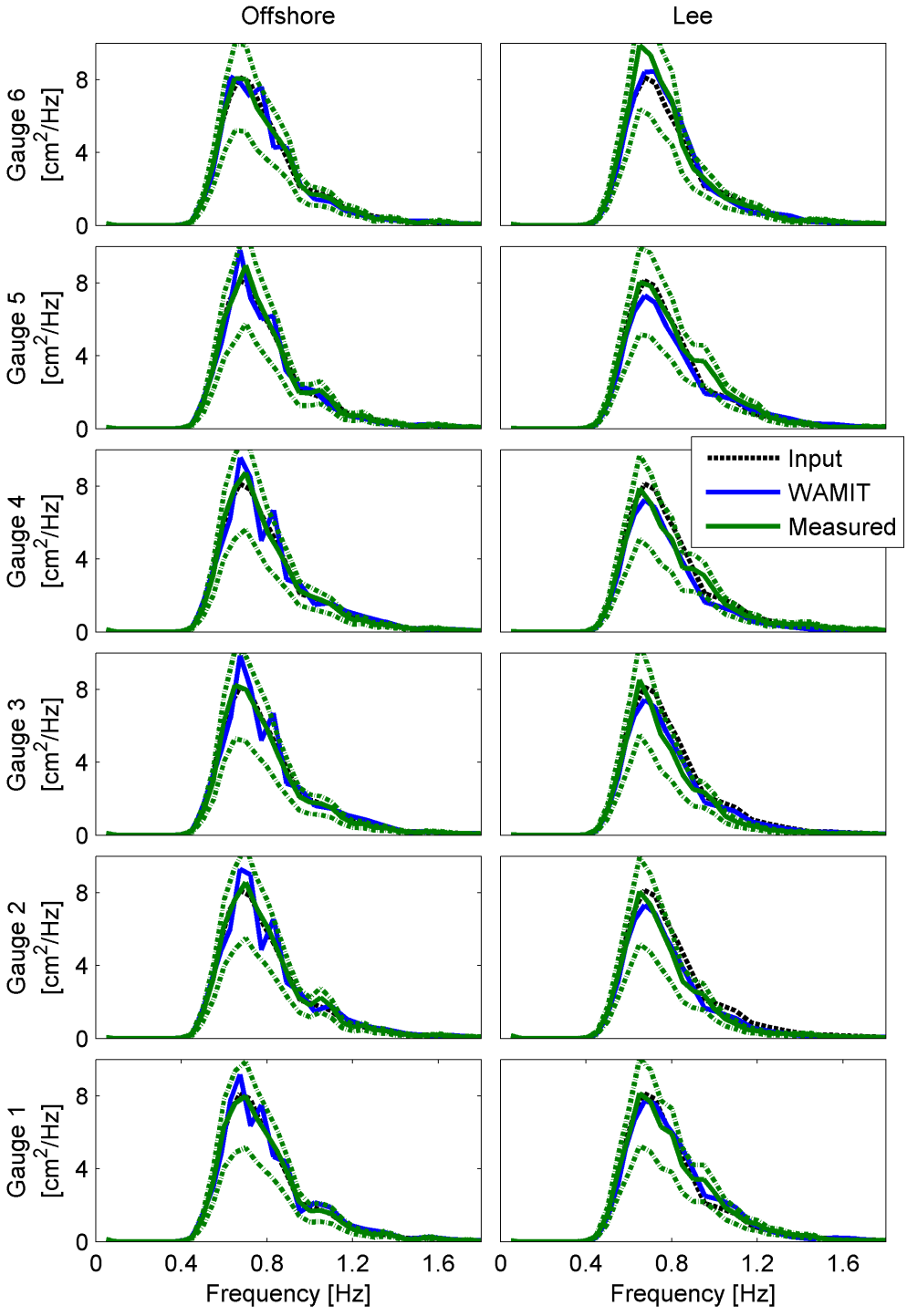

Figure 24: The figures show the measured and computational wave spectra at the wave gauges for the single WEC case.

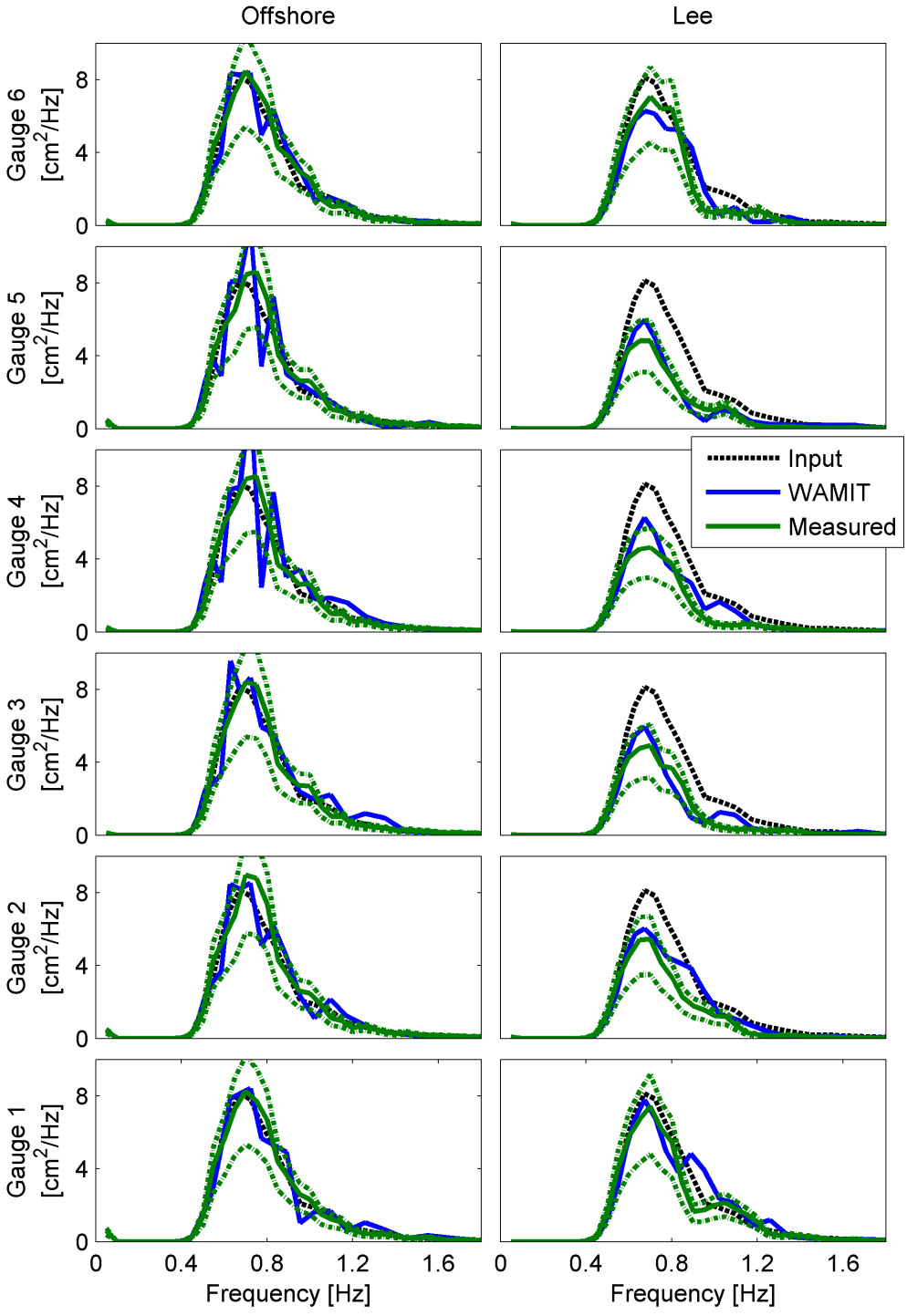

Figure 25: The figures show the measured and computational wave spectra at the wave gauges for the five WEC case.

model, SWAN. Comparisons of the wave field for regular waves and spectral seas are made in the form of plots of wave height or significant wave height respectively. In contrast to the experimental data section, incident wave conditions are known exactly, since they are inputs to the models, and wave data at all points in the wave field can be computed.

SWAN operates on a bathymetric finite element grid, propagating wave components from open boundaries throughout the domain based on the governing equations. The model domain can contain physical boundaries, which allow for partial wave reflection and transmission. Although SWAN cannot model diffraction directly, it has an option that implements a parametric approximation of diffraction that is based on the mild slope equation. The diffraction switch in SWAN changes the direction of wave energy propagation based on gradients in wave height [39].

The geometry used for the comparison is the cylindrical WEC operating in surge that is used for the WEC array experimental data study described in Sec. 4.2. To reproduce the model in SWAN, the power absorption curve is applied at an artificial boundary within the computational domain. Waves are propagated from the wave maker boundary to the location of the WEC, then over a width equal to the beam of the WEC, energy is extracted from the wave field as a function of frequency as defined by the power absorption curve, and the new waves are entered into the domain to continue propagating. The SWAN modeling was done by Porter and is described in more detail in his Masters thesis [31]. The WEC power absorption implemented in SWAN is from the power absorption curve that is determined by WAMIT. This aspect is critical to the justifying the comparison of the two models - in both models the same amount of power is absorbed at each frequency, but do the wave fields look the same?

Comparisons are made for regular waves in wave height and spectral seas with significant wave height. Plots of the wave field of the entire domain as well as transects are shown. In addition to the standard cross-shore transect, another transect in the cross-shore is introduced, the averaged cross-shore transect, which is the average in the longshore direction over the computed domain of the wave height at each cross-shore location. SWAN wave fields are shown without and with the SWAN diffraction switch set.

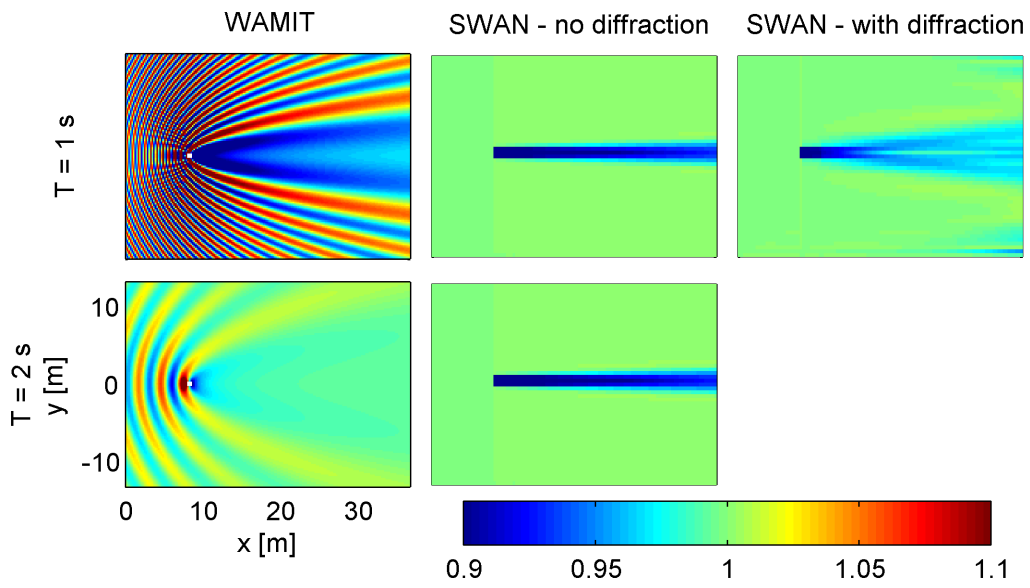

Figure 26: The figures show the wave field produced by WAMIT and SWAN for two regular wave cases. At $T = 1\ s$, there is also a SWAN wave field with the diffraction switch on.

4.3.1 Regular waves

This section compares the SWAN results to those of WAMIT for two regular waves cases - a 1 second period and a 2 second period. The 1 second regular wave case was run in SWAN with and without the diffraction switch set. Unfortunately, the 2 second case did not converge to a result with SWAN diffraction turned on.

Figure 26 shows the wave fields for the two regular wave cases. The relative capture width curve in Fig. 18 shows that at both periods approximately the same amount of energy is extracted from the wave field. Because WEC modeling in SWAN is based solely on energy extraction, the diffraction-off SWAN wave fields for both periods look the same. However, the WAMIT wave fields for the two periods are quite different from one another. The 1 second WAMIT wave field is characterized by steep standing wave ridges and large wave shadow, while the 2 second wave field has smaller standing waves and a much smaller wave shadow. In the 1 second wave field, the standing waves and large wave shadow are mostly due to scattering of the shorter wavelength wave rather than energy extraction. This is the same phenomenon that is discussed for short waves in Sec. 4.1. SWAN is not able to capture wave scattering, and because its wave shadow is based only on energy extraction,

it severely underestimates the depth and breadth of the wave shadow. When the diffraction switch is turned on for SWAN, it does a better job of capturing the shape of the linear wave shadow, but still underestimates its magnitude.

The shape of the wave shadow is an important consideration in the design of WEC arrays. Because of the interaction of the planar incident waves and circular radiated and diffracted waves, phase-resolved linear wave theory produces wave shadows that are parabolically shaped and are wider than the device width. However, SWAN only extracts energy from waves that pass directly through the WEC. The wave shadow is then a streak immediately in the lee of the device. When diffraction is turned off, SWAN does not have a physical mechanism for distributing the energy loss in the wave shadow throughout the domain. A small amount spreading of the wave shadow does occur, but this is because SWAN does not allow for truly unidirectional waves and there is a tiny amount of spreading of the regular wave. When the diffraction switch is turned on in SWAN (see Fig. 26), its wave shadow much more closely resembles the phase-resolved wave shadow. The shadow spreads nicely, and actually has a longshore structure that is similar to the phase-resolved with two dips and center ridge (see Fig. 28).

Figures 27 shows cross-shore transects of wave height for the 1 second wave. Also shown are plots of the averaged cross-shore transect, which is the average of the wave height in the longshore direction as a function of the cross-shore. The averaged cross-shore transect gives an idea of how much total energy is present in the whole computational domain. Consider the 1 second wave case. In the standard cross-shore transect, the wave height immediately in the lee of the device, is quite low for WAMIT, and increases geometrically with distance from the WEC. In SWAN the wave height begins at a more moderate value in the lee of the WEC and only increases gradually. However, when considering the averaged cross-shore transects, the wave heights behind the WEC for WAMIT and both SWAN cases begin around the same value, because all three simulations extract the same energy from the wave field. The cross-shore diffraction-on SWAN transect is actually very close to the WAMIT transect. Near the WEC, it is not as close, but as the SWAN diffraction mechanism takes effect, the energy spreading produces a shape similar to the linear wave theory results.

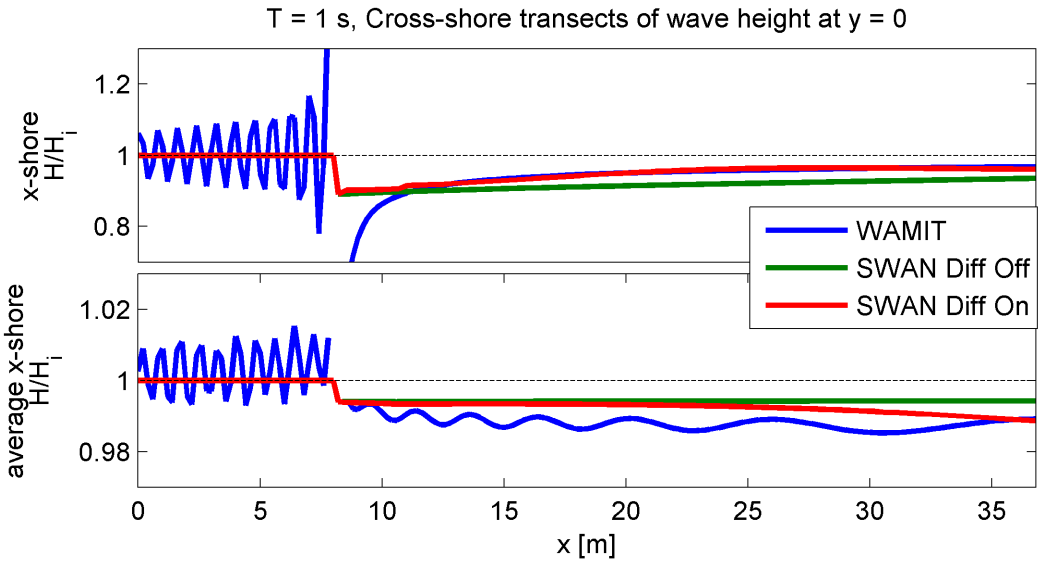

Figure 27: The figures show cross-shore transects of normalized wave height at $y = 0\,m$ (though the WEC). The top figure is a cross-section of wave height, while the bottom figure is the average of the wave height in the longshore direction at each cross-shore location.

4.3.2 Unidirectional Spectral Seas

The WAMIT and SWAN results for spectral seas are also compared. SWAN was not designed to run at a single frequency; it is generally used with a spectral distribution of wave components, and so it should perform better here. In total six spectra are considered: two peak wave periods with three levels of direction spreading. The peak wave periods are at 1 second and 2 seconds; the non-directional spectra are shown in Fig. 29 along with the RCW curve of the device. The directional spreading cases are unidirectional, and two directionally spread spectra created with cosine squared spreading functions.

First consider the unidirectional case. Wave field plots of normalized significant wave height are shown in Fig. 30. More energy is extracted by the WEC from the 2 second peak spectrum, but as before, the short wave, 1 second spectrum creates a significant scattered wave field. The results are similar to those of the regular wave case. Because of scattering of the short waves, SWAN severely underestimates the depth and width of the wave shadow even with diffraction turned on. SWAN is also not able to capture the large standing wave ridge that wraps parabolically around the device in the WAMIT 1 second case.

The SWAN results are a more similar to the WAMIT results for the 2

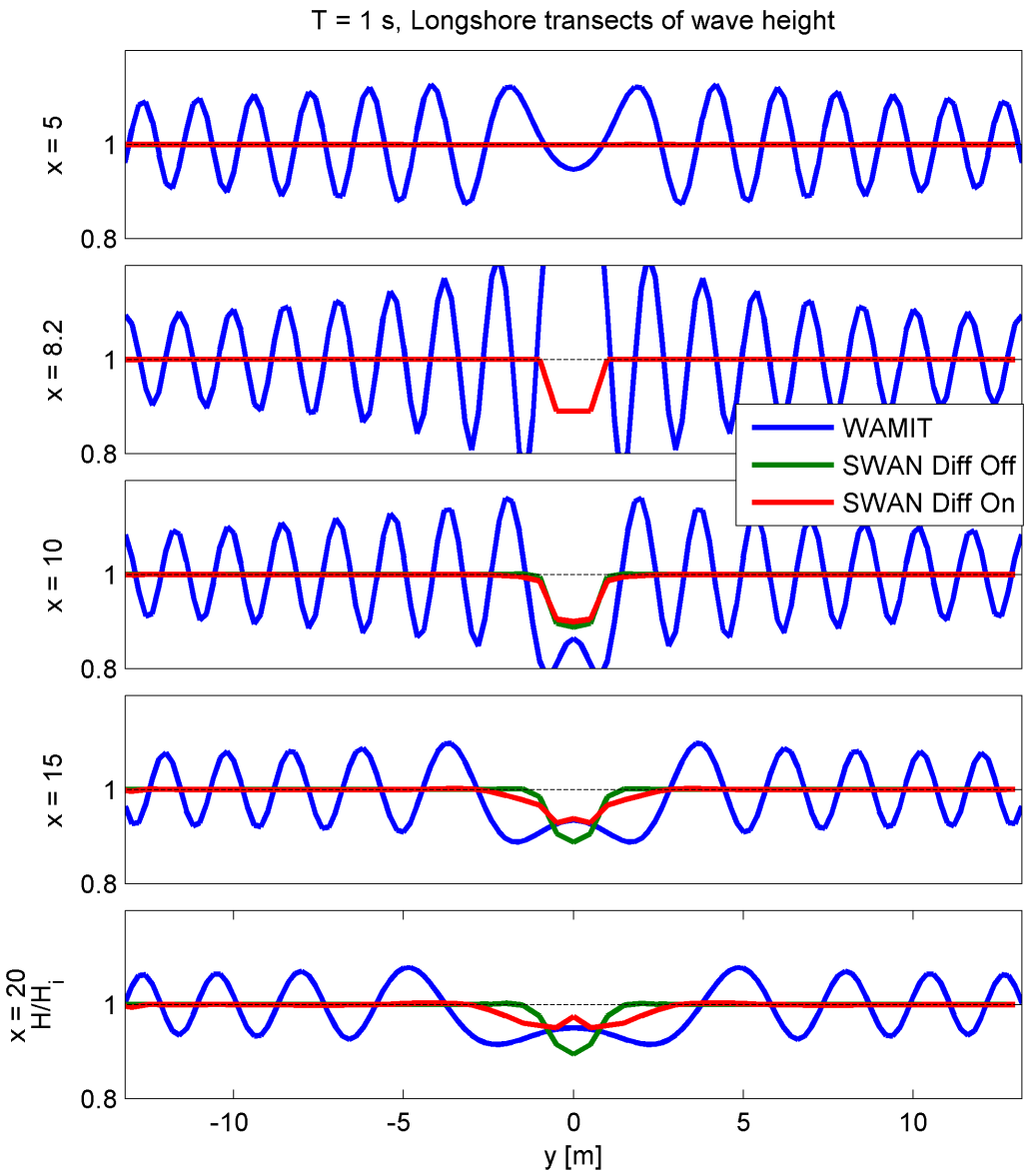

Figure 28: The figures show longshore transects at 5 locations: one offshore, one through the device, and three in the lee.

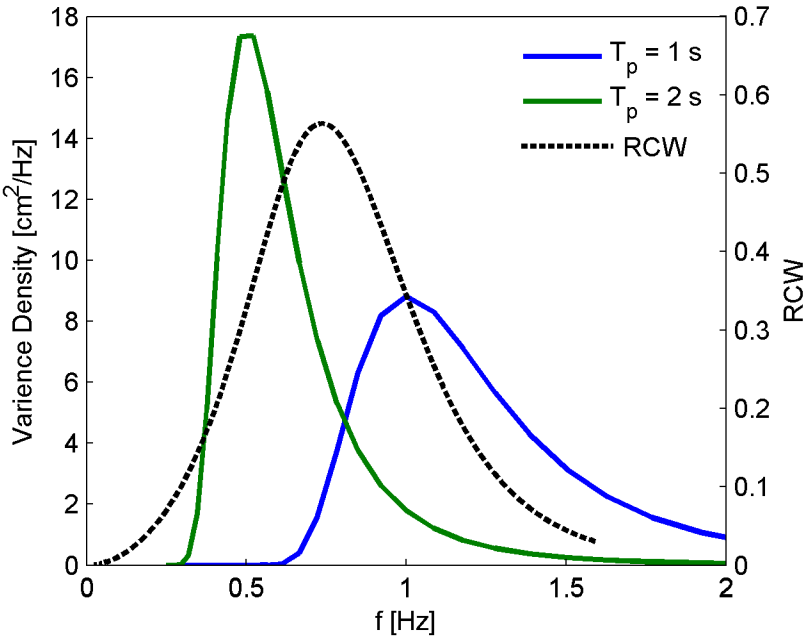

Figure 29: The figure shows the two non-directional input spectra used in the WAMIT-SWAN comparison along side the WEC RCW curve. The spectra correspond to the left y-axis and the RCW curve corresponds to the right y-axis.

second peak case, especially with diffraction turned on. For the 2 second case, the wave shadow is primarily created by energy absorption. Since SWAN only affects the wave field through energy absorption, the magnitude of the wave shadows in SWAN is similar to that of WAMIT. When diffraction is turned on, the SWAN result for the 2 second case is remarkably similar to the WAMIT result. SWAN produces the parabolic wave shadow, which has the same depth and breath as the WAMIT shadow.

4.3.3 Directional Spectral Seas

To compare the result of directional seas, cosine squared spreading is applied to the 1 and 2 second period spectra. Two levels of spreading are used and defined by the spreading parameter, s. One case is $s = 10$, which is fairly narrow, and the second is a broader spectrum with $s = 4$. The spectra are shown in Fig. 31.

As before, in the 1 second case, the wave shadow is primarily due to wave scattering, which is not captured in SWAN. The SWAN results again underes-

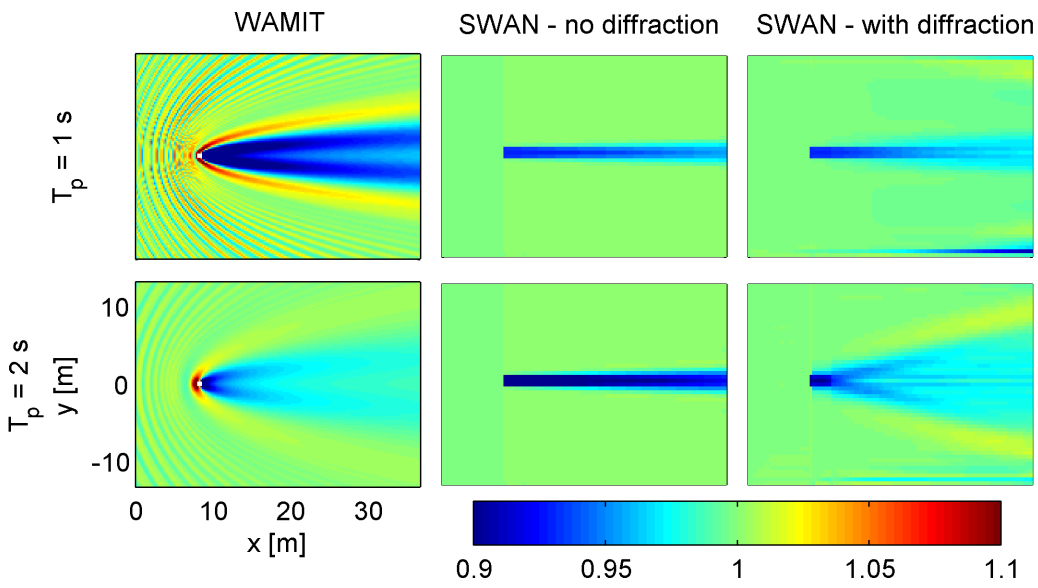

Figure 30: The figures show the wave field (H_s/H_{s-in}) produced by WAMIT and SWAN for two unidirectional spectral seas cases cases. The SWAN results include the wave field with and without the diffraction switch on. The input spectra are shown in Fig. 29.

timate the size of the wave shadow with and without diffraction at both levels of spreading. For the 2 second wave spectra, at both levels of spreading, the SWAN and WAMIT results are very similar. Both WAMIT and SWAN show egg-shaped wave shadows, due to the increase in directionality of the waves. The SWAN diffraction switch has no appreciable effect on the wave field. Directional spreading transfers the wave energy laterally and so diffraction which depends on gradients in wave height is not needed to produce a realistic wave shadow.

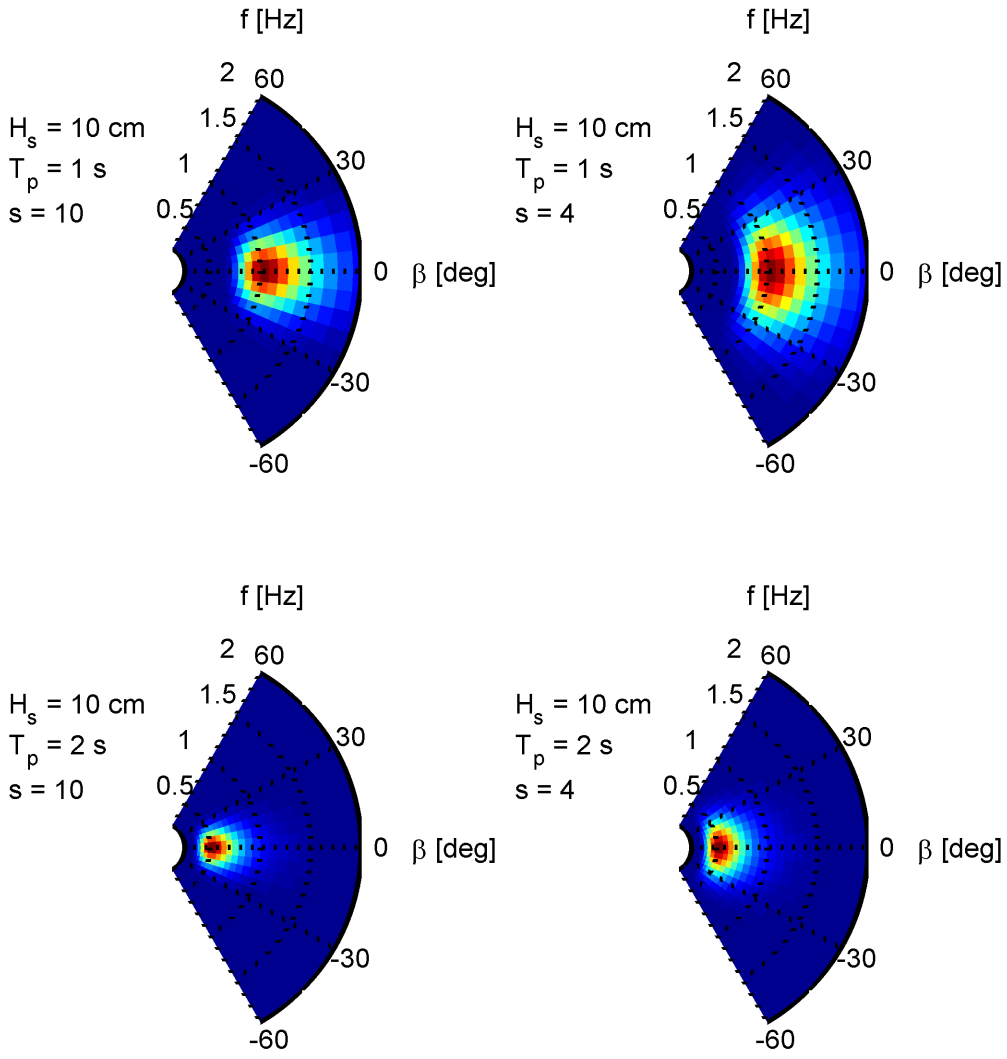

Figure 31: The figure shows the four directional input spectra (two peak periods each at two spreading widths) used in the WAMIT-SWAN comparison.

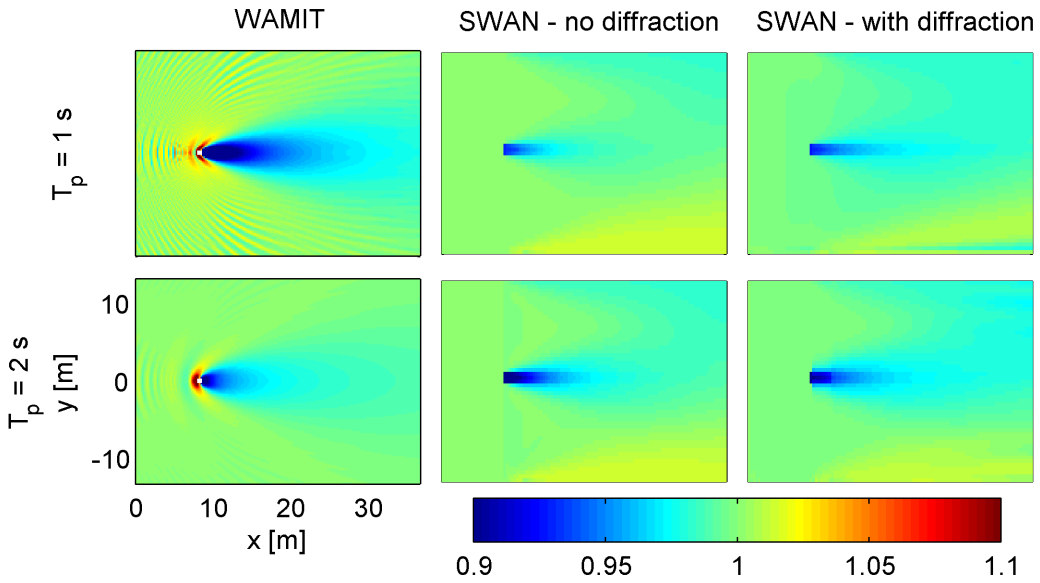

Figure 32: The figures show the wave field (H_s/H_{s-in}) produced by WAMIT and SWAN for two directional spectral seas cases, both with a spreading parameter of $s = 10$. The SWAN results include the wave field with and without the diffraction switch on. The input spectra are shown in Fig. 31

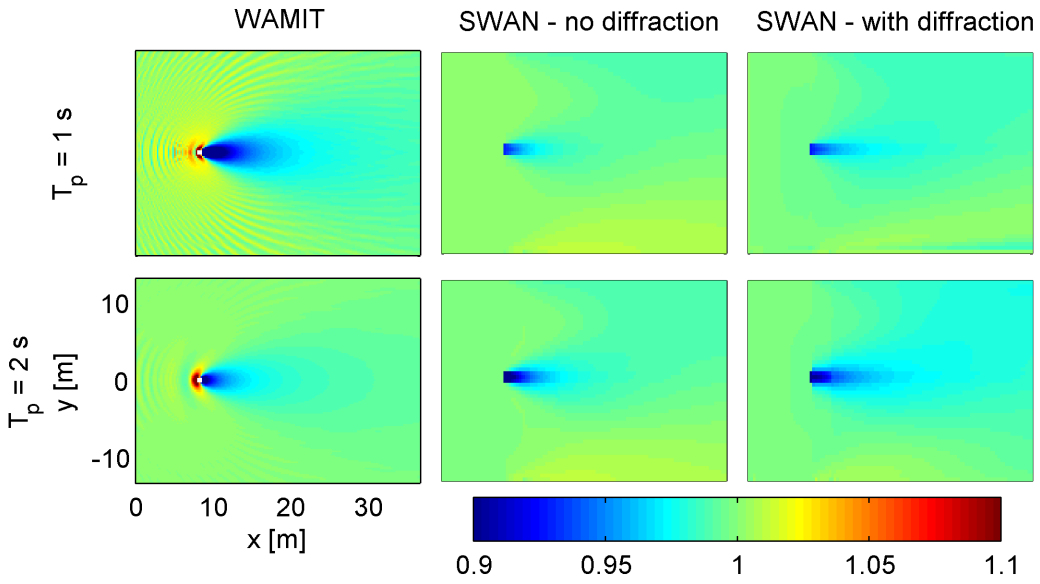

Figure 33: The figures show the wave field (H_s/H_{s-in}) produced by WAMIT and SWAN for two directional spectral seas cases, both with a spreading parameter of $s = 4$. The SWAN results include the wave field with and without the diffraction switch on. The input spectra are shown in Fig. 31

5 Discussion

5.1 WEC Wave Field Patterns

Wave energy converters affect the wave environment. The magnitude, extent and manner of the effects needs to be understood to assist in the design of WEC arrays and assess the impact of WEC arrays in the far field. The results presented here explore the near WEC wave field computationally and experimentally. A consequence of the WEC wave field effects was that in the experiment, wave gauges that were intended to measure incident wave conditions, in fact measured the WEC influenced wave field. This caused difficulty in ascertaining the incident wave conditions, which are critical for determining WEC power absorption and calibrating computational models.

The WEC wave field effects can be broken down into two related categories - standing wave ridges and the wave shadow. The standing wave ridges are partial standing waves created by the coherent interaction of the planar incident wave and the circular generated wave. In linear wave theory, they can be formulated in a straightforward manner by the superposition of a regular wave and a circular wave described by $f(\theta)(kr)^{-1/2}e^{-ikr}$. The complex generated wave function, $f(\theta)$, is responsible for the locations and magnitudes of the standing waves, while the wavelength controls the periodicity. When $f(\theta)$ is a constant the standing waves are shaped like parabolas extending to infinity in the direction of incident wave propagation. For regular waves, the standing waves are distinct.

However, in spectral seas, in terms of the bulk parameter of significant wave height, the standing wave ridges are mostly smoothed out. Although there may still be some standing waves in H_s, because the peaks and troughs occur at different locations based on the wavelength and $f(\theta)$, they appear to average towards a uniform H_s. Of course, the standing waves still exist at each frequency and can be found as spikes and holes in wave spectra taken at field points.

The standing wave phenomenon is produced by phase-resolved linear wave theory and is shown somewhat in the experimental results. From the WEC array experiment, in regular waves, there is clear variability in wave height measured across the offshore wave gauges. While in spectral seas, the significant wave height measured at the offshore wave gauges is fairly constant across the gauges. In the measured wave spectra, the magnitudes and frequency loca-

tions of the spectral spikes and dips varies across the gauges and varies between the 1 WEC and 5 WEC case. The computational results qualitatively agree. They also show variability in the offshore wave height for regular waves, which is smoothed out for spectral seas, and spikes and dips in the wave spectra. However in the offshore, the computational data does not coincide with the experimental results on a gauge by gauge and frequency by frequency basis. This can be attributed to the simplicity of the computational model and errors in the position of physical model. The standing wave field, particularly in the offshore, is very sensitive to the WEC geometry, motions, and location; none of which was captured precisely by the computational model.

In contrast, the wave field in the lee of the WEC or the wave shadow produced by linear wave theory matches the experimental data quite well. The wave shadow is the region of the wave field in the lee of the WEC where the wave height is mostly less than the incident, and which is responsible for wave energy absorption. In the context of linear wave theory, power is absorbed from the incident wave by the coherent interaction of the incident and generated wave. Farley [3] shows that only the interaction of the incident wave and the generated wave propagating in the direction of the incident wave ($\theta = \beta$) can absorb energy. The wave shadow essentially consists of the aft most parabolic standing wave trough and the region between it that converges at $\theta = \beta$.

One may think that only the generated wave at $\theta = \beta$ is needed to determine the absorbed power. However, this is a little misleading. Recall that for some fixed device cases (no power absorbed), there is a wave shadow due to wave scattering, but this is balanced by wave reflection (for example see Fig. 6 at $\lambda' = 10$, and Figs. 9, and 13). Consider Farley's equation for wave field power absorption, Eqn. 23. The power absorption occurs in the first term, which includes only the values of generated wave function in the direction of the incident wave propagation, $f(\theta) = f(0)$. The second term subtracts power based on the power radiated by the generated wave, and is the integral of $f(\theta)$ in all directions. The second term can make the power absorption zero or negative, where negative means the device radiates power. Farley gives a nice example of the Salter's Duck WEC. The Duck is asymmetric front to back and is designed *not* to radiate a wave at $\theta = \beta$. However, there is a diffracted wave at $\theta = \beta$, which is what ultimately absorbs the energy. When the device is held fixed, in addition to the wave cancellation in the lee, there

is reflected wave in the direction towards the incident wave ($\theta = -\beta$), which causes the net wave energy absorption to be zero. When the device in moving, a radiated wave propagates only at $\theta = -\beta$, which cancels the reflected wave, reduces the net radiated power (the second term in Eqn. 23), and creates power absorption.

A wave shadow must exist for a power absorbing device and may exist due to diffraction for a device that does not absorb power. Even for wave scattering, the shadow is due to generated wave in the direction of the incident wave. For a regular wave, Farley shows that the structure of the the wave field in the lee of the WEC is of a certain general form (see Fig. 7). The linear wave computational results are of this form and so are some experimental results (see Fig. 20 especially $T = 0.9\,s$ and $T = 1.1\,s$). In the terms of the longshore structure of wave height, the computational and experimental results are in reasonable agreement of the lee transects for 1 WEC and 5 WECs in regular waves.

For unidirectional spectral seas, the wave shadow is generally found at approximately the same location for all frequencies in the spectrum. The direction of power absorption, $\theta = \beta$, is the same for all frequencies, and the aft most parabolic trough does not deviate greatly from frequency to frequency. The result is that for unidirectional waves, even though the parabolic standing wave ridges are smoothed in the offshore, the wave shadow is preserved in the lee (see Fig. 9). The computational results are in very good agreement with experiment in the lee transects of H_s for both the 1 WEC and 5 WEC cases (see Figs. 22 and 23). The comparison of the lee spectra for the 1 WEC case is inconclusive, but for the 5 WEC case, the experimental and computational spectra in the lee (gauges 2-5) conclusively show a wave shadow (see Fig. 25).

Why is the linear wave computational model able to reproduce the wave shadow that is seen in the experimental results despite the model geometry and motions being only a crude representation of the physical geometry and motions? It is likely because the wave shadow depends on the power captured by the device rather than the particulars of device geometry and motions, and the cylindrical computational model was designed to have approximately the same power capture characteristics as the physical model. It is the coherent interaction of generated wave in the direction of the incident wave that enables WEC to absorb power and create a wave shadow.

Interestingly, the wave shadow produced by the phase-averaged model

occurs at wave components traveling in the direction of the incident wave and passing through the device. However, without the parametric diffraction switch set, the phase-averaged model misses a critical element of the wave shadow. Without diffraction, the phase-averaged model produces a wave shadow that extends as a streak behind the WEC, creating a physically unrealistic canyon in wave energy. When the diffraction switch is set, the diffraction mechanism smooths the steep gradient and produces a wave shadow that can be remarkably like the phase-resolved wave shadow (see Fig. 30).

The diffraction mechanism in the phase-averaged model operates based on gradients in the wave height; it is not the solution to the linear wave-body boundary value problem. The phase-averaged model is not capable of creating standing wave fields. At short wavelengths, WECs produce a large wave shadow due to scattering even though there may be little net energy absorption. The phase-averaged model wave shadow is only created by energy absorption, and so when the wave shadow is due to scattering, the phase-averaged model underestimates it (see Figs. 26 and 30).

For directionally spread spectral seas, wave shadows due to each direction overlap and the wave shadow in H_s loses its parabolic shape. The overlapping of the streak-like wave shadows of the phase-averaged model produces a shape similar to that of linear wave theory. Because wave energy is spread laterally by the directional spreading, the phase-averaged diffraction switch has little effect on the wave field. However, again, when the wave shadow is produced by scattering, the phase-averaged model underestimates it. The phase-averaged model may produce good results when the wave shadow is produced primarily by power absorption and when diffraction is set for long-crested waves or when the seas are spread directionally.

5.2 Application of the WEC Wave Field to Array Design

How could one apply the knowledge of the wave field near a single WEC to WEC array design? Constructive interactions amongst WECs in an array are achieved theoretically for a given wave when WECs operate under precise controls of amplitude and phase (optimal motions) and are located at specific positions in the wave field. The WEC positions turn out to be the locations of the peaks of standing waves, and were found almost fortuitously by varying the spacing of arrays in regular grids or by optimization routines. Child and

Venugopal [2] explicitly examined the wave field and found that by iteratively placing WECs in an array on the parabolic standing waves of other WECs, they could produce an array that performed constructively even for non-optimal motions.

However, they and others realized that a configuration that performed well for a given wave frequency and direction would perform poorly at others. An examination of spectral seas shows that except for the wave shadow, the wave field is mostly uniform in significant wave height. Since significant wave height is proportional to wave energy, the total spectral wave energy is mostly uniform throughout the wave field except in the wave shadow where there is less energy. Also, in "The adequacy of phase-averaged wave models for modelling wave farms," Folley and Whittaker [38] pointed out that the lack of precise knowledge about the position of the WECs and the phasing of wave and device motions would make net consistent constructive performance nearly impossible. This has implications for the design of arrays of real devices, which move about on their moorings and cannot be controlled precisely, in real wave conditions, which are spread in frequency and direction. Perhaps the goal of array design should simply be to avoid the wave shadow where there is a net reduction in wave energy.

A wave shadow could be devised for a given WEC in its expected sea state, or perhaps a generic shadow could be created for an amount of power absorption and a parametric sea spectrum. Wave shadows have been shown to exist for regular waves, unidirectional spectral seas, and spectral seas spread in direction. They have a fairly standard shapes - parabolic and in some cases with a ridge in the middle. The shape and magnitude of the wave shadow are functions of the power absorption rather that the precise geometric and motion characteristics of the WEC. It can be well produced by phase-resolving linear wave theory and in some cases by phase-averaged models. The devised wave shadow could be used to determine the placement of WECs in the array, even in as simple a manner as providing a minimum distance for the spacing between rows. By placing WECs in an array outside of the wave shadows of other WECs, the destructive losses should be minimized for real wave conditions.

5.3 Future Work

In most cases, the wave fields considered in detail in this work are for a single WEC. Individual WEC wave fields cannot necessarily be superimposed upon one another, although they can under the point absorber assumption. In the presence of multiple WECs, there is multiple scattering; that is, the diffracted and radiated waves from one WEC are diffracted off another and those waves can be diffracted off other WECs and so on. It seems prudent to see how the wave field from one WEC extends to the wave field of an array of WECs. Under what circumstances (for instance, under the point absorber assumption) can the wave field from a single WEC be used to determine the wave field of a WEC array? Will the wave shadow method of WEC array design described in the previous section work? Or is it too simple? Will it miss potentially advantageous WEC array configurations? Quite simply, can the wave field from a single WEC be used to design WEC arrays?

Another interesting aspect of the wave field is the importance of the complex generated wave function, $f(\theta)$. Wave fields produced with simple formulation of $f(\theta)$ (see Sec. 3.5) are remarkably similar to wave fields produced with a full formulation of the linear wave boundary value problem. It would be straight-forward to determine an $f(\theta)$ from computational results. Could $f(\theta)$ be determined from experimental results? If one had an $f(\theta)$ function that represented a WEC, how would the wave field produced with the simple formulation (Eqn. 18) compare to the wave field produced by the full linear wave boundary value problem? Could the $f(\theta)$ function be used to explicitly to design arrays? How does the presence of other devices in an array affect the $f(\theta)$ of a single device?

There is also a good deal of work left in the experimental data comparison. Only a simple computation model of the WEC under test could be created due to time limitations and proprietary concerns. This turns out to be somewhat of a blessing in disguise, because it forces the researchers to consider why such a simple model could produce good results in the lee of the WEC, and it shows that the wave shadow it rather generic and not specific to a geometry. The question remains, could better results be obtained for a more accurate computational model, especially in the offshore? It would be nice to construct a computational geometry that was a better representation of the WEC and that operated in all modes of motion. This is not a trivial task.

The implementation of WECs in the phase-averaged model could also pos-

sibly be improved. In the current implementation, the WECs only affect the wave field by power absorption. However, for short waves, the impact of the wave scattering is significant. Perhaps the WEC in the phase-averaged model could include reflection that would redirect wave components offshore. This may be consistent in terms of conservation of energy as long as the same amount of energy that is redirected offshore is also removed from waves propagating in the lee of the WEC, which would create the wave shadow due to scattering that is missing in the current model.

6 Conclusion

The near WEC wave field is characterized by two significant patterns - 1) standing waves that are mostly parabolic and 2) a wave shadow. The standing waves can be formed through simple mathematical representations of the WEC wave field (i.e. the generated wave as $f(\theta)(kr)^{-1/2}e^{ikr}$) as well as by solving the linear wave boundary value problem. In previous theoretical work, WEC array design has taken advantaged of the standing wave patterns to create arrays with constructive power production. In spectral seas, in terms of significant wave height, the standing waves are not distinct. However, they can still be found in wave field spectra as spike and dips. Because spectral seas smooth standing waves, their advantage in producing constructive arrays in real conditions is diminished.

However, in spectral seas as well as in regular waves, a significant wave shadow exists. The wave shadow is produced computationally with linear wave theory, and the linear wave results are in reasonable agreement with experimental measurements. In two single-WEC regular wave cases ($T = 0.9\,s$ and $T = 1.1\,s$), the lee transect shows a longshore structure including standing wave ridges that was predicted by Farley and modeled by linear wave theory. For spectral seas in terms of significant wave height, the longshore structure of wave shadow shown in experimental data is in very good agreement with computational results. The wave shadow is the necessary result of power absorption by a WEC. Farley shows that in linear wave theory, power absorption is created the destructive interference of the planar incident wave and the portion of the circular generated wave propagating in the direction of the incident wave ($\theta = \beta$). The destructive interference at $\theta = \beta$ and the aft-most standing wave trough combine to form a wave shadow that has a parabolic or triangular shape. This wave shadow shape is mostly maintained for unidirectional spectral seas and becomes more oval-like for seas spread in direction. When designing a WEC array, rather than attempting constructive interference by using standing waves patterns, perhaps the best the array designer can do is avoid the unquestionably destructive interference of the wave shadow.

Further work needs to be done to explore how the single WEC wave field extends to the wave field of multiple WECs and to devise more concrete methods of wave field based WEC array design. The WEC wave field approach to array design seems promising. The power production and economic perfor-

mance of wave energy converters will depend not just on efficient individual devises but on effective wave farm design, for which a thorough understanding of the WEC array hydrodynamics interactions is required.

Bibliography

[1] Haller, M., Porter, A., Lenee-Bluhm, P., Rhinefrank, K., Hammagren, E., Ozkan-Haller, H. T., and Newborn, D., 2011. "Laboratory observations of waves in the vicinity of WEC-arrays". In Proceedings of the 9th European Wave and Tidal Energy Conference, Southamption, UK.

[2] Child, B., and Venugopal, V., 2010. "Optimal configurations of wave energy device arrays". *Ocean Engineering,* ***37***, Nov., pp. 1402–1417.

[3] Farley, F. J. M., 2011. "Far-field theory of wave power capture by oscillating systems". *Philosophical Transactions of the Royal Society A: Mathematical, Physical and Engineering Sciences,* ***370***(1959), Dec., pp. 278–287.

[4] Folley, M., Babarit, A., Child, B., Forehand, D., O'Boyle, L., Silverthorne, K., Spinneken, J., Stratigaki, V., and Troch, P., 2012. "A review of numerical modelling of wave energy converter arrays". In Proc. Of the ASME 2012 31th International Conference on Ocean, Offshore and Arctic Engineering.

[5] Budal, K., 1977. "Theory for absorption of wave power by a system of interacting bodies". *Journal of Ship Research,* ***21***(4), Dec., pp. 248–253.

[6] Evans, D. V., 1980. "Some analytical results for two and three dimensional wave-energy absorbers". In *Power from Sea Waves*. Academic Press, London, UK, pp. 213–249.

[7] Thomas, G. P., and Evans, D. V., 1981. "Arrays of three-dimensional wave-energy absorbers". *Journal of Fluid Mechanics,* ***108***, pp. 67–88.

[8] McIver, P., 1994. "Some hydrodynamic aspects of arrays of wave-energy devices". *Applied Ocean Research,* ***16***, pp. 61–69.

[9] Simon, M. J., 1982. "Multiple scattering in arrays of axisymmetric wave-energy devices. part 1. a matrix method using a plane-wave approximation". *Journal of Fluid Mechanics,* ***120***, pp. 1–25.

[10] Kagemoto, H., and Yue, D. P., 1986. "Interactions among multiple three-dimensional bodies in water waves: an exact algebraic method". *Journal of Fluid Mechanics,* ***166***, pp. 189–209.

[11] WAMIT. www.wamit.com/manual.htm.

[12] Mei, C. C., 1978. "Numerical methods in water-wave diffraction and radiation". *Annual Review of Fluid Mechanics,* ***10***, pp. 393–416.

[13] Kalen, O., 2010. "A study of the change of the wave field due to the presence of wave energy converters". Masters thesis, Goteborg University.

[14] Cruz, J., Sykes, R., Siddorn, P., and Taylor, R., 2010. "Estimating the loads and energy yield of arrays of wave energy converters under realistic seas". *IET Renewable Power Generation,* ***4***, p. 488.

[15] De Backer, G., Vantorre, M., Beels, C., De Rouck, J., and Frigaard, P., 2010. "Power absorption by closely spaced point absorbers in constrained conditions". *IET Renewable Power Generation,* ***4***, p. 579.

[16] Folley, M., and Whittaker, T., 2009. "The effect of sub-optimal control and the spectral wave climate on the performance of wave energy converter arrays". *Applied Ocean Research,* ***31***, Oct., pp. 260–266.

[17] Vicente, P. C., de O. Falcão, A. F., Gato, L. M., and Justino, P. A., 2009. "Dynamics of arrays of floating point-absorber wave energy converters with inter-body and bottom slack-mooring connections". *Applied Ocean Research,* ***31***, Oct., pp. 267–281.

[18] Babarit, A., Borgarino, B., Ferrant, P., and Clement, A., 2010. "Assessment of the influence of the distance between two wave energy converters on energy production". *IET Renewable Power Generation,* ***4***, p. 592.

[19] Babarit, A., 2010. "Impact of long separating distances on the energy production of two interacting wave energy converters". *Ocean Engineering,* ***37***, June, pp. 718–729.

[20] Borgarino, B., Babarit, A., and Ferrant, P., 2012. "Impact of wave interactions effects on energy absorption in large arrays of wave energy converters". *Ocean Engineering,* ***41***, Feb., pp. 79–88.

[21] Falnes, J., and Budal, K., 1982. "Wave power absorption by parallel rows of interacting oscillating bodies". *Applied Ocean Research,* ***4***(4), pp. 194–207.

[22] Mavrakos, S. A., and Kalofonos, A., 1997. "Power absorption by arrays of interacting vertical axisymmetric wave-energy devices". *Journal of Offshore Mechanics and Arctic Engineering,* ***119***(4), Nov., pp. 244–251.

[23] Ricci, P., Saulnier, J. B., and de O. Falcão, A. F., 2007. "Point-absorber arrays: configuration study off the potuguese west coast". In Proceedings of the 7th European Wave and Tidal Energy Conference, Porto, Portugal.

[24] Fitzgerald, C., and Thomas, G., 2007. "A preliminary study on the optimal formation of an array of wave power devices". In Proceedings of the 7th European Wave and Tidal Energy Conference, Porto, Portugal.

[25] Newman, J. N., and Lee, C.-H., 2002. "Boundary-element methods in offshore structure analysis". *Journal of Offshore Mechanics and Arctic Engineering,* ***124***, pp. 81–89.

[26] Evans, D. V., 1976. "A theory for wave-power absoption by oscillating bodies". *Journal of Fluid Mechanics,* ***77***, pp. 1–25.

[27] Falnes, J., 2002. *Ocean Waves and Oscillating Systems: Linear Interactions Including Wave-Energy Extraction*, 1 ed. Cambridge University Press, Apr.

[28] Wypych, M., Le-Ngoc, L., Alexander, K., and Gardner, A., 2012. "On the application of circular–cylindrical waves to ocean wave power absorption". *Ocean Engineering,* ***40***, Feb., pp. 69–75.

[29] Newman, J., 1977. *Marine Hydrodynamics*. MIT Press, Cambridge Mass.

[30] Dean, R. G., and Dalrymple, R. A., 1991. *Water Wave Mechanics for Engineers & Scientists (Advanced Series on Ocean Engineering-Vol2)*. World Scientific Pub Co Inc.

[31] Porter, A., 2012. "Laboratory observations and numerical modeling of the effects of an array of wave energy converters". Masters thesis, Oregon State University, Aug.

[32] Holthuijsen, L., 2007. *Waves in Oceanic and Coastal Waters*. Cambridge University Press, Cambridge.

[33] The SWAN Team, 2011. SWAN. http://www.swan.tudelft.nl.

[34] Millar, D., Smith, H., and Reeve, D., 2007. "Modelling analysis of the sensitivity of shoreline change to a wave farm". *Ocean Engineering,* ***34***(5-6), Apr., pp. 884–901.

[35] Smith, H., Millar, D., and Reeve, D., 2007. "Generalisation of wave farm impact assessment on inshore wave climate". In Proceedings of the 7th European Wave and Tidal Energy Conference.

[36] Alexandre, A., Stallard, T., and Stansby, P., 2009. "Transformation of wave spectra across a line of wave devices". In Proceedings of the 8th European Wave and Tidal Energy Conference.

[37] Silverthorne, K. E., and Folley, M., 2011. "A new numerical representation of wave energy converters in a spectral wave model". In Proceedings of the 9th European Wave and Tidal Energy Conference.

[38] Folley, M., and Whittaker, T., 2011. "The adequacy of phase-averaged wave models for modelling wave farms". In Proc. Of the ASME 2011 30th International Conference on Ocean, Offshore and Arctic Engineering.

[39] Holthuijsen, L., Herman, A., and Booij, N., 2003. "Phase-decoupled refraction–diffraction for spectral wave models". *Coastal Engineering,* ***49***(4), Oct., pp. 291–305.